

HEATING AND COOLING OF NEUTRON STAR CRUSTS

By

Michelle Suzanne Ouellette

A DISSERTATION

Submitted to
Michigan State University
in partial fulfillment of the requirements
for the degree of

DOCTOR OF PHILOSOPHY

Department of Physics and Astronomy

2005

ABSTRACT

HEATING AND COOLING OF NEUTRON STAR CRUSTS

By

Michelle Suzanne Ouellette

With the launch of *Chandra* and *XMM*, many new and exciting observations of neutron stars are being made. Some of these observations have detected transient neutron stars cooling into quiescence. Transient neutron stars are a class of objects which are observed to go through accretion outburst periods followed by long quiescent intervals. These sources offer unique opportunities to probe the interior physics of neutron stars. In order to interpret these observations, accurate models of neutron star crusts are needed. In addition, experiments must be done to accurately determine the nuclear physics input for the calculations.

A theoretical crust model was developed in this work to follow the evolution of the quiescent luminosity of a transiently accreting neutron star, and its results were compared with observations of two transient neutron stars: KS 1731-260 and MXB 1659-298. The comparison shows that the calculations for one set of parameters are consistent with observations of KS 1731-260, but under-predict the quiescent luminosity for MXB 1659-298. Additional physics is necessary to fully understand these systems. Constraints such as the conductivity of the crust and the material at the center of the star can still be made on the interior physics of these neutron stars. More observations are necessary to obtain data on more systems and to better map out the actual cooling curves. To enable the interpretation of future observations, a parameter study was performed to determine a set of cooling curve predictions for various outburst lengths, recurrence times, and mass accretion rates.

The most important input to the cooling calculations is the heat deposited in the

crust during outburst events, which is a function of the outburst length and mass accretion rate, and determines the temperature of the crust before quiescence. This, in turn, determines how the crust cools after the outburst. The primary sources of heating in the crust come from electron captures throughout the crust and pycnonuclear reactions in the inner crust. Preliminary work has been done to calculate the depth and thickness of these reaction layers using a network calculation implementing a realistic thermal model in conjunction with all the relevant nuclear physics. The depth and thickness of these layers depend on the temperature of the capture layer, the nuclear electron capture reaction rate, and the reaction Q -value. Additional studies are necessary to properly calculate the electron phase-space factor in determination of the electron capture reaction rates.

Since the nuclei involved in the electron captures are very neutron-rich, many of the nuclear properties necessary to calculate the electron captures are available only from theoretical models. Experiments must be made to provide accurate data as input for these calculations; of primary interest are the masses of these exotic nuclei. An experiment has been proposed at the National Superconducting Cyclotron Laboratory at Michigan State University to make time-of-flight measurements of nuclei in the ^{70}Fe region. A pair of stacked parallel-plate avalanche counters for use in such an experiment were designed, built, and tested. It was found that the resolution of these detectors in the current design is too low for use in mass measurements requiring a high timing precision.

ACKNOWLEDGMENTS

Without the support of those around me, finishing this degree would not have been possible. First and foremost, I would like to thank my advisor Hendrik Schatz. I could not have asked for a better guide through my graduate career, especially when we decided that theory was a better fit for me than experimental physics. Thanks, also, for being easy-going and conducting occasional group meetings at Harper's which helped to ease the stress of work and make our research group more friendly.

Thanks to Ed Brown for suggesting the cooling neutron star project and for his guidance in its progress.

Thanks to John Yurkon for bestowing on me all his expertise in gas detectors and to Alfredo Estrade Vaz for his help in building and rebuilding the same detectors. Thanks also to Peter Santi for explaining nuclear electronics and for guiding the development of the detectors.

Thanks to my guidance committee: Hendrik Schatz, Ed Brown, Horace Smith, Brad Sherrill, and Bob Stein. Thanks to Hendrik and Ed for reading my thesis multiple times and beating it into a coherent form.

Thanks to the Schatz groupies for discussions about various projects and for amusement in the midst of physics research. Some more cheap champagne, Paul?

Thanks to the National Science Foundation, the Joint Institute for Nuclear Astrophysics, and the Graduate School Dissertation Completion Fellowship for their financial support.

Thanks to the staff of the NSCL for providing me with the necessary resources to complete these projects. The computer group was especially helpful in humoring my incessant requests for more disk space.

Thanks to the grad students, both at the NSCL and in the Astronomy group. The numerous outings to movies, bad sci-fi movie nights, and Christmas craft parties made

grad school more enjoyable. Thanks to my officemates Pat, Jenny, Ryan, and Russ for putting up with my occasional outbursts. Special thanks to Katie for dragging me to aerobics; to Debbie for being the other “big one” in ballet; to Heather and Karen for listening when I needed an ear; and to Regner and Dali for all of our wonderful dinner parties. Thanks to Ion for many meals, long nights of homework, and being my friend for so long. Thanks also to Eric for making me realize that there is life outside of physics.

Finally, thanks to my family for their support through my many years of studies and for some reason thinking that a PhD in astrophysics would be a good idea. Thanks to Andi for being the best sister ever and listening when I needed to talk.

Et un autre “enfin”. Merci à Fabrice pour sa patience pendant ces trois longues années. N’es-tu pas heureux de ne plus avoir à faire ces huit heures de route? J’attends avec impatience les années à venir avec toi.

Contents

1	Introduction	1
2	Background	6
2.1	Neutron star structure	7
2.2	Binary systems and accretion	9
2.3	Neutron star transients	11
2.4	Thermonuclear bursts	13
2.4.1	X-ray bursts	14
2.4.2	Superbursts	16
2.5	Observations	17
3	The Cooling of Neutron Star Transients	19
3.1	Description of the model	19
3.1.1	Thermal balance in the crust	19
3.1.2	Physical input	22
3.1.3	Numerical method	35
3.2	The transient neutron star KS 1731-260	39
3.2.1	Observations of the source	39
3.2.2	Modeling the source	41
3.2.3	Summary	52
3.3	MXB 1659-298	53
3.3.1	Observations of the source	53
3.3.2	Calculations	54
3.3.3	Summary	58
3.4	Evolution of quiescent luminosity: a parameter study	58
3.4.1	Results	59
3.4.2	Summary	68
3.5	Future work	68
4	Electron Captures in Neutron Star Crusts	70
4.1	Theory	70
4.1.1	Thermal structure	70
4.1.2	Electron captures	75
4.1.3	Numerical method	82
4.2	Results	86

4.2.1	The $A = 56$ chain	86
4.2.2	Capture dependences	89
4.3	Summary and future prospects	93
5	Time-of-flight Detectors	96
5.1	Time-of-flight measurements	96
5.2	Measuring the mass of ^{70}Fe	97
5.3	Timing detectors	100
5.3.1	Electronics	103
5.3.2	Detector tests	104
5.3.3	Sources of error	106
5.4	Outlook	109
6	Conclusion	110
A	Outer boundary condition derivation	113
B	Heat capacity and neutrino luminosity of the core	115
	<i>Bibliography</i>	118

List of Figures

2.1	Internal structure of a neutron star.	8
2.2	Illustration of the Roche lobes in a binary system.	10
2.3	The lightcurve of Aquila X-1.	12
2.4	The lightcurve of KS 1731-260.	13
2.5	The reaction flow of the rp-process.	15
3.1	Time for heat to diffuse to the top of the crust and to the core.	22
3.2	The equation of state.	24
3.3	The critical temperature, T_c , as a function of density.	26
3.4	Crustal composition and nuclear energy sources in the crust.	33
3.5	Calculation of KS 1731-260 for $\tau_{ob} = 12$ yr and $\tau_{rec} = 1500$ yr.	42
3.6	Calculation of KS 1731-260 for $\tau_{ob} = 12$ yr and $\tau_{rec} = 1500$ yr with a declining \dot{M}_{ob}	44
3.7	Calculation of KS 1731-260 for $\tau_{ob} = 6$ yr and various recurrence times.	48
3.8	Calculation of KS 1731-260 for $\tau_{ob} = 3$ yr and various recurrence times.	49
3.9	Calculation of KS 1731-260 for $\tau_{ob} = 12$ yr, $\tau_{rec} = 1500$ yr, and various mass accretion rates.	50
3.10	The ratio L_{acc}/L_{q1} as a function of mass accretion rate.	51
3.11	Lightcurves calculated for MXB 1659-298 with observations normalized to the high-conductivity/standard cooling model.	55
3.12	Lightcurves calculated for MXB 1659-298 with observations normalized to the high-conductivity/enhanced cooling model.	56
3.13	Lightcurves calculated for MXB 1659-298 for various mass accretion rates.	57
3.14	One twelfth of the cooling curve parameter space.	60
3.15	L_{q1} for low conductivity, standard cooling, and $\dot{M}_{ob} = 10^{15}$ g s $^{-1}$	61
3.16	L_{q1} for low conductivity, standard cooling, and $\dot{M}_{ob} = 10^{16}$ g s $^{-1}$	61
3.17	L_{q1} for low conductivity, standard cooling, and $\dot{M}_{ob} = 10^{17}$ g s $^{-1}$	62
3.18	L_{q1} for low conductivity, enhanced cooling, and $\dot{M}_{ob} = 10^{15}$ g s $^{-1}$	62
3.19	L_{q1} for low conductivity, enhanced cooling, and $\dot{M}_{ob} = 10^{16}$ g s $^{-1}$	63
3.20	L_{q1} for low conductivity, enhanced cooling, and $\dot{M}_{ob} = 10^{17}$ g s $^{-1}$	63
3.21	L_{q1} for high conductivity, standard cooling, and $\dot{M}_{ob} = 10^{15}$ g s $^{-1}$	64
3.22	L_{q1} for high conductivity, standard cooling, and $\dot{M}_{ob} = 10^{16}$ g s $^{-1}$	64
3.23	L_{q1} for high conductivity, standard cooling, and $\dot{M}_{ob} = 10^{17}$ g s $^{-1}$	65
3.24	L_{q1} for high conductivity, enhanced cooling, and $\dot{M}_{ob} = 10^{15}$ g s $^{-1}$	65
3.25	L_{q1} for high conductivity, enhanced cooling, and $\dot{M}_{ob} = 10^{16}$ g s $^{-1}$	66

3.26	L_{q1} for high conductivity, enhanced cooling, and $\dot{M}_{ob} = 10^{17} \text{ g s}^{-1}$. . .	66
4.1	Atomic Q -values for nuclei included in the electron capture calculations.	76
4.2	Reaction rates for electron capture on ^{56}Fe	78
4.3	Effective reaction rates for electron capture on ^{56}Fe	82
4.4	Flow chart of the electron capture program.	84
4.5	Abundance plot for the $A = 56$ electron capture chain.	87
4.6	The density curve for the $A = 56$ electron capture chain.	88
4.7	The energy generation for the $A = 56$ chain.	90
4.8	The dependence of the electron capture on the reaction rate for $T = 0.0101 \text{ GK}$	91
4.9	The dependence of the electron capture on the reaction rate for $T = 0.101 \text{ GK}$	91
4.10	The dependence of the electron capture on the effective rate calculation.	92
5.1	The coupled cyclotron facility at the NSCL.	98
5.2	Diagram of the S800 spectrograph at MSU.	100
5.3	Photograph of a timing PPAC.	101
5.4	Diagram showing a G10 board used in the timing detector.	102
5.5	Diagram showing the electronic circuitry for PPAC timing measurements.	103
5.6	Plot of the FWHM as a function of bias voltage.	105
5.7	Timing spectrum obtained from the optimum setup during testing. . .	107

Images in this dissertation are presented in color.

List of Tables

3.1	Parameters used for the calculation of the critical temperature.	26
3.2	Reactions occurring in the neutron star crust.	34
3.3	The four physical models used in the cooling calculations.	41
3.4	Neutron star crust properties and ^{12}C ignition properties for various cooling models.	45
3.5	Table of quiescent bolometric flux for different assumed distances to MXB 1659-298.	54
3.6	Parameters used for the study of cooling curves. Refer to Table 3.3 for the definition of the various models.	59
5.1	Production rates for nuclei of interest in the Fe – Ni region.	99

Chapter 1

Introduction

With the launch of the *Chandra X-ray Observatory* and *XMM-Newton*, many new and exciting observations of neutron stars are being made. Some of these observations have detected transient neutron stars cooling into quiescence. Transient neutron stars go through accretion outburst periods followed by long quiescent intervals. These observations open up new questions as to the interior properties and the thermal evolution of these objects and offer unique opportunities to probe the interior physics of neutron stars. To interpret these observations, accurate models of neutron star crusts are needed. The heating and cooling of accreting neutron stars is determined by nuclear interactions in the crust and the thermal structure of the stellar interior and can be studied by observing the X-ray light output. In addition, laboratory experiments must be made to accurately determine the nuclear physics input for the calculations.

Accretion onto a neutron star releases energy resulting in a luminosity, $L \sim 10^{37}$ erg s⁻¹. When the accretion onto the surface of the star slows or stops, the X-ray luminosity of the object decreases during several months to years, finally leveling out in a quiescent state. Neutron star systems which show such large luminosity changes are known as *transient* low-mass X-ray binary (LMXB) systems. Multiple transient

systems have been observed in a quiescent state where the luminosity, L_q is less than 10^{34} erg s $^{-1}$, e.g. Cen X-4, Aql X-1, KS 1731-260, and MXB 1659-298. The source of this quiescent luminosity is still uncertain. It could be due to continued accretion at a much lower rate than during outburst [152], accretion onto the neutron star magnetosphere [27], or thermal emission from the neutron star core which has been heated by nuclear reactions in the deep crust [22]. Of these three possibilities, the arguments for accretion offer no predictions of the magnitude of the quiescent luminosity. Only the deep-crust heating argument offers predictions of the quiescent luminosity that scale with observations. The heating scenario also offers an explanation of the observed thermal spectrum, though it does not explain the existence of a hard power-law component. It is this deep-crust nuclear heating scenario which is the focus of the present work.

Previous work to study the cooling of neutron stars has mainly focused on isolated neutron stars (see Tsuruta [148] for a review). Studies of the energy sources of transient luminosity concentrated mostly on the atmosphere [46], or on the relationship of cooling to pulsar glitches [34,36,153]. More recently, Colpi et al. [37] studied the effect of non-equilibrium crust reactions on the temperature of the core of transient neutron stars and quantified the variability of quiescent luminosity based on the deep-crust heating model of Brown, Bildsten & Rutledge [22]. The work presented here follows that of Ushomirsky & Rutledge [151], who expanded on the work of Colpi et al. [37] and detailed the time dependence of the crust temperature and the luminosity over a series of short outbursts.

In this work, a calculation was made to follow the thermal evolution of a transient neutron star over a series of outbursts and quiescent periods. The results of these calculations were compared with observations of two long-duration transient neutron stars: KS 1731-260 and MXB 1659-298. In contrast to previous work, these calculations study the effects of different recurrence times and mass accretion rates for the

sources. Calculations of KS 1731-260 are fit to the most recent observation [158] and also include a study of the ignition conditions for explosive ^{12}C burning. Comparison to observations reveals that the calculations agree with the observations for KS 1731-260, but under-predict the quiescent luminosity for MXB 1659-298. Additional physics is necessary to more fully understand these systems, especially in the case of KS 1731-260 where the calculations agree with the luminosity observed but still cannot explain the observed superburst. Nonetheless, constraints can be made on the interior physics of these neutron stars, such as the conductivity of the crust and the material at the center of the star. More observations are needed to better map out the actual cooling curves.

A survey of cooling transient neutron stars will aid in interpreting future and archival observations of quiescent neutron stars which have undergone long outbursts. With this aim, the cooling code was used to make a parameter study of neutron stars cooling into quiescence in order to determine how the cooling curves change with respect to outburst length, recurrence time, and mass accretion rate. The outburst length and accretion rate determine how much heat is deposited in the crust over an outburst, and the recurrence time determines the amount of heat lost during quiescent periods. The thermal conductivity of the crust and neutrino emission from the core also affect the rate at which heat is emitted during quiescence.

The most important input for the cooling calculations is the heat deposited in the crust during outburst events. The amount of heat deposition determines the temperature of the crust before quiescence. This, in turn, determines how the crust cools after the outburst. Detailed studies of the processes taking place in the neutron star crust were initiated by Sato [126], who studied several scenarios with different initial compositions. See, also, the work of Bisnovatyi-Kogan & Chechetkin [18]. Vartanyan & Ovakimova [154] studied aspects of the energy release, though they used a rather unrealistic model of neutron star material, and Fujimoto et al. [52] showed that the

energy release in the crust is greater than the inward heat flow due to hydrogen burning in the outer layers. Haensel & Zdunik [66,67] made additional calculations of the energy release for electron captures and density-dependent pycnonuclear reactions assuming a zero-temperature crust composed of one species at each depth. The work presented here continues these studies by calculating the depth and thickness of these reaction layers using a network calculation which implements a realistic thermal model in conjunction with all the relevant nuclear physics.

Since the nuclei involved in the electron captures are far from the valley of β -stability, many of the nuclear properties necessary to calculate the electron capture reaction rates and other nuclear processes relevant to astrophysics are available only from theoretical models. Experiments must be made to provide accurate data as input for these calculations; of primary interest are the masses of these exotic nuclei. An experiment has been proposed at the National Superconducting Cyclotron Laboratory (NSCL) at Michigan State University (MSU) to make time-of-flight mass measurements of nuclei in the ^{70}Fe region. ^{70}Fe is also believed to be a waiting point in the rapid neutron (r-) process, and data about this nucleus will be useful in r-process calculations. The production rates of such exotic nuclei are estimated to be quite low, so it is necessary to construct gas detectors for use in these measurements. Gas detectors have the advantage that the particle energy loss in the detector is minimal. A pair of stacked parallel-plate avalanche counters (PPACs) for use in such an experiment were designed, built, and tested. It was found that the resolution of these detectors in the current design is not yet suitable for use in mass measurements requiring a high time precision.

Chapter 2 provides the history and background of neutron stars. A description of the calculation used to simulate the cooling of transient neutron stars is presented in Chapter 3. Comparisons to observations are discussed, and a study of the parameters involved is also described. Calculations of electron capture reactions under steady

accretion in parallel with the thermal equations are explained in Chapter 4. The discussion includes the dependence of the reaction layers on the temperature, Q -value, and phase space calculation. Chapter 5 covers the design and testing of a pair of timing PPACs for use in time-of-flight mass measurements. Conclusions and suggestions of future work are included in Chapter 6.

Chapter 2

Background

First hypothesized by Baade & Zwicky in 1934 [8], the first neutron star models were made by Oppenheimer & Volkoff in 1939 [110], in which they modeled the neutron star matter as an ideal gas of free neutrons near nuclear density and developed the relativistic stellar structure equations. More details were added to the models in the following years, which concentrated on describing the equation of state in the neutron star [1, 26, 68, 69]. It was not until 1967 that the first observational signature of neutron stars was found [73]. With the discovery the following year of the Crab and Vela pulsars situated in supernova remnants [133, 143], the connection between neutron stars and massive stars was confirmed. Following this, in 1975 Hulse & Taylor discovered the first binary neutron star [74], leading to the measurement of neutron star masses.

Neutron stars in accreting binary systems are host to a wide variety of observational phenomena. In some systems, the accretion may slow or stop, and stars with a high accretion luminosity will begin to decrease in brightness. Neutron stars exhibiting high-luminosity accretion outbursts followed by long quiescent periods are known as *transient* neutron stars. Observations of such cooling neutron stars offer the opportunity to determine properties of the stellar interior by comparison with

theoretical calculations. The rate of cooling after accretion ends is dependent on the energy deposited in the crust during accretion, the state of matter in the crust, and which type of material lies at the center of the star. The cooling curve will also be affected by the equation of state throughout the star. In one case, a transient neutron star has exhibited a superburst (Section 2.4.2) during the accretion phase, which places additional constraints on the composition and physics of the interior [20].

Sections 2.1 and 2.2 set up the environment of transient neutron stars. More detail about these systems, including observations is given in Section 2.3. Thermonuclear bursts as evinced by transient neutron stars are described in Section 2.4, and some observational aspects of the problem are collected in Section 2.5.

2.1 Neutron star structure

Neutron stars are believed to be the result of core-collapse supernova explosions. Typical interior temperatures of the star at birth are $T \gtrsim 10^{11}$ K, which cool to $10^9 - 10^{10}$ K through neutrino emission within a couple of days. Surface temperatures several hundred years later, at 10^6 K, are a bit lower than the interior. At such high interior temperatures, the matter can be considered as being in thermodynamic equilibrium, and the material in which all possible interactions have completed is termed *cold catalysed matter* [134]. It is on this basis that static models of neutron stars are constructed. However, accretion of matter from a secondary star onto the neutron star (Section 2.2) can produce regions of the neutron star crust in which the matter is not in its ground state. Many crust characteristics of neutron stars are dependent on the composition, including the thermal structure [23, 66], neutrino energy loss [53], and possible gravitational wave emission [17, 137]. The crust composition may also give insight into the evolution of magnetic fields in such extreme environments.

The basic structure of a neutron star is illustrated in Figure 2.1. For neutron

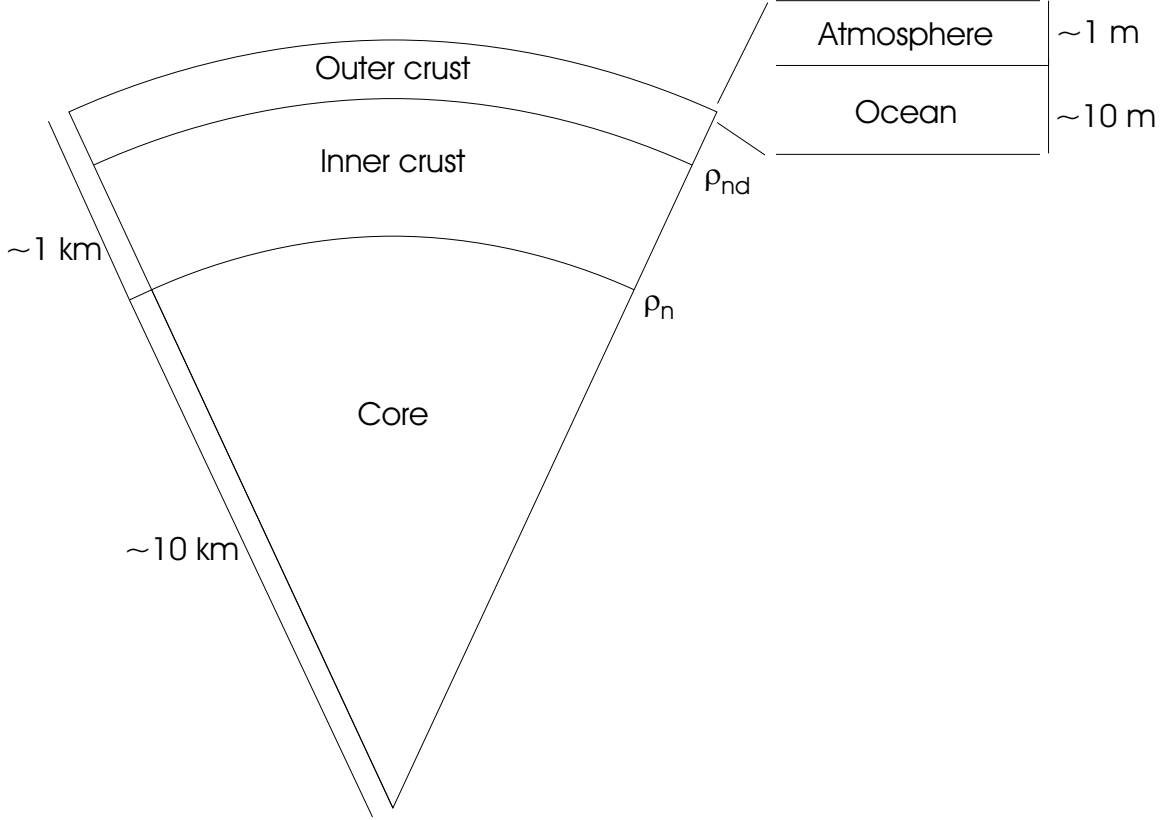


Figure 2.1: Internal structure of the neutron star showing the transitions between the outer crust, inner crust, and core. Above the outer crust lie the thin atmosphere and ocean. Here, ρ_{nd} is the neutron-drip density and ρ_n is the nuclear saturation density.

stars accreting matter with a solar abundance pattern, matter falls onto the gaseous atmosphere and is burned there via the rapid proton (rp-) process originally described by Wallace & Woosley [155], producing an X-ray burst (Section 2.4.2). The result of this process is a mix of nuclei from He up through Te, with the most abundant nuclei around $A \sim 60$ [165] and $A \sim 104$ [130]. No hydrogen remains at the end of the process at a density of $\sim 10^6 \text{ g cm}^{-3}$, though further burning of helium may occur. The ashes of this burning get forced into the neutron star crust by continued accretion, replacing the original crust in $\sim 10^6 \text{ yr}$. At a density of $\sim 10^9 \text{ g cm}^{-3}$ carbon may ignite, resulting in a superburst, an explosion a thousand times more energetic than a regular X-ray burst (Section 2.4.2).

Upon further accretion, the matter is pressed into the outer crust of the neutron

star. At a density of $\sim 10^9$ g cm $^{-3}$ the Fermi energy of electrons has risen high enough that electron captures may occur [66, 126]. Here, nuclei are arranged in a lattice surrounded by free relativistic electrons. Free neutrons are also present in the inner crust which begins at the neutron-drip density, ρ_{nd} . The electron captures are interspersed with pycnonuclear fusion reactions as the density of the matter increases even further. This continues down to the crust/core interface at a density near the nuclear saturation density, ρ_n . Just above the core/crust boundary, nuclei are more stable in non-spherical configurations such as planar or cylindrical geometries known as *nuclear pasta* [70, 121]. Further increases in pressure cause the nuclei to disintegrate into individual nucleons which are then incorporated into the core. The central density of a neutron star may be higher than 10^{15} g cm $^{-3}$. It is as yet unclear what sort of matter lies at the heart of a neutron star. The nuclei disintegrate, but the constituent products are unknown. The core could be composed of a gas of neutrons and protons, nuclei mixed with pions [10, 11], kaons [84, 106], or hyperons [16], or the nucleons could decompose further into a gas of quarks [3, 82, 164].

2.2 Binary systems and accretion

Transient neutron stars reside in low-mass X-ray binary (LMXB) systems, which are composed of a neutron star and a low-mass ($M < 1 M_\odot$) companion. The presence of a slightly evolved low-mass star in the system indicates an old star, and as such, these are Population II stars found in the galactic bulge and in globular clusters. In the standard scenario, a binary system forms and the more massive star later evolves into a neutron star, though tidal capture processes are also a likely scenario if the kinetic energy of the system can be dissipated rapidly [47]. Reviews of binary system evolution are given by Canal, Isern & Labay [29] and Iben [75].

In LMXBs, accretion of material from the secondary to the neutron star takes

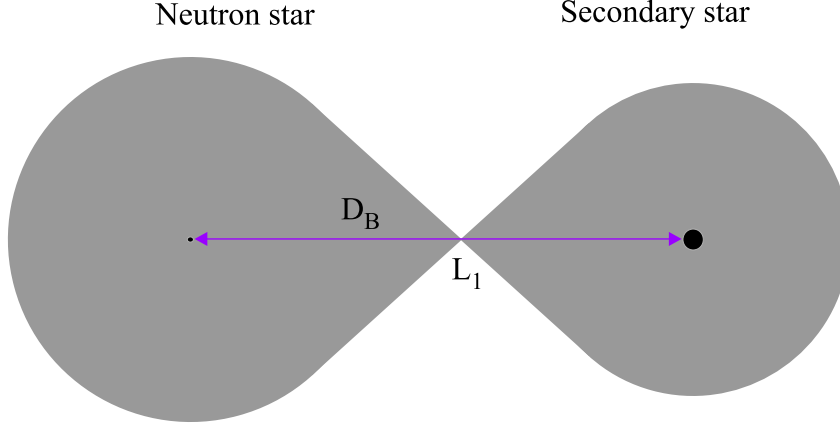


Figure 2.2: Illustration of the Roche lobes in a binary system. The Lagrange point, L_1 , and the separation distance, D_B , are shown.

place when the secondary fills its Roche lobe and begins to overflow through the Lagrange point. The Roche lobes are formed by the equipotential surfaces of each object, which are distorted by centrifugal force effects (Figure 2.2). Typical separation distances between the primary and companion stars are between 0.001 and 1 AU.

Several effects may lead to a Roche lobe overflow. Interior evolutionary changes of a star will cause it to expand and fill up its Roche lobe. Conversely, the orbit may shrink due to angular momentum loss through either a stellar wind or gravitational wave emission. The rate at which the companion star initially loses mass through the Lagrange point depends on the structure of the star at the moment the Roche lobe is filled, the degree to which orbital angular momentum and mass are conserved in the system, and the response of the companion to accretion.

Matter from the companion star does not fall directly onto the neutron star, but first piles up in the accretion disk to conserve angular momentum, and then flows onto the surface of the neutron star. Total mass accretion rates are typically $10^{15} - 10^{18}$ g s^{-1} . A limit exists to the total luminosity a star can emit and still remain in hydrostatic equilibrium. This quantity is known as the Eddington luminosity, and is given by

$$L_{\text{Edd}} = \frac{4\pi cGM}{\kappa} = 1.3 \times 10^{38} \left(\frac{M}{M_{\odot}} \right) \text{ erg s}^{-1}, \quad (2.1)$$

where M and R are the mass and radius of the star, and κ is the atmospheric opacity. If the luminosity exceeds L_{Edd} , the star will expand due to radiation pressure.

The Eddington mass accretion rate is defined as the rate at which the gravitational energy released by the in-falling matter generates the Eddington luminosity. Assuming Thomson scattering is the only opacity source, this is denoted as [129]

$$\dot{m}_{\text{Edd}} = \frac{2m_{\text{p}}c}{(1+X)R\sigma_{\text{T}}} = 8.8 \times 10^4 \left(\frac{1.71}{1+X_{\text{H}}} \right) \left(\frac{10 \text{ km}}{R} \right) \text{ g cm}^{-2} \text{ s}^{-1}, \quad (2.2)$$

where X_{H} is the hydrogen mass fraction of accreted material, m_{p} is the proton mass, and σ_{T} is the Thomson cross section. A neutron star can locally accrete matter faster than \dot{m}_{Edd} , in which case the radiation spreads out over the surface of the star, eliminating the need for expansion.

2.3 Neutron star transients

As previously mentioned, the accretion in some binary systems may turn off, allowing the neutron star to cool into a low-luminosity quiescent state. This is believed to be the mechanism behind X-ray transients. The difference between transients and persistent sources is not patent, but may be defined as an object whose luminosity changes by $\gtrsim 3$ orders of magnitude [122]. These systems exhibit long periods (years to decades) of low X-ray luminosities ($< 10^{34} \text{ erg s}^{-1}$) separated by short outbursts lasting weeks to months and characterized by luminosities of $10^{36} - 10^{38} \text{ erg s}^{-1}$ [33]. As an example of the behavior of these sources, Figure 2.3 shows the lightcurve of the well-studied Aquila X-1 as observed with *RXTE*/ASM. For details of *RXTE* see Section 2.5. This source exhibits a variable luminosity in quiescence, below the flux threshold of *RXTE*/ASM. The quiescent luminosity of transient neutron stars in general has been shown to vary by a factor of 3 – 5 on timescales of years to days [27, 58, 122, 123, 152], though the cause of the fluctuation is as yet unknown. A number of scenarios are

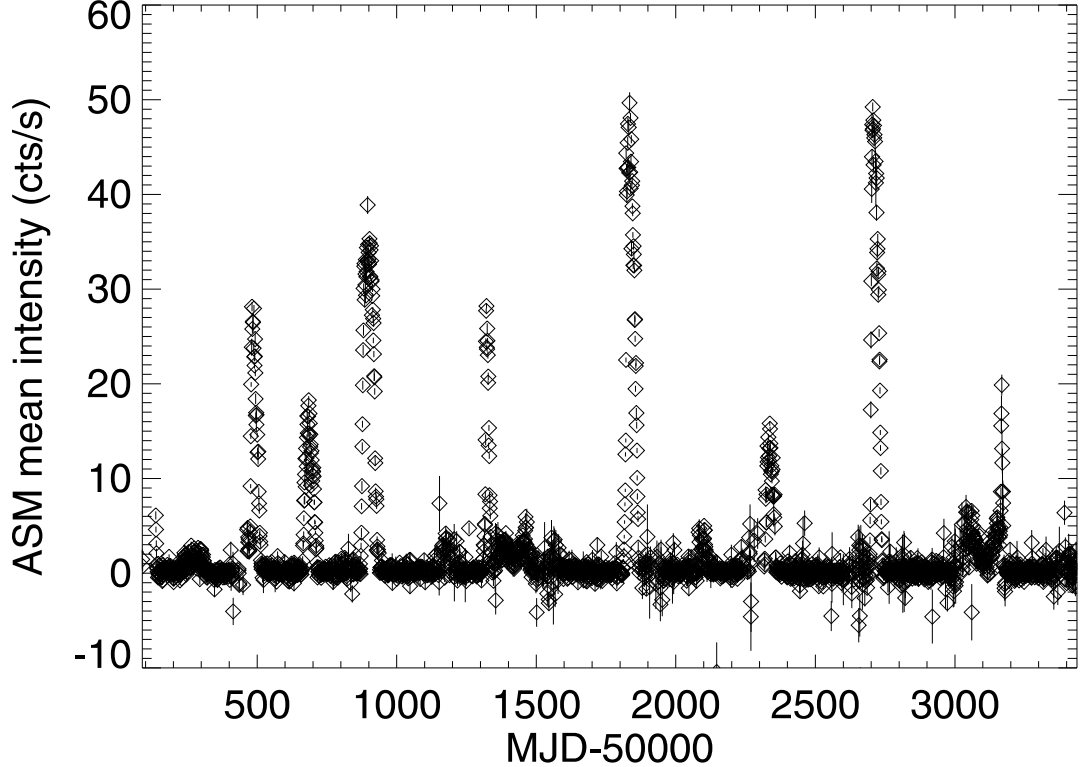


Figure 2.3: The lightcurve of Aquila X-1 as observed with *RXTE*/ASM. The short outburst length and ~ 220 day recurrence time is evident.

variable accretion onto the neutron star surface [172], variable accretion onto the magnetosphere [28], or a variable absorption column density (N_{H}) [122].

A subclass of transients is characterized by very long outburst periods lasting years to decades instead of weeks to months. These sources include MXB 1659-298 and KS 1731-260, as well as EXO 0748-676 [113], 4U 2129+47 [116,117], and X 1732-304 (Terzan 1) [77,98]. One of these sources, KS 1731-260, recently turned off after accreting for more than 12 yr [159]. Its lightcurve is shown in Figure 2.4 [159]. Note that the lightcurve declines rapidly, yielding clues as to the properties of the accretion behavior.

Of these systems, EXO 0748-676 and X 1732-304 seem to have been in outburst for ~ 15 yr. MXB 1659-298 has shown two outbursts of 2.5 yr duration with a 20 yr quiescent period. 4U 2129+47 was originally thought to be a persistent source, so its outburst length is unknown. Due to the long outburst duration, the neutron

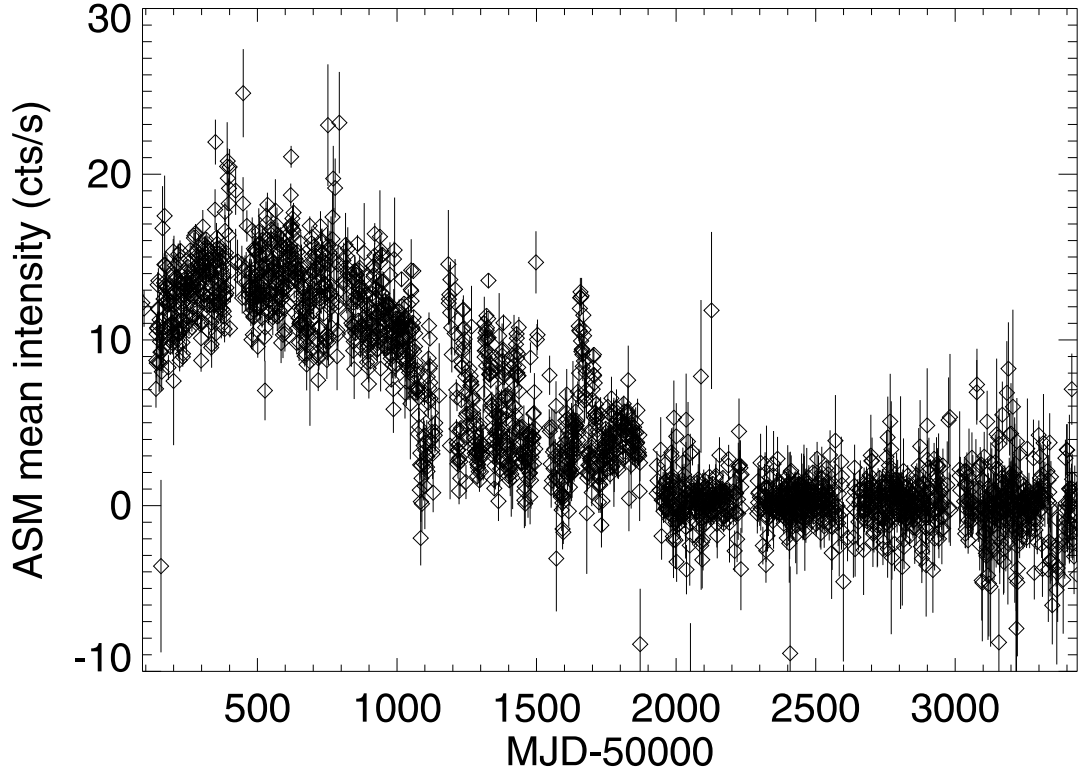


Figure 2.4: The lightcurve of KS 1731-260 as observed with *RXTE*/ASM.

star crust is presumed to heat much more than for short outbursts (e.g. Aql X-1); thus it has been estimated that the quiescent periods are longer as well, lasting up to centuries. However, it will be shown in this work that the length of the recurrence time for certain models is not necessarily constrained. Of the sources listed above, EXO 0748-676 and X 1732-304 seem to be brighter in quiescence than the other systems [58, 113, 157]. Differences between the systems give indications about the physics of the stellar interior, possibly indicating that these two sources have crusts with a lower conductivity.

2.4 Thermonuclear bursts

Most neutron star transients reveal thermonuclear bursts during outburst periods. The presence of X-ray bursts confirms that the primary in an X-ray emitting system

is a neutron star, and indicates a low magnetic field strength of $B < 10^9$ G. Only one transient neutron star (KS 1731-260) has shown a superburst, and this observation places many additional constraints on the thermal properties of the neutron star crust.

2.4.1 X-ray bursts

X-ray bursts were discovered in 1975 by both Grindlay et al. [63] and Belian, Conner & Evans [15]. Shortly after, Maraschi & Cavaliere [99] and Woosley & Taam [166] discussed the possibility that the bursts were a result of thermonuclear burning of hydrogen and helium on the surface of accreting neutron stars. The rp-process [155] synthesizes the accreted matter via a series of proton captures and β -decays along the proton-drip line. X-ray bursts last several seconds to minutes, producing a luminosity of $10^{36} - 10^{38}$ erg s⁻¹. It was shown for a one-zone model that when this process reaches the Te isotopes, further burning is halted by the Sn-Sb-Te cycle [130], whereby the strongly α -unbound ¹⁰⁴Te decays back to Sn. Figure 2.5 shows the reaction flow of the rp-process for a one zone, steady-state model illustrating the Sn-Sb-Te cycle. The reaction flow is dominated by the 3α reaction for nuclei lighter than ¹²C, by the (α ,p) process from ¹²C to ²⁵Al, and by the rp-process for heavier nuclei. Multi-zone models [165] indicate that in subsequent bursts the burning does not reach this point, instead creating nuclei of $A \approx 64$.

X-ray bursts have been observed from ~ 60 sources. Typical rise times are less than 2 s, but some cases have exhibited rise times up to 10 s. Typical decay times range from about 10 s to several minutes. The interval between bursts can range from about 5 min up to days, but the behavior can be either regular or irregular. The base luminosity of X-ray burst sources is not zero since continual accretion of matter releases about 200 MeV/u in gravitational energy. In comparison, the rp-process releases 6.9 MeV/u. Despite being much less energetic than the gravitational energy release, the X-ray burst is visible above the accretion-powered background

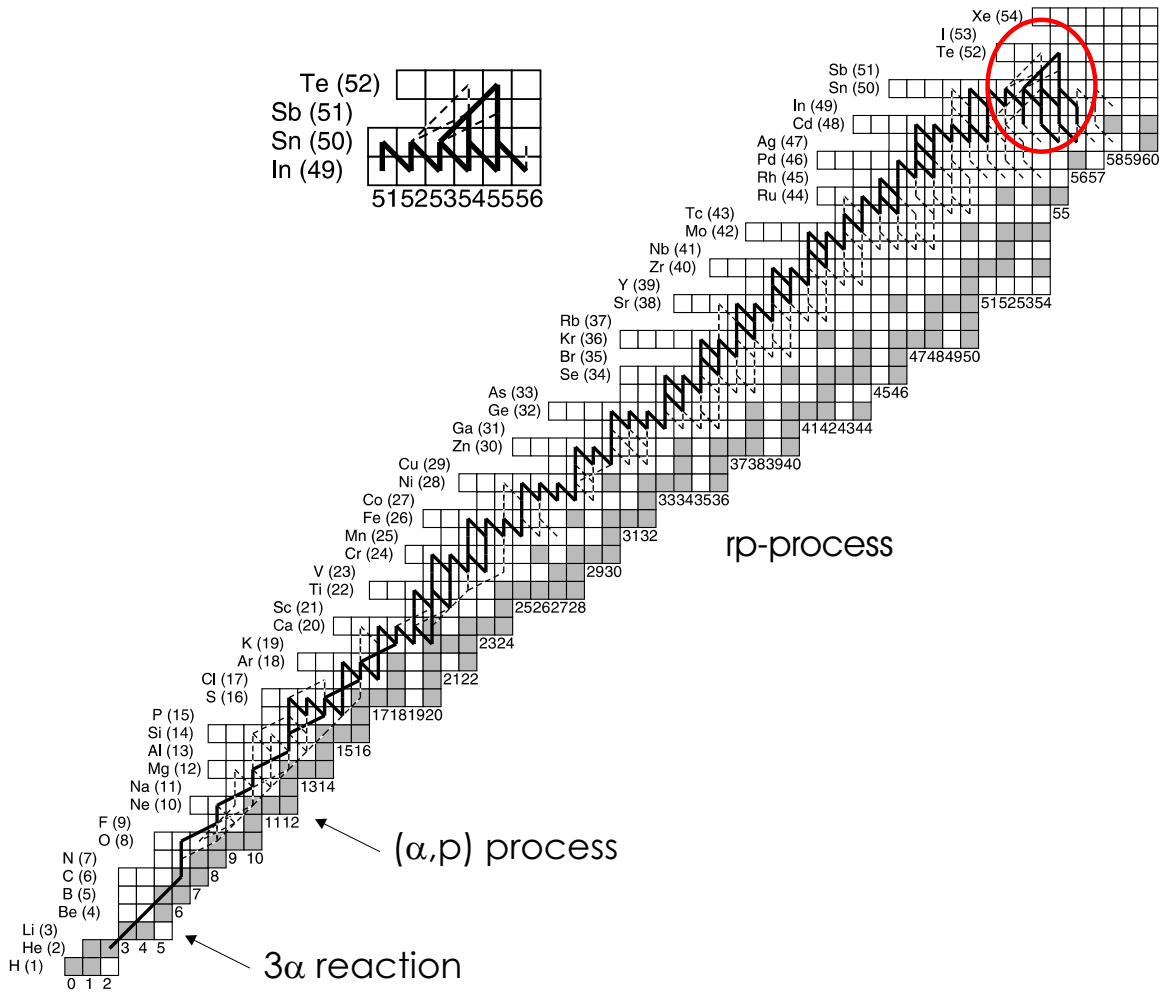


Figure 2.5: The reaction flow of the rp-process illustrating the Sn-Sb-Te cycle (inset). The solid line represents the strongest reaction flow and the dashed line represents a weaker flow.

since all of the energy is released in a short time. The fluence of the X-ray burst over its duration, $\sim 10^{39}$ erg, therefore, is much larger than the fluence due to gravitational energy in the same amount of time.

2.4.2 Superbursts

Superbursts are thermonuclear events similar to type I X-ray bursts: they have a rapid rise and an exponential decline. However, the duration is 1000 times longer than a normal burst, making the total energy output 1000 times greater. Nine superbursts from seven sources have been detected: KS 1731-260 [86], 4U 1735-44 [41], 4U 1636-536 [87], GX 3+1 [85], 4U 1820-303 [138], Ser X-1 [42], and 4U 1254-69 [79]. Four additional flares which have superburst characteristics have been discovered from G 17+2 [76] recurring on the order of weeks, though it is not certain whether these flares are superbursts. The recurrence time between superbursts is uncertain, although one source (4U 1636-536) has exhibited three superbursts over a period of $\simeq 4.7$ yr [87, 139, 156].

Cumming & Bildsten [44] and Brown & Strohmayer [138] proposed the ignition of ^{12}C in the outer crust as the source of these superbursts, and they predict that superbursts should occur for any source with a luminosity above $0.1 L_{\text{Edd}}$, and should occur with a recurrence time of a few years. Figure 1 in the Cumming & Bildsten [44] paper plots the temperature required to ignite ^{12}C at a given depth, which is approximately 5×10^8 K for a depth of 10^{12} g cm^{-2} . Schatz et al. [131] showed that for low mass accretion rates ($0.1 - 0.3 \dot{m}_{\text{Edd}}$), significant amounts of carbon and heavier elements remain in the ashes of the rp-process in X-ray bursts. The mass fraction of ^{12}C is somewhat below the 10% required by Cumming & Bildsten [44], though more work is needed to determine under which conditions enough ^{12}C is made to fuel superbursts. The work of Wallace & Woosley [155] showed that ^{12}C produced in the rp-process is destroyed by subsequent bursts due to helium burning.

For stable burning, significant amounts of ^{12}C remain up to mass accretion rates of $1 \dot{m}_{\text{Edd}}$, and accreted matter enriched in helium above the solar abundance means that more ^{12}C remains at the end of the rp-process. However, superburst sources also exhibit regular X-ray bursts, so superbursts should occur in the unstable burning regime. Therefore, the origin of the ^{12}C fuel for superbursts is still an open question. As to the source of energy in superbursts, Schatz et al. [127] showed that the high temperatures found in superbursts ($T > 10^9$ K) lead to photodisintegration reactions, transforming the heavy nuclei into iron-group elements. Furthermore, they showed that depending on the initial composition, photodisintegration can be the dominant source of energy in superbursts.

2.5 Observations

Because the Earth's atmosphere absorbs X-rays, observations cannot be made from the ground, and it is necessary to place X-ray telescopes in orbit. Proportional counters and scintillators flown on rocket and balloon flights in the 1960s detected the first extra-solar X-ray source, Sco X-1 [59]. Additional discoveries include X-rays from the Sun, gamma-ray bursts, and X-rays from supernova remnants. The first X-ray satellite was *Uhuru*, launched by NASA in the early 1970s, which discovered the first X-ray emitting neutron stars. Several more satellites were launched in the following years, and four X-ray telescopes launched in the last decade have contributed to and greatly expanded X-ray astronomy. These are the *Rossi X-ray Timing Explorer (RXTE)*, *BeppoSAX*, *XMM-Newton*, and the *Chandra X-ray Observatory (Chandra)*.

Launched in 1995, *RXTE* is useful for studying rapid time variability over a wide range of energies. Its All Sky Monitor (ASM) surveys 80% of the sky every orbital period (90 min) over the energy range 2 – 10 keV. *BeppoSAX* was retired in 2003, but was useful due to its many instruments sensitive to a wide range of energies: 0.1 – 300

keV. It had imaging capabilities of $1.5' - 3'$ FWHM. Both *XMM* and *Chandra* have lower flux thresholds than *RXTE*, and so are useful for observing sources such as KS 1731-260 after they have decreased in luminosity below the *RXTE* threshold. *XMM* is capable of returning X-ray spectroscopic data in the energy range $0.1 - 12$ keV and is a nice complement to *Chandra*, which can view objects more than twice as far as previously launched telescopes and also offers very detailed images. *Chandra* has a high angular resolution ($0.5''$) for its 1.0° field of view and it has a moderate energy range of $0.09 - 10$ keV over all of its instruments.

For observers, properties of the neutron star are altered by the gravitational redshift as follows: for the observed luminosity,

$$L_\infty = L \left(1 - \frac{r_g}{R}\right), \quad (2.3)$$

the observed effective temperature,

$$T_{S,\infty} = T_S \sqrt{1 - \frac{r_g}{R}}, \quad (2.4)$$

and the observed stellar radius,

$$R_\infty = R \left(1 - \frac{r_g}{R}\right)^{-1/2}. \quad (2.5)$$

Here, $r_g = 2GM/c^2$ is the gravitational radius [144]. Luminosities, temperatures, and radii discussed in this work are proper, and not redshifted, quantities.

Chapter 3

The Cooling of Neutron Star Transients

3.1 Description of the model

To understand how the crust of a neutron star responds to heating and cooling, the time-dependent thermal balance equation was solved for four different crust/core models following the work of Ushomirsky & Rutledge [151]. The dependence of the quiescent luminosity on outburst length, recurrence time, accretion rate, and stellar model were studied. During outbursts, nuclear reactions heat the stellar interior, and during quiescence the crust cools through thermal and neutrino emission. The equation of state follows that used in Brown [23].

3.1.1 Thermal balance in the crust

The entropy equation describes the balance of thermal energy in a neutron star crust and is expressed as

$$T \frac{dS}{dt} = -\frac{1}{\rho} \nabla \cdot \mathbf{F} + \epsilon, \quad (3.1)$$

where T is the temperature, S is the entropy, ρ is the mass density, \mathbf{F} is the flux, and $\varepsilon = \varepsilon_N + \varepsilon_\nu$ represents sources and sinks of energy. Because the crust is very thin compared to the radius of the neutron star (Figure 2.1), the general relativistic corrections enter the calculation only through the relativistic gravity. The flux is given by Fick's Law, $\mathbf{F} = -K\nabla T$, where K is the thermal conductivity (Section 3.1.2). In plane-parallel coordinates the flux equation may be rewritten as

$$\frac{\mathbf{F}}{K\rho} = \frac{\partial T}{\partial y}, \quad (3.2)$$

where $y = \int \rho dr = P/g$ is the column depth. Here, P is the pressure, and g is the gravity.

Using the flow velocity, $u = \dot{m}/\rho$, where \dot{m} is the accretion rate per unit area, and the thermodynamic relation

$$\left(\frac{\partial s}{\partial P}\right)_T = -\left(\frac{\partial T}{\partial P}\right)_s \left(\frac{\partial s}{\partial T}\right)_P, \quad (3.3)$$

a number of simplifications can be made to transform the left-hand side of Equation (3.1) into a more useful form [21]:

$$T \frac{dS}{dt} = c_P \left[\frac{\partial T}{\partial t} + \dot{m} \frac{\partial T}{\partial y} \right] - \frac{c_P T \dot{m}}{y} \nabla_{ad}, \quad (3.4)$$

where c_P is the specific heat at a given pressure. The adiabat is $\nabla_{ab} \equiv (\partial \ln T / \partial \ln P)_s$. Further simplification may be made by treating all terms containing \dot{m} as negligible [21] since the energy produced by compressional heating in the crust is small compared to the energy released by nuclear reactions. Because \dot{M} is small ($\dot{M} \sim 10^{-11} - 10^{-8} M_\odot \text{ yr}^{-1}$), the total mass accreted before the crust reaches a steady state is small, and the mass of the atmosphere, therefore, stays roughly constant over the period of accretion. Thus, matter which gets pushed onto the star is incorporated into crust

at same rate as matter at the bottom of the crust is forced into core material, which keeps the flux of matter through the layers constant, maintaining a static structure. Combining Equation (3.1) and the relevant terms from Equation (3.4) leaves

$$c_P \frac{\partial T}{\partial t} = -\frac{1}{\rho} \nabla \cdot \mathbf{F} + \varepsilon. \quad (3.5)$$

The sources of energy, ε_N , (Section 3.1.2) in the neutron star crust are the electron captures throughout the crust with pycnonuclear reactions and neutron emission in the inner crust. Energy in the form of non-interacting neutrinos, ε_ν , leaves the neutron star primarily through bremsstrahlung neutrino interactions in the crust.

The timescale for heat to diffuse through a given thickness from a radius r_o to r can be obtained from Equation (3.5) and is given by [72]

$$\tau_{cool} \simeq \frac{1}{4} \left[\int_{r_o}^r \left(\frac{\rho c_P}{K} \right)^{1/2} dr \right]^2. \quad (3.6)$$

The calculation of the cooling rate for heat to reach the top of the crust and the core for two mass accretion rates is shown in Figure 3.1. The cooling timescale to the core agrees well with the calculations of Ushomirsky & Rutledge [151], and the timescale to the top of the crust is in agreement with the calculation of Brown, Bildsten & Rutledge [22]. As is clear in Figure 3.1, the thermal time in the inner crust is longer than for layers toward the surface, so the heat deposited in in deep layers is spread out radially before it reaches the surface. This means that while individual reactions in the outer layers may be visible observationally, heat from reactions in the inner layers will merge together before reaching the surface, so individual reaction layers of the deep crust will not be observable. This is also a result of the difference in column depth between the reaction layers: those in the outer crust are more separated than those in the inner crust.

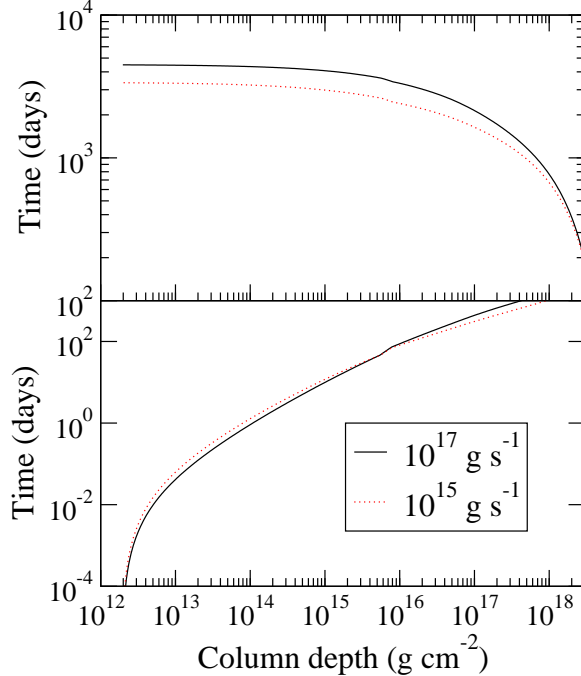


Figure 3.1: The time for heat to diffuse from a given column depth to the top of the crust (bottom panel) and to the core (top panel). Two mass accretion rates are shown: $\dot{M} = 10^{15}, 10^{17} \text{ g s}^{-1}$. Note that most of the nuclear energy is produced around $y \sim 10^{16} \text{ g cm}^{-3}$.

3.1.2 Physical input

The mass of the neutron star was set to $1.4 M_{\odot}$ and the radius, R , was set equal to 10 km at a density of 10^9 g cm^{-3} . Relativistic gravity was used, where $g = GM/(R^2 e^{\phi})$, with $e^{\phi} = \sqrt{1 - r_g/R}$ [144]. The inner boundary, which is defined as the core/crust interface, was set to a density of $1.6 \times 10^{14} \text{ g cm}^{-3}$, slightly below the transition density specified by Brown [23]. The density calculated here and the one cited by Brown [23] are in agreement with Pethick et al. [114] and Akmal et al. [2]. These stellar properties yield a crust mass of $0.01 M_{\odot}$ and a thickness of about 0.3 km. The composition is taken from the electron capture calculations of Haensel & Zdunick [66] with the assumption that a single species of $\langle Z \rangle$ and $\langle A \rangle$ exists at any given depth.

Equation of state

The equation of state was taken from Brown [23], and a plot of it is shown in Figure 3.2. The pressure is composed of contributions from electrons, ions, and neutrons. The electrons in the crust are relativistic and degenerate. The equation of state of the electrons is provided in a table of the Helmholtz free energy from Timmes & Swesty [146]. The ion pressure is calculated from derivatives of the Helmholtz free energy with respect to the ionic free energy which can be expressed as a function of

$$\Gamma = \frac{Z^2 e^2}{k_B T} \left(\frac{4\pi}{3} n \right)^{1/3} = 5.9 \times 10^5 \left(\frac{Z^2}{T} \right) \left(\frac{X_i}{A} \rho \right)^{1/3}. \quad (3.7)$$

This is simply the ratio of the Coulomb energy of a Wigner-Seitz cell to the thermal energy, where n is the number density of nuclei, Z is the charge number, and A is the mass number. $X_i = 1 - X_n$ is the mass fraction of nuclei, where X_n is the mass fraction of neutrons. If $\Gamma \ll 1$ the ions will behave as an ideal gas. For temperatures and densities of interest to this calculation, $\Gamma \gg 1$, so matter in the neutron star crust is not in a gaseous state. When the Coulomb energy becomes comparable to the thermal energy, $\Gamma \sim 1$, the ions will be affected by the Coulomb field, and become strongly-coupled, i.e. interactions between particles become non-negligible. The equation of state for matter in this phase was taken from Chabrier & Potekhin [31], who considered a one-component plasma including electron screening effects. At some point — calculated by Brown to be $\Gamma = 178$ — the ions will settle into a lattice configuration. This transition is given by the intersection of the free energies of the liquid and solid states. The equation of state for the lattice comes from fits to simulations made by Farouki & Hamaguchi [48], who modeled the molecular dynamics of a one-component, strongly-coupled plasma. The binding energy of the nuclei is calculated from the compressible liquid drop model of Mackie & Baym [96], which, in the limit of single nucleons, accounts for the surrounding neutron gas as well.

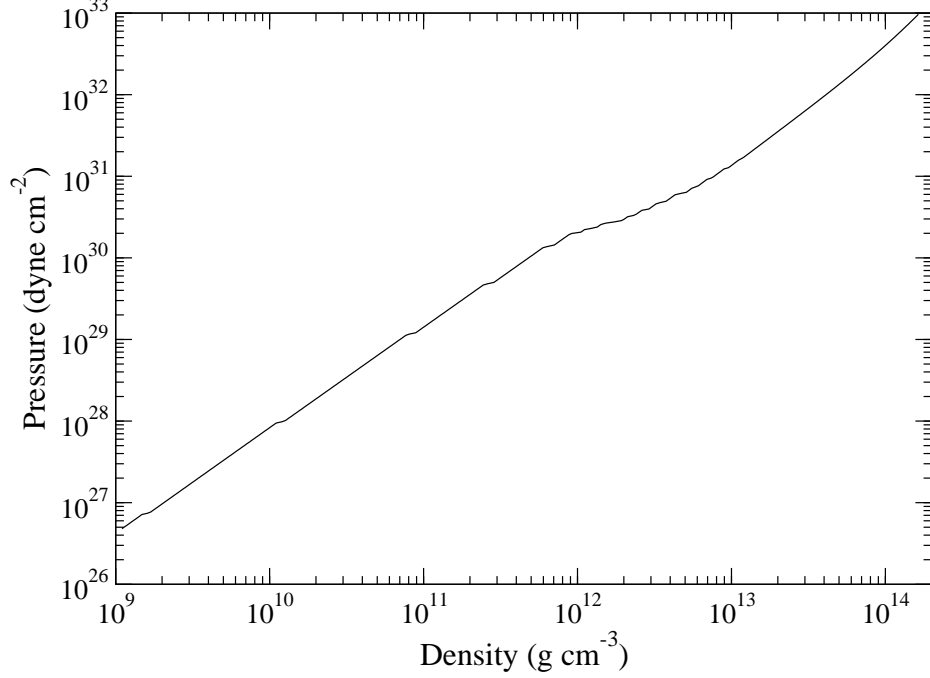


Figure 3.2: Pressure as a function of density in the neutron star crust. Notice that there are discontinuities in the density where electron captures occur.

Specific heat

The total specific heat in the crust is the sum of contributions from electrons, ions, and free nucleons. Electrons in the crust behave as a strongly degenerate, ultra-relativistic gas. The heat capacity per electron is then [169]

$$C_e = \frac{m_e^* p_{F,e} k_B^2 T}{3\hbar^3} \approx 5.67 \times 10^{19} \left(\frac{n_e}{n_0} \right)^{2/3} T_9 \text{ erg cm}^{-3} \text{ K}^{-1}, \quad (3.8)$$

where $n_e = (Z/A)X_i N_A \rho$ is the number density of electrons, $m_e^* \approx p_{F,e}/c$, and $p_{F,e}$ is the electron Fermi momentum. The number density $n_0 = 0.16 \text{ fm}^{-3}$ is the standard nuclear saturation density. For free nucleons, as in the case for neutrons in the inner crust, the heat capacity is that of a non-relativistic, degenerate gas [169]:

$$C_{n,0} = \frac{m_n^* p_{F,n} k_B^2 T}{3\hbar^3} \approx 1.61 \times 10^{20} \left(\frac{m_n^*}{m_n} \right) \left(\frac{n_n}{n_0} \right)^{1/3} T_9 \text{ erg cm}^{-3} \text{ K}^{-1}. \quad (3.9)$$

Here, $p_{F,n}$ is the Fermi momentum, n_n is the neutron number density, and $m_n^* \simeq 1$ is the effective mass of the neutron. The effective mass is set equal to one since the interactions between neutrons are presumed to be negligible. Finally, the heat capacity for ions was calculated numerically from the derivatives of the free energy [31, 48].

Superfluidity

The strong force between two nucleons is composed of short-range repulsive interactions and attractive interactions at larger distances. In the inner crust, a certain fraction of neutrons are free, and the average inter-particle distance is larger than the range of the repulsive interaction. Due to the influence of the attractive interactions, therefore, a macroscopic fraction of the neutrons pair as bosons and occupy a single quantum state. Excitations out of this state require the pair to be broken, necessitating a jump in energy, $\Delta(T)$, the energy gap. Superfluidity affects the equation of state and the thermal state of the star through the neutron specific heat. The effects of superfluidity on the cooling timescale are complicated by normal fluid components and the behavior of the specific heat near the critical temperature.

Neutrons will become superfluid if the temperature falls below a certain critical temperature, T_c . Protons in the crust are bound in nuclei and are thus not subject to superfluidity. At densities lower than about nuclear density, neutrons pair in a singlet state, and they pair in a triplet state for higher densities. The critical temperature is dependent on the Fermi wavevector, $k_F = (3\pi^2 n)^{1/3}$, and a fit to the critical temperature calculations may be expressed as [23]

$$T_c(k) = T_{c,0} \left[1 - \frac{(k_F - k_0)^2}{(\Delta_k/2)^2} \right]. \quad (3.10)$$

The parameters $T_{c,0}$, k_0 , and Δ_k depend on the state of the matter (Table 3.1) and were chosen to reproduce the transition temperatures of Amundsen & Østgaard [4] for

Table 3.1: Parameters used for the calculation of the critical temperature.

State	T_c (MeV)	k_0 (fm $^{-1}$)	Δ_k (fm $^{-2}$)
neutron 1S_0	0.802	0.7	1.2
neutron 3P_2	0.0776	2.0	1.6
proton 1S_0	0.345	0.7	1.0

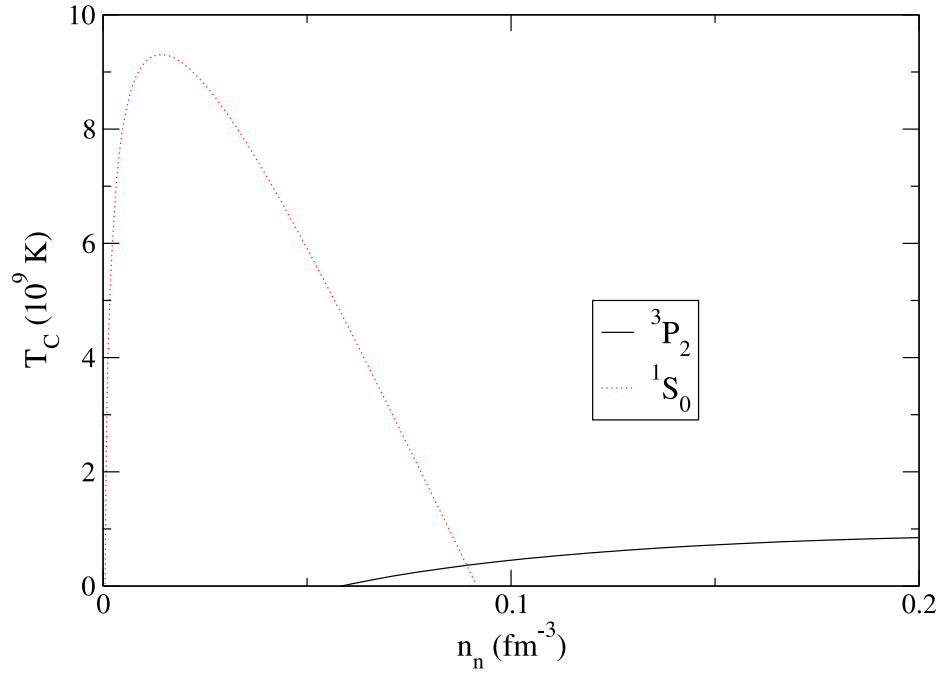


Figure 3.3: The calculation of the critical temperature, T_c , as a function of density for the singlet and triplet states of neutrons. Matter with a temperature below T_c for either case will be in a superfluid state.

the singlet state and Amundsen & Østgaard [5] for the triplet state. Equation (3.10) also reproduces the results of Takatsuka & Tamagaki [142]. A plot of the critical temperature in the neutron star crust is shown in Figure 3.3. It is clear that neutrons at $\rho \gtrsim 6 \times 10^{11}$ g cm $^{-3}$ will be superfluid since temperatures in the crust are always below 10^9 K.

Superfluidity was included for the calculation of the specific heat of the neutrons in the inner crust following the formulation of Yakovlev et al. [169]. In general, the heat capacity for superfluid neutrons can be written as $C_n = C_{n,0}R_{sf}$, where $C_{n,0}$ is given by Equation (3.9), and R_{sf} describes how the heat capacity changes due to superfluidity.

Fit expressions for R_{sf} are given for the different pairings of neutrons [93]:

$$R_{sf}(^1S_0) = \left(0.4186 + \sqrt{(1.007)^2 + (0.5010v)^2}\right)^{2.5} \exp\left(1.456 - \sqrt{(1.456)^2 + v^2}\right) \quad (3.11)$$

$$R_{sf}(^3P_2) = \left(0.6893 + \sqrt{(0.790)^2 + (0.2824v)^2}\right)^{2.5} \exp\left(1.934 - \sqrt{(1.934)^2 + v^2}\right). \quad (3.12)$$

Here, $v = \Delta(T)/(k_B T)$ is a dimensionless quantity describing the temperature dependence of the energy gap amplitude. It is a function of $\tau = T/T_c$, and analytical fits to numerical data have been calculated by Levenfish & Yakovlev [93]:

$$v(^1S_0) = \sqrt{1 - \tau} \left(1.456 - \frac{0.157}{\sqrt{\tau}} + \frac{1.764}{\tau}\right) \quad (3.13)$$

$$v(^3P_2) = \sqrt{1 - \tau} \left(0.7893 + \frac{1.188}{\tau}\right). \quad (3.14)$$

Thermal conductivity

The heat in the crust is transported by relativistic electrons, and is given by the Wiedemann-Franz law [170, 173]:

$$K = \frac{\pi^2}{3} \frac{k_B^2 T n_e}{m_e^*} \nu^{-1}. \quad (3.15)$$

Here, $m_e^* = \epsilon_F/c^2$ is the effective mass of an electron where ϵ_F is the Fermi energy and ν is the effective collision frequency [119]. Where ions are liquified, the thermal conductivity is determined by electron-electron and electron-ion scattering: $\nu = \nu_{ei} + \nu_{ee}$, where ν_{ei} is the electron-ion frequency [118, 119, 167, 170] and ν_{ee} is the electron-electron collision frequency [118, 145, 149]. Where ions are crystallized, the conductivity is given by electron-electron, electron-impurity, and electron-phonon scattering: $\nu = \nu_{ee} + \nu_{eQ} + \nu_{ep}$. Here, ν_{ep} is the the electron-phonon frequency [12] and ν_{eQ} is the electron-impurity scattering frequency [170].

Electron-electron interactions are non-negligible only in the liquid phase for weak electron degeneracy where $Z \lesssim 6$, and so are typically negligible over much of the crust. The collision frequency is given by [119, 149]

$$\nu_{ee} = \frac{3\alpha_f^2(k_B T)^2}{2\pi^3 \hbar m_e^* c^2} \left(\frac{2k_F}{k_{TF}} \right)^3 J(x_r, y), \quad (3.16)$$

where $y = \sqrt{3}T_{pe}/T$, $T_{pe} = (\hbar/k_B)\sqrt{4\pi e^3 n_e/m_e^*}$ is the electron plasma temperature, and

$$J(x_r, y) \approx \left(1 + \frac{6}{5x_r^2} + \frac{2}{5x_r^4} \right) \left[\frac{y^3}{3(1 + 0.07414y)^3} \ln \left(1 + \frac{2.81}{y} - \frac{0.81}{y} \frac{v_F^2}{c^2} \right) + \frac{\pi^5}{6} \frac{y^4}{(13.91 + y)^4} \right] \quad (3.17)$$

is a fit of the scattering integral [170]. This is dependent on the relativistic parameter, $x_r \approx 1.009(\rho_6 Z/A)^{1/3}$, and y . Further, k_F is the Fermi wavevector, v_F is the Fermi velocity, and the electron degeneracy temperature is

$$T_F = \frac{\epsilon_F - m_e c^2}{k_B} \approx 5.93 \times 10^9 \sqrt{1 + x_r^2} \text{ K}. \quad (3.18)$$

In addition, the Thomas-Fermi wavevector describes the electrostatic screening properties of the electron gas by accounting for the change in the electron wavefunction near the ion, and is given by

$$k_{TF}^2 = 4\pi^2 \frac{\partial n_e}{\partial \mu} \approx \frac{\alpha_f}{\pi} \frac{\sqrt{1 + x_r^2}}{x_r} (2k_F)^2. \quad (3.19)$$

The impurity parameter for neutron star matter is expressed as [81]

$$Q \equiv \frac{1}{n} \sum_i (Z_i - \langle Z \rangle)^2, \quad (3.20)$$

where $\langle Z \rangle = n^{-1} \sum_i n_i Z_i$ is the mean charge number. The crust is actually predicted

to be quite impure [129, 130]; however, in this study, only one ionic species is assumed to be present at a given depth. In this manner, impurities can be neglected in order to study the bounds on the conductivity. For the case of no impurities where $Q = 0$, the upper bound on the conductivity is expressed as the electron-phonon scattering off of a pure crystal. The lower bound on the conductivity is that of a completely disordered crust, where $Q \sim Z^2$. This case corresponds to electron-ion interactions in a liquid.

The fits of electron-ion scattering frequency used here were by calculated by Potekhin et al. [119]. The frequency is expressed as

$$\nu_{\text{ei,ep}} = \frac{4Z\epsilon_{\text{F}}}{3\pi\hbar} \alpha_f^2 \Lambda, \quad (3.21)$$

where Λ is the Coulomb logarithm in the Born approximation:

$$\Lambda = \int_{q_0}^{2k_{\text{F}}} dq q^3 u^2(q) S(q) \left[1 - \frac{v_{\text{F}}^2}{c^2} \left(\frac{q}{2k_{\text{F}}} \right)^2 \right]. \quad (3.22)$$

Here, q is the momentum transfer in the collision, and q_0 is a cutoff parameter which is equal to zero for elastic scatterings in the liquid phase, and equal to the equivalent radius of the Brillouin zone, $q_{\text{B}} = (6\pi^2 n_{\text{i}})^{1/3}$, in the solid phase. Expressed in such a manner, Equation (3.21) calculates both the electron-ion and electron-phonon collision frequencies. Equation (3.22) also includes $u(q) \equiv |U(q)|/(4\pi Z e^2)$, where $U(q)$ is the Fourier transform of the electron-ion scattering potential, and $S(q)$, which is the effective static structure factor taking into account correlations in the Born approximation. Potekhin et al. [119] calculate an effective electron-ion scattering potential in order to analytically integrate Equation (3.22), and they provide analytical fits which have been used in this calculation.

Neutrino emission

Neutrino emission in the crust, ε_ν in Equation (3.5), is dominated by bremsstrahlung interactions by electrons scattering off of the Coulomb field of nuclei in the crust [65, 80, 100]:

$$e^- + Z \rightarrow e^- + Z + \nu + \bar{\nu}. \quad (3.23)$$

The fits of Haensel et al. [65] were used for the liquid state of the ions, and those of Yakovlev & Kaminker [168] were used for the crystalline state. Pair, plasma, and photo neutrino emission processes [132] were not included since they are negligible at the temperatures of interest. Pethick & Thorsson [115] showed that band-structure effects would suppress bremsstrahlung interactions at temperatures of 5×10^9 K and below because the separation between electron energy bands is ~ 1 MeV, much larger than the thermal energy. Despite this, these effects have not been included here since the exact structure of the crystal lattice is unknown and the band-gap effects are negligible when the lattice is impure. Furthermore, the neutrino emission in the crust is much lower than the emission from the core and thus the band-gap effects would only minimally affect the neutron star cooling.

Neutrino emission from the core is a very effective means of cooling the neutron star [11, 35, 49, 51]. The standard mode of neutrino energy loss is assumed to be through the modified Urca reactions:

$$n + n \rightarrow n + p + e^- + \bar{\nu}_e \quad (3.24)$$

$$n + p + e^- \rightarrow n + n + \nu_e. \quad (3.25)$$

The neutrino emissivity due to these reactions is [169]

$$L_\nu^{\text{Urca,n}} = 8.55 \times 10^{21} R_{sf}^{Mn} T_9^8 \quad (3.26)$$

for the neutron branch, where T_9 is the temperature in units of 10^9 K. For the proton branch, the emissivity becomes

$$L_\nu^{\text{Urca,p}} = 8.53 \times 10^{21} R_{sf}^{Mp} T_9^8. \quad (3.27)$$

R_{sf}^{Mn} and R_{sf}^{Mp} are again the superfluid reduction factors as given by Levenfish et al. [169].

Because the matter in the neutron star core is unknown, the possibility exists for there to be enhanced neutrino cooling. Enhanced cooling may be due to the presence of a pion condensate [11], quark- β decay [25,82], or direct Urca reactions. As an upper bound on the neutrino luminosity, the direct Urca processes were considered. These are reactions occurring directly, without the need for a spectator nucleon:

$$n \rightarrow p + e^- + \bar{\nu}_e \quad (3.28)$$

$$p + e^- \rightarrow n + \nu_e. \quad (3.29)$$

This process is forbidden in the outer core and crust of the neutron star because the free proton fraction is too low to simultaneously conserve momentum and energy [92]. However, in the inner core the fraction of protons may become high enough that the reactions become relevant. The neutrino emissivity for these reactions is [169]

$$Q = 4 \times 10^{27} R_{sf}^D T_9^6, \quad (3.30)$$

where R_{sf}^D is the reduction factor for the direct Urca process [169]. For temperatures on the order of 10^9 K, the direct Urca process is 5 – 6 orders of magnitude more efficient than the modified Urca process. For a $1.4 M_\odot$ star, as studied here, only the very central region of the core exhibits the direct Urca process if it occurs at all. The spatial separation of the core into direct Urca and modified Urca neutrino emission

regions is discussed in Appendix B.

Nuclear reactions

Heating in the deep crust occurs through electron captures accompanied by neutron emission and pycnonuclear reactions. These were tabulated by Haensel & Zdunik [66] assuming the outermost layer of the crust was composed purely of iron. A later calculation [67] was made of nuclei with $A \sim 106$, but it was shown that there was little difference in total nuclear heating between the two cases. It may be more realistic to consider nuclei such as $A \sim 62, 66$, being products of superbursts [127], but for the current calculation $A = 56$ is sufficient. It is uncertain how the presence of other isotopes in a layer affects the pycnonuclear reactions. The pycnonuclear reactions rely on the inter-particle spacing, and if there are other isotopes present, it is possible that the inter-particle spacing between like species will become larger and pycnonuclear reactions will be quenched; thus, the total energy production for pycnonuclear reactions may be reduced.

Figure 3.4 shows a calculation of the composition and energy production in the crust based on data from [66]. Note that free neutrons are present where $\rho > 6 \times 10^{11}$ g cm⁻³. For each electron capture below the neutron drip density, the mass number remains the same while the charge number decreases by one unit. Above neutron drip, neutrons are emitted during an electron capture and so the mass number drops as well. For a pycnonuclear reaction both the charge number and mass number double.

The plot of energy production clearly shows that most of the energy produced in the crust is due to pycnonuclear reactions; however, the energy produced by the electron captures may be more evident in certain observations as discussed below. Table 3.2 lists the reactions in the neutron star crust for the $A = 56$ chain. According to Haensel & Zdunik [66], reactions deeper in the crust ($\rho > 10^{13}$ g cm⁻³) are not included here because the energy release per nucleon beyond this point is negligible

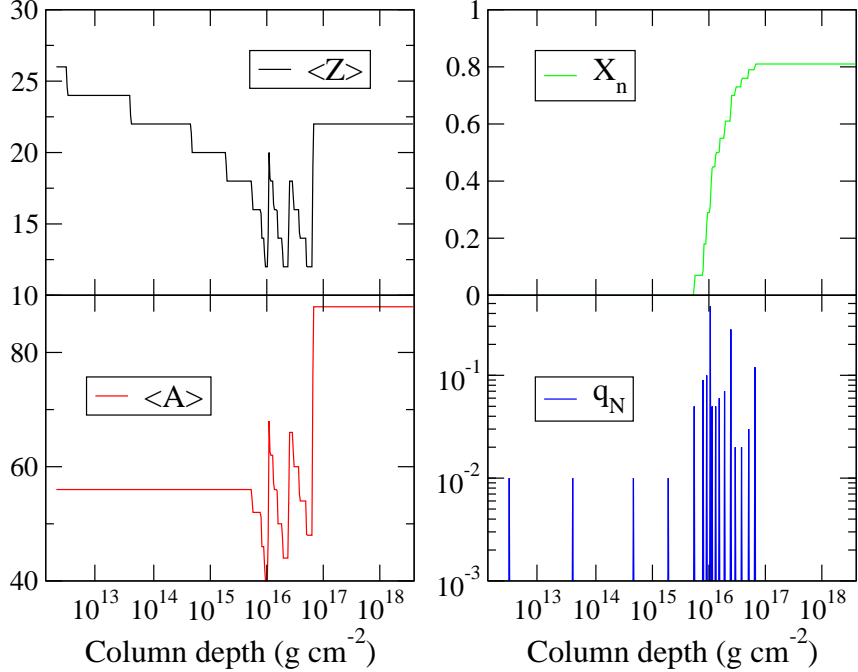


Figure 3.4: A calculation of the crust composition using data from Haensel & Zdunik [66]. In the plots of $\langle Z \rangle$ and $\langle A \rangle$ the steps down are due to electron captures and the jumps up are due to pycnonuclear reactions. X_n is the neutron mass fraction and q_N is the nuclear energy production in units of MeV/u.

compared to reactions at lower pressures. The neutron fraction also becomes large enough that there are more free neutrons than neutrons in nuclei; therefore, the nuclei become less dense and less bound. In addition, the validity of the model they use becomes questionable at densities greater than $10^{14} \text{ g cm}^{-3}$ since the free neutron fraction becomes so high that only about 10% of nucleons are bound in nuclei.

Jones [83] has recently reviewed the evolution of rp-process ashes beyond neutron drip and has shown that the electron capture calculations of Haensel & Zdunik [66] produce nuclei lying well below the equilibrium charge number for matter at this density. He states that further reactions must proceed to increase Z . Principally, these reactions are neutron pair captures followed by electron emission. As a result, he predicts the mass-quadrupole tensor components to be an order of magnitude smaller than previous estimates [17, 150], which would have observational consequences for gravitational wave emission. While confirmation of this theory and implementation

Table 3.2: Reactions occurring in the neutron star crust as a function of pressure [66]. The heat deposited by each reaction is also listed. The first group of reactions occur in the outer crust before neutron drip. The rest of the reactions occur in the inner crust.

Pressure (dyne cm ⁻²)	Reaction	Heat deposited (MeV/u)
7.235×10^{26}	$^{56}\text{Fe} \rightarrow ^{56}\text{Cr} - 2e^- + 2\nu_e$	0.01
9.569×10^{27}	$^{56}\text{Cr} \rightarrow ^{56}\text{Ti} - 2e^- + 2\nu_e$	0.01
1.152×10^{29}	$^{56}\text{Ti} \rightarrow ^{56}\text{Ca} - 2e^- + 2\nu_e$	0.01
4.747×10^{29}	$^{56}\text{Ca} \rightarrow ^{56}\text{Ar} - 2e^- + 2\nu_e$	0.01
1.361×10^{30}	$^{56}\text{Ar} \rightarrow ^{52}\text{S} + 4n - 2e^- + 2\nu_e$	0.05
1.980×10^{30}	$^{52}\text{S} \rightarrow ^{46}\text{Si} + 6n - 2e^- + 2\nu_e$	0.09
2.253×10^{30}	$^{46}\text{Si} \rightarrow ^{40}\text{Mg} + 6n - 2e^- + 2\nu_e$	0.10
2.637×10^{30}	$^{40}\text{Mg} \rightarrow ^{34}\text{Ne} + 6n - 2e^- + 2\nu_e$ $^{34}\text{Ne} + ^{34}\text{Ne} \rightarrow ^{68}\text{Ca}$	0.47
2.771×10^{30}	$^{68}\text{Ca} \rightarrow ^{62}\text{Ar} + 6n - 2e^- + 2\nu_e$	0.05
3.216×10^{30}	$^{62}\text{Ar} \rightarrow ^{56}\text{S} + 6n - 2e^- + 2\nu_e$	0.05
3.825×10^{30}	$^{56}\text{S} \rightarrow ^{50}\text{Si} + 6n - 2e^- + 2\nu_e$	0.06
4.699×10^{30}	$^{50}\text{Si} \rightarrow ^{44}\text{Mg} + 6n - 2e^- + 2\nu_e$	0.07
6.043×10^{30}	$^{44}\text{Mg} \rightarrow ^{36}\text{Ne} + 8n - 2e^- + 2\nu_e$ $^{36}\text{Ne} + ^{36}\text{Ne} \rightarrow ^{72}\text{Ca}$ $^{72}\text{Ca} \rightarrow ^{66}\text{Ar} + 6n - 2e^- + 2\nu_e$	0.28
7.233×10^{30}	$^{66}\text{Ar} \rightarrow ^{60}\text{S} + 6n - 2e^- + 2\nu_e$	0.02
9.238×10^{30}	$^{60}\text{S} \rightarrow ^{54}\text{Si} + 6n - 2e^- + 2\nu_e$	0.02
1.228×10^{31}	$^{54}\text{Si} \rightarrow ^{48}\text{Mg} + 6n - 2e^- + 2\nu_e$	0.03
1.602×10^{31}	$^{48}\text{Mg} + ^{48}\text{Mg} \rightarrow ^{96}\text{Cr}$	0.11
1.613×10^{31}	$^{96}\text{Cr} \rightarrow ^{88}\text{Ti} + 8n - 2e^- + 2\nu_e$	0.01

into the cooling calculations are beyond the scope of this work, a future study will be devoted to this problem.

3.1.3 Numerical method

Recasting Equation 3.5 in a solvable form gives

$$\frac{\partial T}{\partial t} = \frac{1}{c_P \rho} \left[\frac{\partial K}{\partial r} \frac{\partial T}{\partial r} + \frac{2K}{r} \frac{\partial T}{\partial r} + K \left(\frac{\partial^2 T}{\partial r^2} \right) \right] + \frac{1}{c_P} \varepsilon. \quad (3.31)$$

Using the scale height, $H = P/\rho g$, and hydrostatic balance, $dP/dr = -\rho g$, Equation (3.31) was solved as a function of $\ln P$ using $dr = H d \ln P$ to ensure that there would be adequate resolution where the pressure and density change rapidly as a function of radius.

Equation (3.31) is a parabolic nonlinear differential equation which was linearized into a series of ordinary differential equations (ODE) using the method of lines [97, 135]. Following this formulation, each $\partial/\partial \ln P$ term can be translated into a finite difference between the two points adjacent to the point of interest in a second order method. Since the boundary conditions are dependent only on the point of interest and one adjacent point, inaccuracies in the boundary conditions will propagate through neighboring points in the calculational grid. These errors will be smoothed out with subsequent integration steps. The series of ODEs was integrated forward in time using the variable-order Bader-Deuffhard stiff integration routines [9] with a tolerance of 10^{-3} . A convergence test was made that showed the calculational method deviated only slightly when the number of grid points, N , was changed. $N = 400$ was chosen to keep the computation time short while giving enough spatial resolution to ensure that at most two electron capture layers would fall within a zone. With this resolution, the thermal time at the top of the crust (Equation [3.6]) is ~ 1 day.

A *zone* is defined as the difference in the log of the pressure: $\Delta(\ln P)$. The vari-

ous calculational quantities, such as temperature and density, are determined at the boundaries of the zone. It is assumed that matter does not accumulate anywhere so $\partial\rho/\partial t = 0$, and the grid is static. The composition of a zone containing a burning layer is the mass average of nuclei present above and below the layer. Zones not containing a burning layer are composed of a single ionic species. Each burning layer is included in only one zone determined by the pressure at which the burning occurs, and the heating is spread out over the zone. If there is more than one burning layer in a pressure zone, the deposited heat is the sum of the heat for each layer and the composition of the zone is the mass average of the composition above, below, and between the burning layers.

Boundary conditions

Because each boundary point is adjacent to only one other grid point, the corresponding partial differential equations must be amended. For the outer boundary, the equation becomes

$$\frac{\partial T}{\partial t} = -\frac{1}{c_P \rho} \frac{1}{H \Delta(\ln P)} [F_0 - F_n], \quad (3.32)$$

where F_0 is the flux at the stellar surface, and F_n is the flux at a density of 10^9 g cm^{-3} , the top of the crust.

The value of F_0 is dependent on the composition and thermonuclear state of the upper layers. During accretion, the temperature at the base of the hydrogen burning zone is set to $T_0 = 2.5 \times 10^8 \text{ K}$ [23, 43]. Equating the flux at this point to the flux at the outer boundary of the crust yields

$$\frac{F}{10^{22}} = \frac{1}{1.2} \left[\ln \left(\frac{y}{y_0} \right) \right]^{-1} \left[\left(\frac{T}{T_0} \right)^2 - 1 \right], \quad (3.33)$$

with the base of the hydrogen burning zone set at $y_0 = 10^8 \text{ g cm}^{-2}$. See Appendix A for the derivation of this boundary condition.

In the absence of accretion, the upper boundary condition is set by the material in the envelope surrounding the crust [64]. It is assumed that this envelope is composed of ^{56}Fe , though a small amount of accreted material ($M \gtrsim 10^{-16} M_\odot$) will affect the cooling rate since the thermal insulation will be reduced due to the lighter nuclei present [118]. The temperature fits calculated by Potekhin et al. [118] match an effective temperature at the stellar surface to a temperature in the deeper layers at a density of $10^{10} \text{ g cm}^{-3}$. This relationship is determined by the equation of state and the thermal conductivity of the matter in the envelope, both of which are affected by the composition. From this relationship a flux can be calculated at the surface and equated to the flux at the outer boundary. The temperature relationship is given by

$$T_b = 1.288 \times 10^8 \left(\frac{T_{6,s}^4}{g_{14}} \right)^{0.455} \text{ K}, \quad (3.34)$$

where $T_{6,s}$ is the effective temperature in units of 10^6 K , and g_{14} is the gravity at the outer boundary in units of $10^{14} \text{ cm s}^{-2}$.

The core is assumed to be isothermal due to its high conductivity [62] and so the inner boundary is placed at the edge of the outer core at a density of $1.6 \times 10^{14} \text{ g cm}^{-3}$. The boundary condition at this point is given by

$$\frac{\partial T}{\partial t} = \frac{4\pi r_{cc}^2}{C} K \frac{\partial T}{\partial r} - \frac{1}{C} L_\nu, \quad (3.35)$$

where r_{cc} is the radius of the core-crust interface, and C is the total heat capacity of the core. L_ν is the neutrino luminosity of the core, which, in this calculation, may be given by either modified Urca neutrino emission (Equations [3.26] and [3.27]), or direct Urca neutrino emission (Equation [3.30]). See Appendix B for details on the total heat capacity of the core and the treatment of the neutrino luminosity in the presence of nucleon superfluidity.

Accretion events

An *outburst* is defined as the period of time during which the neutron star exhibits a high luminosity, which can range from about $10^{36} - 10^{38}$ erg s⁻¹. In these calculations it is assumed that this luminosity is due to accretion. Outbursts are separated by *quiescent periods* when the neutron star emits a lower luminosity between $10^{32} - 10^{34}$ erg s⁻¹, during which it is assumed that the accretion has shut off. Over the course of many outbursts, where the recurrence time $\tau_{rec} < 10^4$ yr, the neutron star crust will reach a limit cycle such that the temperature profile of the crust and core return to the same quiescent level after each outburst. A recurrence time greater than this corresponds to the thermal timescale of the core, at which point the thermal emission is no longer dominated by heat from the crust.

To obtain a reproducible cooling curve, such as what a neutron star would exhibit after millions of years, a model was run starting from a temperature profile corresponding to a $1.4 M_{\odot}$, 10.7 km neutron star with electron-ion scattering in the crust (see Figure 7 of Brown [23]). The initial temperature profile is consequential only in the number of outbursts needed to reach a limit cycle. Over the course of many outbursts, the crust relaxes into its own characteristic temperature profile regardless of the choice of the initial profile. Once a limit cycle was reached, one further calculation was done for a time spanning the outburst and the following quiescent period starting with the temperature profile at the end of the previous quiescent period. Each cooling curve described herein has been calculated in this manner.

The mass accretion rate enters into the calculation through the nuclear energy term, ε_N , in Equation (3.5). For simplicity, each accretion event is represented by the sum of two step functions since the precise behaviour of the accretion as it turns on and off is uncertain. One should note that there may be residual accretion after the end of the outburst and so the calculations presented here offer a lower limit to the quiescent luminosity curves. The timestep for each integration period was chosen

to be less than 1% of the length of the outburst. Timesteps greater than this were shown to reduce the resultant luminosity, and shorter timesteps had a negligible effect on the luminosity. Furthermore, this timestep allows the calculation to be run in a reasonable amount of time.

3.2 The transient neutron star KS 1731-260

3.2.1 Observations of the source

Having been initially detected in 1989 by COMIS/TTM on *Mir-Kvant* [141], the neutron star X-ray transient KS 1731-260 accreted actively for ~ 12 yr and entered quiescence in February 2001. A possible optical counterpart was identified using *Chandra* [160], and infrared counterparts were found with YALO [111], and ESO/MPI [101]. The detection of type I X-ray bursts characterizes the primary as a neutron star. Subsequent observations about one month after the source entered quiescence [24, 159] showed that the luminosity of the source rapidly decreased from $\sim 10^{37}$ erg s $^{-1}$ to $\sim 10^{33}$ erg s $^{-1}$, though this may be uncertain to within a factor of three due to spectral errors [124]. The source was observed again by Wijnands et al. [158] using *XMM-Newton* in September 2001, and it was found that the X-ray luminosity had dropped to $(2 - 5) \times 10^{32}$ erg s $^{-1}$.

Analysis of radius-expansion bursts by Munro et al. [103] set an upper limit on the distance to the source of 7 kpc. This method was discussed by Galloway et al. [57]. If the energy of a thermonuclear burst is released rapidly enough, the maximum luminosity, the Eddington luminosity (Equation [2.1]), will be reached when the radiation force balances gravity. The extra energy is converted to potential and kinetic energy which raises the outer layers of the star while the luminosity remains constant. The apparent temperature and the solid angle of the emission region are obtained from blackbody fits to the background-subtracted burst spectra. The source is not likely

a pure blackbody since electron scattering can cause deviations in the spectra. This results in a higher temperature and a smaller radius at a given flux.

Rutledge et al. [124] assumed an outburst duration $\tau_{ob} = 13$ yr and calculated a recurrence time $\tau_{rec} = 1500$ yr from the flux to match the value inferred by assuming a steady-state crust. The quiescent flux for the source is the lowest observed flux thus far, $F_q = 3.5 \times 10^{-13}$ erg cm⁻² s⁻¹. Integrating over the length of the outburst, they found a fluence of $\mathcal{F} = 2.3$ erg cm⁻². The recurrence time is given by [124]

$$\tau_{rec} \approx \frac{\mathcal{F}}{135 F_q} \frac{Q_{nuc}}{1.45 \text{ MeV}} \frac{0.2}{\epsilon}, \quad (3.36)$$

where Q_{nuc} is the nuclear energy deposited in the crust and ϵ is the efficiency with which the accretion energy is converted to radiation. Rutledge et al. [124] made theoretical calculations of this source using the 1500 yr recurrence time calculated for a steady-state crust and compared the lightcurves to their quiescent observation. They showed that this observation was best explained by assuming a high-conductivity crust and enhanced neutrino cooling in the core. In addition, to agree with their observation of $L_q = 2.7 \times 10^{33}$ erg s⁻¹, the total energy from nuclear heating in the crust needed be adjusted to $Q_{nuc} = 3.1$ MeV, more than twice the value predicted by Haensel & Zdunik [66] for the $A = 56$ electron capture chain.

During its period in outburst, one 12 hr superburst was observed in 1996 with *RXTE*/ASM [86]. If the ignition of ¹²C is the source of these outbursts, then at some point during outburst, KS 1731-260 must have reached a temperature high enough to ignite ¹²C unstably at a depth where the recurrence time would be ~ 12 yr. This places an additional constraint in matching calculations to the observations. The calculations presented here were made to compare with the results of Rutledge et al. [124] and to expand upon their work by surveying a range of recurrence times and possible outburst lengths. Self-consistent calculations are also made to study the

Table 3.3: The four physical models used in the cooling calculations.

	Low conductivity electron-ion	High conductivity electron-phonon
Standard cooling modified Urca	ei,std	ep,std
Enhanced cooling direct Urca	ei,enh	ep,enh

feasibility of unstable ignition of ^{12}C .

3.2.2 Modeling the source

For comparison to the work of Rutledge et al. [124], the cooling code input was set to match the inferred properties of KS 1731-260: $\tau_{ob} = 12$ yr, and $\tau_{rec} = 1500$ yr. The accretion rate was calculated from the observed luminosity during outburst from [22],

$$L_{acc} \approx \frac{GM\dot{M}}{R} = 1.858 \times 10^{38} \left(\frac{M}{1.4 M_{\odot}} \right) \left(\frac{10 \text{ km}}{R} \right) \left(\frac{\dot{M}_{ob}}{10^{18} \text{ g s}^{-1}} \right) \text{ erg s}^{-1}, \quad (3.37)$$

where \dot{M}_{ob} is the mass accretion rate during the outburst. For KS 1731-260 this results in $\dot{M}_{ob} = 2 \times 10^{17} \text{ g s}^{-1}$, though this value may be quite uncertain due to errors in the distance, accretion efficiency, and physical uncertainties of the binary system. The model was run with both high and low conductivity, and both standard and enhanced core neutrino cooling (Table 3.3). Rutledge et al. [124] state that the maximum core temperature of this source should be $< 3.5 \times 10^8 \text{ K}$, and these calculations confirm that.

The resulting cooling curves are shown in Figure 3.5, and are in good agreement with the calculations of Rutledge et al. [124], though there are some differences. The left panel shows the luminosity of the star as a function of time after the outburst has ended, and can be compared with Figure 3 of Rutledge et al. [124]. Note that their figure shows the quiescent luminosity at infinity (Equation [2.3]) and the quiescent luminosity shown in Figure 3.5 is the luminosity at the surface of the star. The

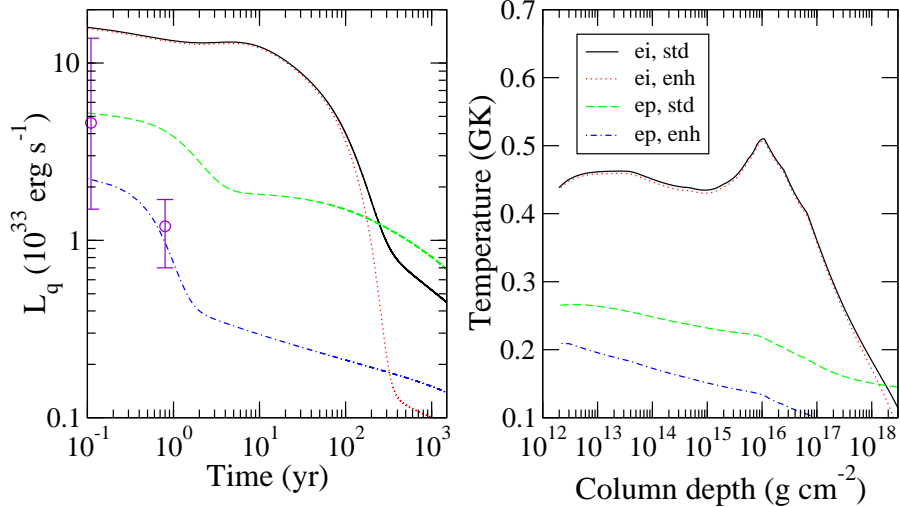


Figure 3.5: Calculation of KS 1731-260 for $\tau_{ob} = 12$ yr and $\tau_{rec} = 1500$ yr, showing the cooling curves (left panel) and maximum temperature profiles (right panel). The observations are marked with circles.

microphysics used in this calculation is the same as in Rutledge et al. [124, 151], though the exact implementation and treatment of the core physics may differ. One difference in the model is that they assumed $\tau_{ob} = 13$ yr while $\tau_{ob} = 12$ yr is assumed here, though this difference should have a negligible effect on the quiescent luminosity. It is not understood why their curve for the high-conductivity/standard cooling case is so close to the curve for the low-conductivity cases, since a high-conductivity crust means that the heat leaves the star much faster than a low-conductivity crust, thus resulting in a lower luminosity.

The observations are also shown in Figure 3.5. The point at $t = 0.1$ yr is the *Chandra* observation by Rutledge et al. [124] and has been adjusted to the stellar reference frame. The large error bar is mostly due to spectral uncertainty. The point at $t = 0.7$ yr is an *XMM-Newton* observation made by Wijnands et al. [158]. The value they quote has been adjusted to the stellar reference frame also, and since they quote only the X-ray luminosity, their value was doubled to approximate the bolometric luminosity. In order to fit the observation of $L_q = 4.6 \times 10^{33}$ erg s $^{-1}$ at $t = 0.1$ yr and $L_q = 1.2 \times 10^{33}$ erg s $^{-1}$ at $t = 0.7$ yr, both high conductivity and

enhanced core neutrino cooling are needed in the star, as has been suggested by Rutledge et al. [124] and as illustrated in Figure 3.5. Moreover, the slope of the high-conductivity/enhanced cooling case is the best match to the data. This is probably a better comparison parameter since this ratio is not dependent on the distance to the source.

Figure 2.4 shows the observed lightcurve of KS 1731-260. The drop in flux takes ~ 4 yr from a maximum at MJD 500 to the lowest observed flux at MJD 2000, hinting that the mass accretion rate may decrease during that time. A calculation of KS 1731-260 was made in which the mass accretion rate decreased steadily during the last 4 yr of the outburst, and the results are shown in Figure 3.6. Comparing Figures 3.6 and 3.5 shows that while there is only a slight change for the low-conductivity cases, the cooling curves are much flatter for a steadily decreasing mass accretion rate. In addition, the slope of the high-conductivity/enhanced cooling case for the variable mass accretion rate during outburst does not match the observations as well as the same model for a constant mass accretion rate, hinting at continued accretion until the end of the outburst. Furthermore, the error bar is large enough on the $t = 0.1$ yr observation that the low-conductivity cases are not ruled out. While a more in-depth study of this problem has not been undertaken, this calculation indicates that such an investigation is necessary.

Figure 3.5 also shows temperature profiles of the crust at the time when the temperature is at a maximum. This maximum temperature profile is reached at the end of an outburst. If this source is to produce superbursts, the temperature at a column depth of 10^{12} g cm $^{-2}$ must reach a temperature high enough to ignite ^{12}C unstably in the upper layers of the star. Brown [20] studied the ignition depth of ^{12}C in the steady-state crust and showed that enhanced cooling is not compatible with the observed superburst energetics and recurrence times unless the crust has a low conductivity.

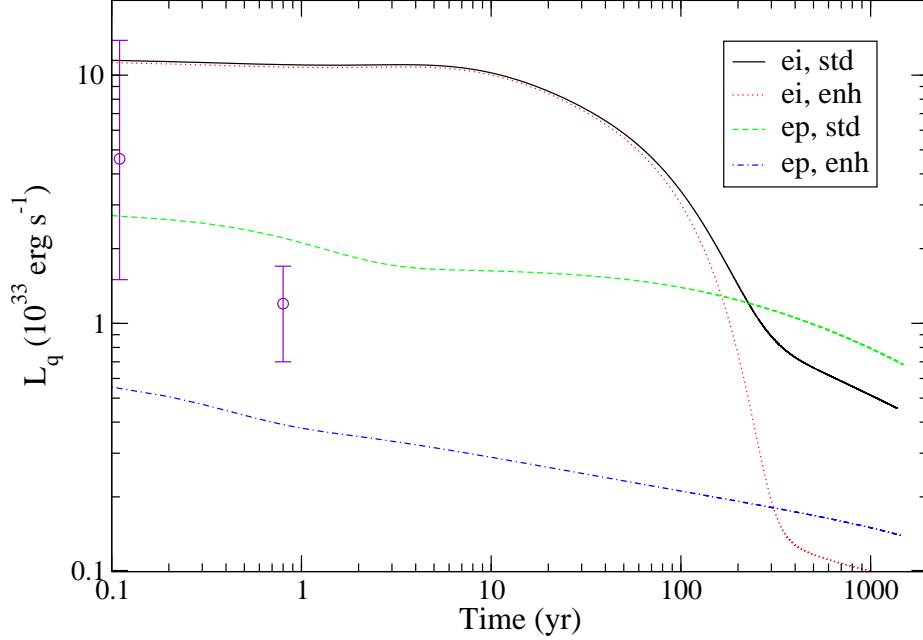


Figure 3.6: Calculation of KS 1731-260 for $\tau_{ob} = 12$ yr and $\tau_{rec} = 1500$ yr where the mass accretion rate decreased steadily for the last 4 yr of the outburst. The observations are marked with circles.

Clearly the calculations of KS 1731-260, which exhibited a superburst, indicate both a high-conductivity crust and enhanced neutrino cooling. Here, self-consistent ^{12}C ignition calculations were made following Cumming & Bildsten [44] and Brown & Bildsten [21] to determine the recurrence time of unstable ^{12}C burning given the properties of KS 1731-260. The ignition condition is expressed as

$$\frac{d\varepsilon_{nuc}}{dT} \geq \frac{d\varepsilon_{cool}}{dT}, \quad (3.38)$$

where ε_{nuc} is given by

$$\varepsilon_{nuc} = \frac{1}{2} Q Y_C^2 \rho N_A^2 \langle \sigma v \rangle E, \quad (3.39)$$

and ε_{cool} is given by the approximation

$$\varepsilon_{cool} = \frac{\rho K T}{y^2}. \quad (3.40)$$

Table 3.4: Neutron star crust properties and ^{12}C ignition properties for various cooling models. The temperature T is at the outer boundary, y is the column depth at which ^{12}C would ignite, Γ indicates the state of matter at y , and t_{rec} is the recurrence timescale for ignition.

Model	T (10^8 K)	y (10^{12} g cm^{-2})	Γ	t_{rec} (yr)
ei, std	4.38	9.44	35.7	20
ei, enh	4.36	9.44	36.0	20
ep, std	2.65	33.7	88.3	71
ep, enh	2.10	45.1	2705	95

Here, $Q = 13.96$ MeV is the Q -value of the $^{12}\text{C} + ^{12}\text{C} \rightarrow ^{24}\text{Mg}$ fusion reaction, $N_A \langle \sigma v \rangle$ is the stellar reaction rate, and E is the enhancement factor. A 10% mass fraction of ^{12}C throughout the crust and a 90% mass fraction of the species present at a given depth were assumed. The $^{12}\text{C} + ^{12}\text{C}$ reaction rate of Caughlan & Fowler [30] was used with the screening enhancement factor of Ogata et al. [108]. Table 3.4 shows the results of this calculation along with properties of the neutron star crust for the various cooling models shown in Figure 3.5. The temperature at the outer boundary of the crust is the major determinant in where ^{12}C will ignite in the star.

Since the burst profile, cooling behavior, and energetics of the KS 1731-260 superburst are similar to other superbursts, the recurrence time should also be similar. Kuulkers et al. [86] found an energy of $\simeq 9.8 \times 10^{41}$ erg for the superburst from KS 1731-260, indicating a recurrence time of 5.5 yr assuming the presence of 10% ^{12}C . Considering that the 12 yr, non-continuous observation of this source yielded evidence of one superburst, there are few constraints for the recurrence time that one can place on this source resulting from the calculations presented here. This calculation assumes that ^{12}C survives to the ignition depth; however, several caveats should be mentioned. First, it is not at all certain that ^{12}C even survives to the ignition depth listed in Table 3.4. In the region between the base of the rp-process burning zone and the top of the electron capture zone, reactions with residual ^4He could deplete the amount of ^{12}C . In addition, for the first three models listed in Table 3.4, stable burning depletes

the ^{12}C before unstable burning can ignite. Another problem is that Γ (Equation [3.7]) for the high-conductivity/enhanced cooling scenario is well into the regime of a crystalline state at the ignition depth. In this case, it is likely that the ^{12}C nuclei are well-separated from each other and interspersed with other nuclei such that carbon fusion reactions would be suppressed. In recent work, Cooper & Narayan [40] studied the neutron star parameters in relation to ^{12}C ignition and found that superbursts on neutron stars with high-conductivity crusts and enhanced neutrino cooling were much too energetic ($> 10^{44}$ erg) to match the observations. Nevertheless, superbursts are observed and deep ignition of ^{12}C is currently the most likely explanation.

Dependence on outburst length and recurrence time

To understand how KS 1731-260 can show both superbursts and a low luminosity after one year in quiescence, calculations were run for a series of outburst lengths ranging from 3 – 12 yr and recurrence times ranging from 100 – 1500 yr. While an outburst length of 12 yr is the estimated value for this source, continuous monitoring of the source was done only for the last 6 yr of the outburst period, placing a lower limit on the outburst length. All the same, an outburst length of 3 yr is included for comparison. Since the source has only been observed in one outburst period, the recurrence time is unconstrained, so several recurrence times are also tested. Rutledge et al. [124] claim that the recurrence timescale found by Wijnands et al. [159] is a lower limit, though it will be shown in a parameter study (Section 3.4) that the recurrence timescale for KS 1731-260 is unconstrained even at short recurrence times. The low-conductivity/standard cooling model is discussed here, though general trends in the results hold for the other models.

For an outburst length $\tau_{ob} = 12$ yr, there is little variation in the maximum temperature curves or in the length of the cooling timescale for different recurrence times. This can be understood by considering the thermal state of the crust at the end

of the outburst. For a low-conductivity/standard cooling model, the thermal profile of the crust and core is hot enough that the time it takes for heat to diffuse from the core through the crust (see Figure 3.1) is on the order of the recurrence time, so little variation is seen in the thermal profile for small changes in the length of the recurrence time. The recurrence time affects the quiescent luminosity for times shorter than the thermal diffusion timescale through the crust, which is about 100 yr.

There is more variation in the temperature profiles for an outburst length of $\tau_{ob} = 6$ yr. Figure 3.7 shows the cooling curves and temperature profiles for various recurrence times. It is clear in the plot of cooling curves that the quiescent luminosity for any recurrence time is similar to the low-conductivity/standard cooling model calculated for the $\tau_{ob} = 12$ yr case (compare to Figure 3.5). The change in quiescent luminosity over time is not large, and this behavior would be evident observationally; however, the luminosity difference between cooling curves for the various recurrence lengths is too small to be observed. In addition, it is shown in the plot of temperature profiles that the interior of the star stays slightly cooler for long recurrence times than for the $\tau_{ob} = 12$ yr case, though the temperature at $y \sim 10^{12}$ g cm⁻² is still high enough that ¹²C may be ignited.

Finally, note the temperature inversion around $y \sim 10^{15}$ g cm⁻². Since there is a heat flux into the star from the hydrogen burning in the outer layers and since the heat from the deep crust reactions flows primarily into the core, the outer crust ($y \sim 10^{12} - 10^{14}$ g cm⁻²) heats up more quickly than the region around 10^{15} g cm⁻². This behaviour is even more pronounced when the outburst length is shortened to 3 yr (Figure 3.8). It is clear that the outburst length of KS 1731-260 is not this short, but the calculation may be applicable to other sources where the outburst length is comparable (e.g. MXB 1659-29). This situation may also offer a scenario consistent with the observations of KS 1731-260 whereby the quiescent luminosity of a source can drop significantly in ~ 1 yr while still maintaining a high temperature in the outer

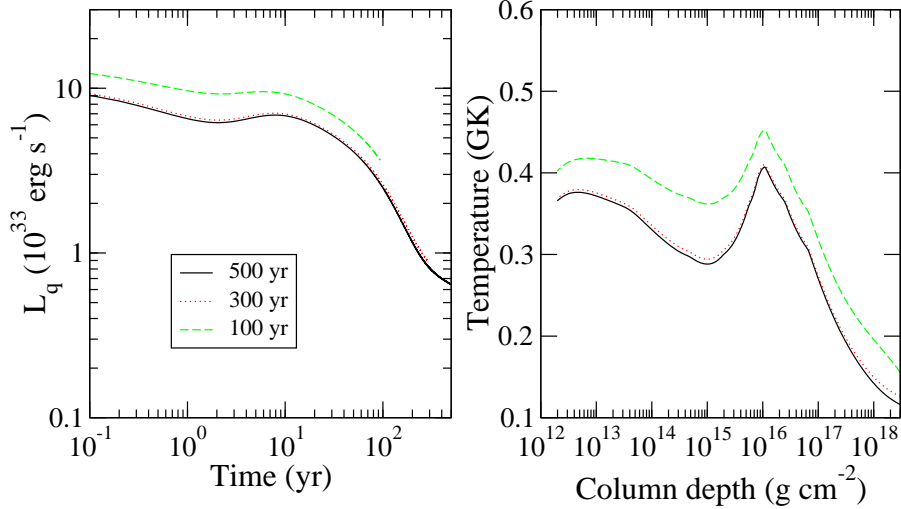


Figure 3.7: Calculation of KS 1731-260 for $\tau_{ob} = 6$ yr and various recurrence times, showing the cooling curves (left panel) and maximum temperature profiles (right panel). Calculations were made for the low-conductivity model with standard cooling.

crust. As is evident in the plot of cooling curves for $\tau_{ob} = 3$ yr, there is a drop in the quiescent luminosity by a factor of two in the first year after the end of the outburst. This points to a prominent role for the electron captures in the outer crust in heating up the outer layers which then cool off more rapidly than the interior (Figure 3.1). The short outburst length means that the crust at a depth of $10^{12} \text{ g cm}^{-2}$ does not heat up enough to trigger ^{12}C ignition in the upper layers, and such systems should therefore show no superbursts. On the other hand, while the temperature profiles for an outburst length of 12 yr begin to plateau around $\rho \sim 10^{15} \text{ g cm}^{-2}$, they do not exhibit an inversion.

The short outburst lengths and recurrence times discussed here search for a scenario whereby the temperature at the top of the crust can be hot enough to ignite ^{12}C while the lightcurve declines rapidly enough to match the observations of KS 1731-260. However, as can be seen, the observed luminosity decline cannot be explained when using realistic recurrence times since the calculated lightcurves are still too flat.

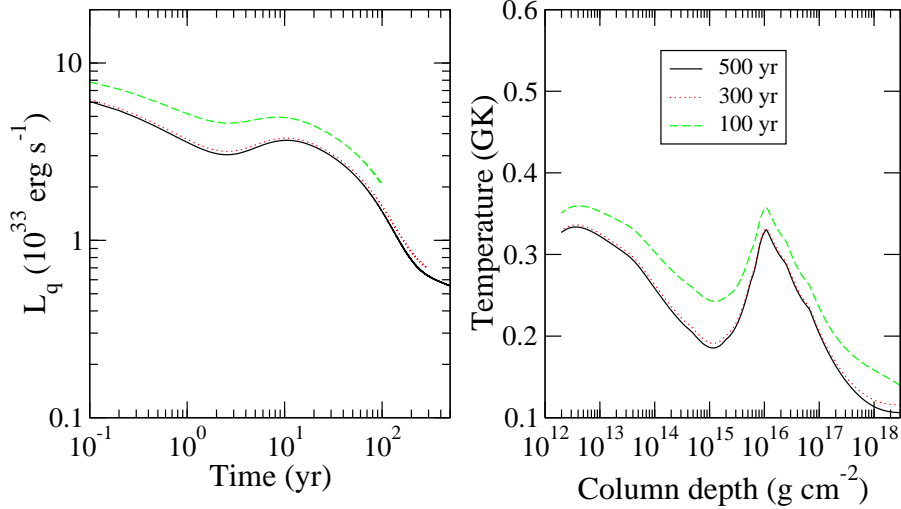


Figure 3.8: Calculation of KS 1731-260 for $\tau_{ob} = 3$ yr and various recurrence times, showing the cooling curves (left panel) and maximum temperature profiles (right panel). Calculations were made for the low-conductivity model with standard cooling.

Dependence on mass accretion rate

Since the mass accretion rate for this source is quite uncertain, calculations were made to study the effect of the mass accretion rate on the cooling curves and temperature profiles. The standard $\tau_{ob} = 12$ yr and $\tau_{rec} = 1500$ yr was used. It has already been shown in Figure 3.5 that the calculation for the high-conductivity/enhanced cooling model yields the proper cooling curve, but the temperature is too low for superburst ignition on a recurrence timescale of 10 yr. On the opposite front, the temperature predicted by the low-conductivity/standard cooling model is consistent with superbursts, but the cooling curve is much too shallow. A nice compromise between the low quiescent luminosity and high temperature profile is the low-conductivity/enhanced cooling case which shall be used here.

Changing the mass accretion rate halfway through the outburst by $\pm 50\%$ did not change the cooling curve by more than a factor of two. However, the mass accretion rate was also varied from $10^{15} - 2 \times 10^{17}$ g s $^{-1}$ for the entire outburst duration, and the results are shown in Figure 3.9. It is evident that there is a large dependence on the mass accretion rate in the amount of heat deposited in the crust. Although the

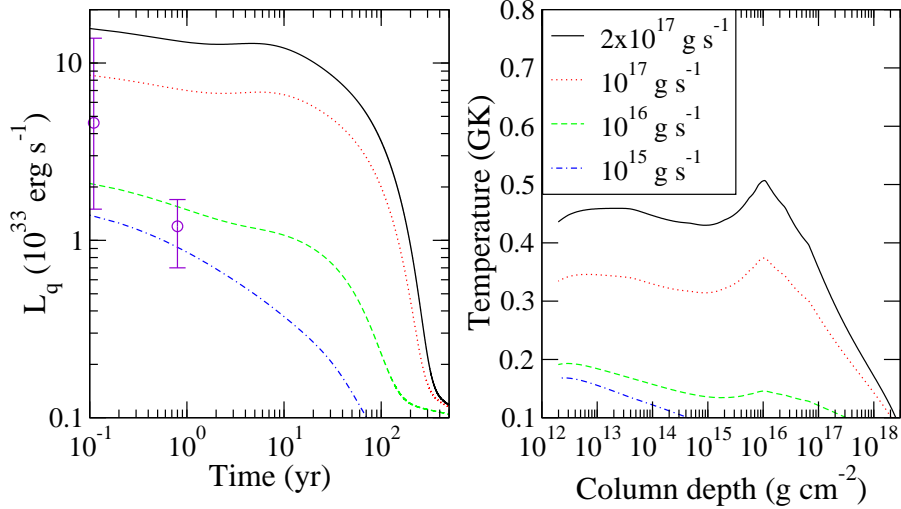


Figure 3.9: Calculation of KS 1731-260 for $\tau_{ob} = 12$ yr, $\tau_{rec} = 1500$ yr, and various outburst mass accretion rates. The cooling curves (left panel) and maximum temperature profiles (right panel) are shown. A low-conductivity/enhanced cooling model is used. The observations are indicated by the circles.

luminosity at $t = 1$ yr matches the observations best for the low accretion rates, the temperature at the ^{12}C ignition layer is much too low to ignite superbursts on a 10 yr recurrence timescale.

During the outburst, the accretion luminosity, L_{acc} , is given by Equation (3.37). Following the outburst period, the crust cools according to whichever model is used, and the quiescent luminosity at $t = 1$ yr, L_{q1} , is useful in distinguishing between these models. The ratio L_{acc}/L_{q1} is independent of the distance to the source and thus is useful in reducing the uncertainties in the observations. If one compares L_{acc}/L_{q1} for different models and mass accretion rates, a rough fit finds that the ratio L_{acc}/L_{q1} goes as $\sim \sqrt{\dot{M}_{ob}}$ (Figure 3.10).

The high-conductivity models have a higher L_{acc}/L_{q1} ratio across all mass accretion rates due to the behavior of the high-conductivity crust. The outburst luminosity is dependent mainly on the mass accretion rate, and thus does not vary with the interior stellar properties. The high-conductivity models cool much more within a year than the low-conductivity models; hence, the ratio L_{acc}/L_{q1} is higher. Note that

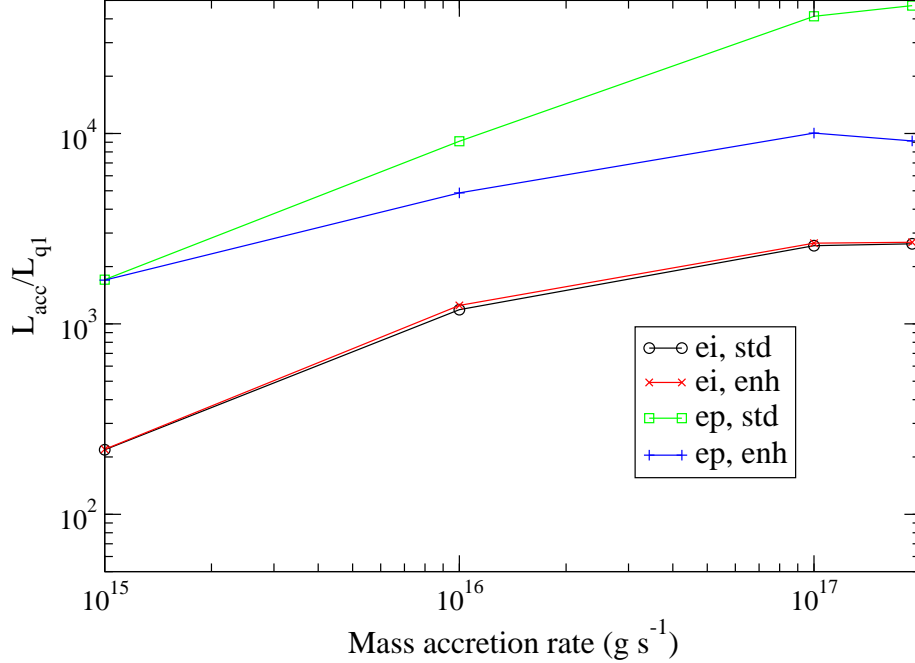


Figure 3.10: The ratio L_{acc}/L_{q1} as a function of mass accretion rate during the outburst for $\tau_{ob} = 12$ yr and $\tau_{rec} = 1500$ yr. L_{q1} is the luminosity 1 yr after the end of the outburst.

L_{acc}/L_{q1} for the high-conductivity/enhanced cooling model at $\dot{M}_{ob} = 2 \times 10^{17} \text{ g s}^{-1}$ is actually lower than L_{acc}/L_{q1} for $\dot{M}_{ob} = 10^{17} \text{ g s}^{-1}$. This is because the lightcurve for the higher mass accretion rate drops more quickly in the first year than the lightcurve for the lower mass accretion rate. The crust is heated more for the higher mass accretion rate and the high conductivity allows the heat to flow out faster. The cooling curve is much less steep for lower mass accretion rates so the effect is not noticeable.

This ratio difference for a given mass accretion rate is dependent solely on the stellar properties. If the outburst and recurrence lengths for a given source are known, the accretion rate may be inferred from a diagram such as Figure 3.10 with assumptions on the interior stellar properties. On the other hand, if the accretion rate of system is known, such a diagram will help to narrow the interior properties of the neutron star. A parameter study and additional diagrams of L_{q1} are discussed in Section 3.4.

3.2.3 Summary

The work presented here shows calculations of KS 1731-260 cooling from an outburst period into quiescence. The presence of a core with $T < 10^8$ K has been confirmed. It has been demonstrated that KS 1731-260 most likely contains a high-conductivity crust and exhibits enhanced neutrino cooling from the core. The calculations made here agree with the observations within the uncertainties. Despite this, the temperature of the outer crust for this model is too low to ignite ^{12}C as fuel for superbursts. Calculations based on the energy of the observed superburst indicate a recurrence time of 5.5 yr, but calculations made here suggest a recurrence time of 95 yr.

In search of a model that fits the observations and also allows for a reasonable ^{12}C ignition recurrence timescale, the recurrence time, outburst length, and mass accretion rate for this source were studied. While there are combinations of the recurrence time and outburst length that give reasonable ^{12}C ignition recurrence times, these models are inconsistent with the observed luminosity. In addition, no constraints can be placed on the outburst recurrence time. Though an immediate drop-off in accretion is unlikely, a more accurate profile of the behavior of the accretion was found to disagree with the observations. Finally, it was found that the ratio L_{acc}/L_{q1} is a useful observational quantity independent of distance. This ratio gives a clear distinction between the high- and low-conductivity cases for all mass accretion rates, and one can distinguish further between enhanced and standard cooling for the high-conductivity case at high mass accretion rates.

3.3 MXB 1659-298

3.3.1 Observations of the source

MXB 1659-298 was first discovered in outburst in 1976 by Lewin et al. [94] with *SAS 3* and remained bright for another 11 months. X-ray bursts from the source confirmed that the primary is a neutron star. Its position was confirmed with *HEAO 1* data by Doxsey et al. [45]. Shortly after, the source was found to exhibit eclipses with a 7.1 hr period [38, 39], confirming the presence of a companion object. It was observed to be in outburst again in 1999 [78] after a 21 yr period in quiescence. The source remained in outburst for 2.5 yr and returned to quiescence in 2001. MXB 1659-298 was observed by Wijnands et al. [162] using *RXTE* about a month after its return to quiescence with a flux of $\sim 3 \times 10^{-13}$ erg cm $^{-2}$ s $^{-1}$. It was observed again twice after this using *Chandra* [163]. During the 1.6 yr between the first and last observations studied by Wijnands et al. [163], the flux of the source decreased by a factor of 7 – 9. The distance range of 5 – 13 kpc determined by Wijnands et al. [163] is consistent with previous measurements by Oosterbroek et al. [109] and Munro et al. [104] who cited a distance of 10 – 13 kpc.

Since measurements of the distance to the source were not determined independently from the neutron star flux, the normalization was fixed with three different distances by Wijnands et al. [163] in their spectral analysis. These distances were kept fixed between observations and the column density was also kept fixed. Table 3.5 was taken from Wijnands et al. [163] and lists the bolometric flux for different assumed distances for each observation. Comparisons of this data to the cooling calculations were made using the 10 kpc distance.

While the outburst length and recurrence time have been observed, the mass accretion rate is more uncertain. Wijnands et al. [161] made a study of the behaviour of the X-ray bursts and concluded that the source exhibited both high- and low-

Table 3.5: Table of bolometric flux for different assumed distances at each observation. Fluxes listed are in units of 10^{-14} erg cm $^{-2}$ s $^{-1}$, unabsorbed.

Observation (MJD)	5 kpc	10 kpc	13 kpc
52197	61.6±4.2	42.1±2.9	37.7±2.8
52562	16.9±1.5	10.1±1.0	8.5±0.8
52768	8.9 $^{+1.4}_{-0.4}$	5.1±0.9	4.2±0.6

accretion rate bursts, though they make no estimates as to what the accretion rate should be. To approximate the accretion rate, one needs to know the luminosity or the flux and distance to the source. Table 1 of Wijnands et al. [161] lists the properties of a number of X-ray bursts from MXB 1659-298. A mean persistent flux can be taken to be $\sim 9 \times 10^{-10}$ erg cm $^{-2}$ s $^{-1}$. During the outburst, the luminosity is given by Equation (3.37). Assuming a distance of 10 kpc, the outburst accretion rate is calculated to be 5.8×10^{16} g s $^{-1}$. However, this value is quite uncertain given the error in the distance and non-continuous flux, variable by a factor of two.

3.3.2 Calculations

Assuming an outburst length of 2.5 yr and a quiescent period of 20 yr, the lightcurves of MXB 1659-298 were calculated using the same procedure as discussed in Section 3.1.3. The estimated mass accretion rate, $\dot{M} = 5.8 \times 10^{16}$ g s $^{-1}$ was used here. To compare the cooling curves with the observations [163], the flux at MJD 52768 and 10 kpc (Table 3.5) and the calculated luminosity at MJD 52768 for the high-conductivity/enhanced cooling case were used to calculate a distance to the source: 7 kpc, in reasonable agreement with the 10 kpc suggested by Wijnands et al. [163]. When using the same flux and the calculated luminosity for the high-conductivity/standard cooling case, one obtains a distance of 18 kpc, out of the range of error on the distance estimate.

Luminosities at each observation point were then calculated using the distances obtained from the calculated lightcurves as described above and the fluxes at 10 kpc

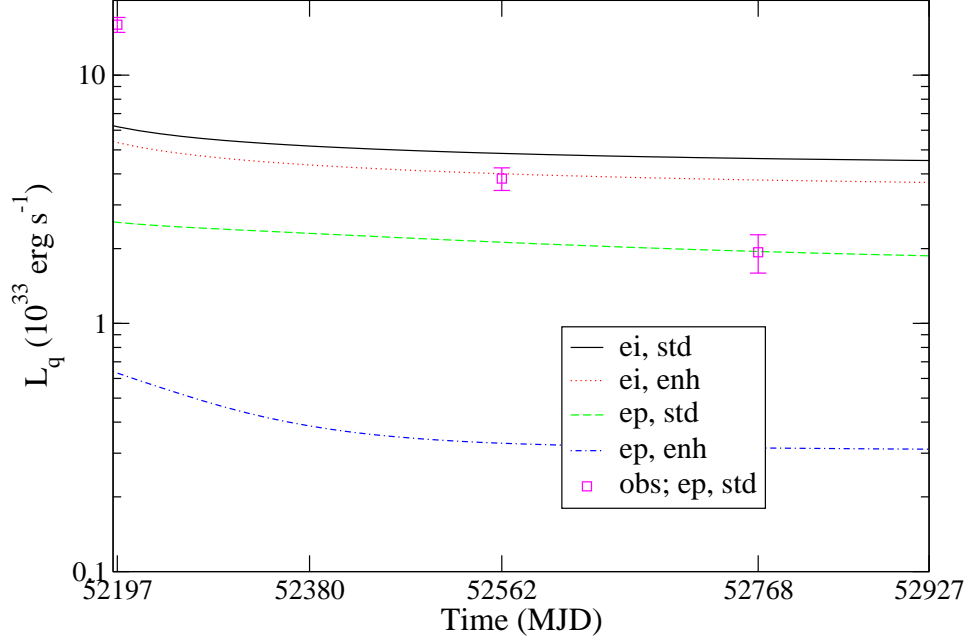


Figure 3.11: Lightcurves of MXB 1659-298 for various models. The squares show luminosities calculated from the fluxes listed under 10 kpc in Table 3.5 normalized to the high-conductivity/standard cooling curve at $t = \text{MJD } 52768$.

listed in Table 3.5. Cooling curves for the various models are shown in Figure 3.11 with the observations normalized to a distance of 18 kpc and Figure 3.12 with the observations normalized to a distance of 7 kpc. It is evident that the cooling curves for the low-conductivity cases are too luminous to agree with the data. Due to the rate of cooling after the outburst and distance estimate, the high-conductivity/enhanced cooling case gives the most likely state of MXB 1659-298. As can be seen in Figures 3.11 and 3.12, the observed luminosity points fall on a line which is much steeper than either the high-conductivity/standard cooling case or the high-conductivity/enhanced cooling case. Because the calculations here assumed accretion that acted as a step function and did not have a slow rise to maximum accretion or slow return to quiescence, the observations suggest that the actual source could have some residual accretion after the major outburst period which would keep the initial quiescent flux higher than the calculations. This is a likely scenario since other sources (e.g. Aql X-1) show signs of residual accretion resulting in a variable quiescent luminosity.

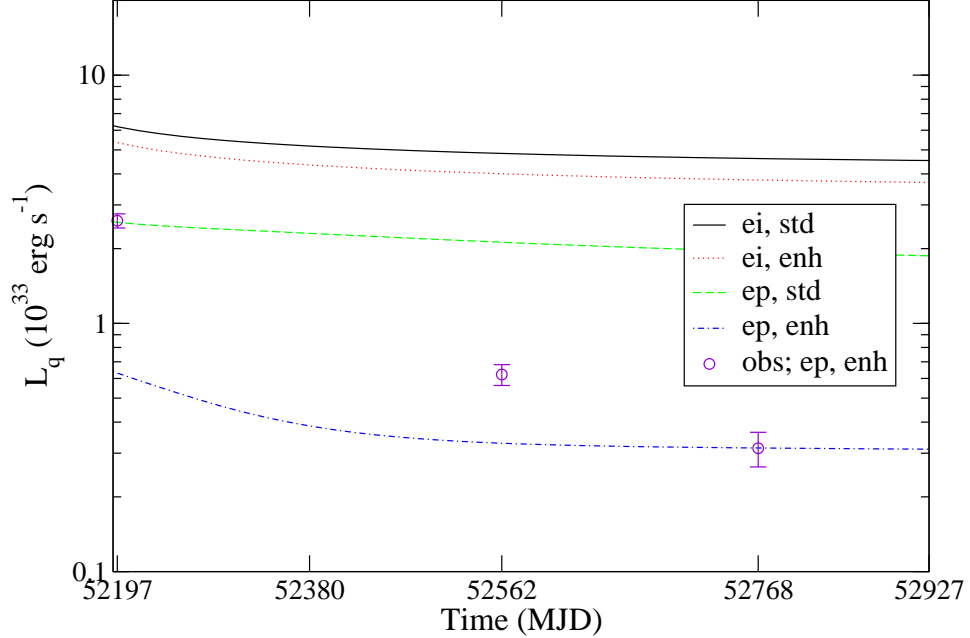


Figure 3.12: Lightcurves of MXB 1659-298 for various models. The circles show luminosities calculated from the fluxes listed under 10 kpc in Table 3.5 normalized to the high-conductivity/enhanced cooling curve at $t = \text{MJD } 52768$.

The calculations made here are a nice complement to the conclusions of Wijnands et al. [163], who suggested the presence of both a high-conductivity crust and enhanced core cooling in this source based on the rapid decrease in quiescent luminosity. These calculations take into account the long-term behaviour of MXB 1659-298, assuming that its behaviour is consistent over its history. As Wijnands et al. [163] mention, this long-term evolution of the source is important in comparing observations to the calculations. Consequently, it appears from these long-term evolution calculations that there is evidence of a high-conductivity crust in this neutron star source. Additional flux measurements and a tighter error on the distance measurement would serve to better constrain the interior properties of this source.

Since there has only been one quiescent interval observed, the recurrence time for this source was varied from 5 – 50 yr with a resulting difference in luminosity at $t = 0.1$ yr after the outburst of $10^{32} \text{ erg s}^{-1}$. It is not likely that this difference is observable. Considering the uncertainties on distance and mass accretion behavior,

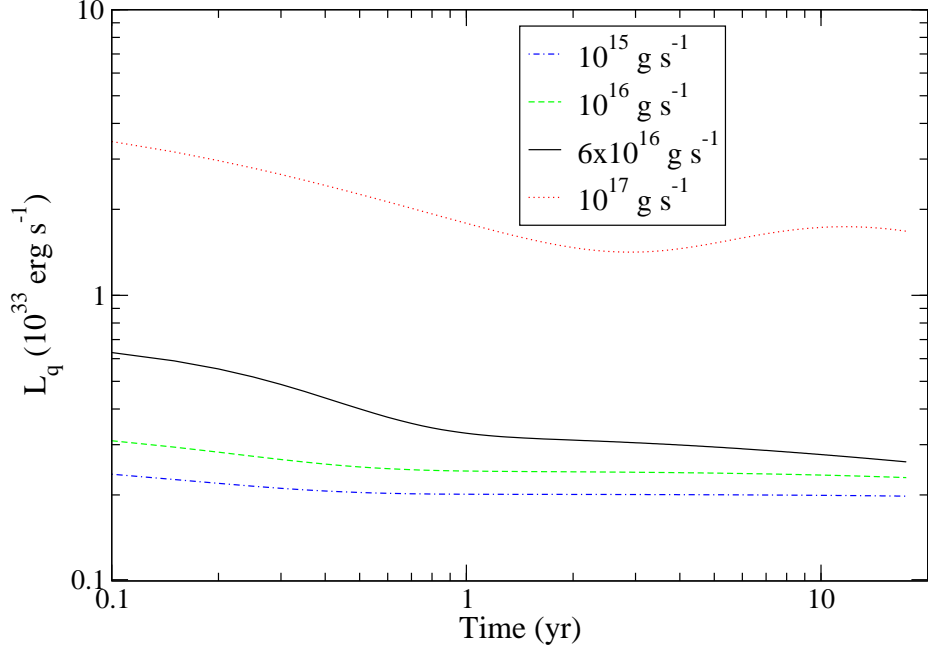


Figure 3.13: Lightcurves of MXB 1659-298 for various mass accretion rates calculated with the high-conductivity/enhanced cooling model.

no constraints can be placed on the recurrence time based on these calculations.

Because the mass accretion rate of MXB 1659-298 is unconstrained, the outburst accretion rate was varied from $10^{15} - 10^{17} \text{ g s}^{-1}$ and the results are shown in Figure 3.13. These calculations were made using the high-conductivity/enhanced cooling model since this is the model for the calculated accretion rate which gives a distance in agreement with previous estimates. While the calculations for 10^{16} and 10^{15} g s^{-1} are shallower than the calculation for $6 \times 10^{16} \text{ g s}^{-1}$, these mass accretion rates cannot be ruled out, as some residual accretion may occur after the outburst which is not taken into account in these calculations. Comparing observations to the quiescent luminosity at 1.6 yr for the calculation of $\dot{M} = 10^{17} \text{ g s}^{-1}$ yields a distance of 16 kpc, slightly out of the likely range of distances stated previously. A calculation of L_{acc}/L_{q1} for this source shows the same relationship as for KS 1731-260, including the turnover in the relationship for the high-conductivity/enhanced cooling case.

3.3.3 Summary

The neutron star transient MXB 1659-298 was modeled as it cooled from an accretion outburst into quiescence, and from the calculations it is not possible to constrain the behavior of this source. Based on the calculations, it would seem that the star is composed of a high-conductivity crust and a core which exhibits enhanced neutrino cooling. This model yields a distance estimate in accordance with previous measurements. It is likely that this source is host to some residual accretion which would keep the luminosity curve steeper than the calculations show. The outburst mass accretion rate for this source is very uncertain, so calculations were made in an attempt to constrain it. While a mass accretion rate of 10^{17} g s^{-1} provides the steepest decline in quiescent luminosity, the distance calculated for this model is out of the range of error on previous measurements. In addition, the difference in quiescent luminosity between calculations with recurrence times 5 – 50 yr is too small to be observed, so these calculations do not serve to constrain the outburst recurrence time. Again, residual accretion would explain the discrepancy between observation and calculation. If this is the case, it would show that not all transient neutron star luminosities are dominated by thermal emission.

3.4 Evolution of quiescent luminosity: a parameter study

In order to survey the parameter space for transient neutron stars, a series of cooling curves was calculated for different values of outburst length, recurrence time, and outburst mass accretion rate within each of the conductivity and neutrino cooling models. Table 3.6 lists the range of parameters used. Figure 3.14 shows graphically a small portion of the parameter space. The upper bound on the outburst length matches the observed outburst length of KS 1731-260. The lower bound was chosen

Table 3.6: Parameters used for the study of cooling curves. Refer to Table 3.3 for the definition of the various models.

Model	\dot{M}_{ob} (g s^{-1})	τ_{ob} (yr)	τ_{rec} (yr)
ei, std	10^{15}	1	2
ei, enh	10^{16}	2.5	5
ep, std	10^{17}	3	10
ep, enh		6	20
		10	50
		12	100
			300
			500
			1500

to be an extension of the work by Ushomirsky & Rutledge [151] and corresponds to an outburst length slightly longer than that of Aql X-1. The shortest recurrence time is determined by the length of the outburst, i.e. the recurrence time cannot be shorter than the length of the outburst. In order to study the cooling of the crust, the upper bound on the recurrence time was set to 1500 yr, the estimated recurrence time of KS 1731-260 [124]. Times longer than this approach the cooling timescale of the core and would thus affect the results. A quiescent cooling curve was calculated following the method presented in Section 3.1.3 for each combination of model, mass accretion rate, outburst length, and recurrence time resulting in a total of 528 cooling curves.

3.4.1 Results

Figures 3.15 – 3.26 show the quiescent luminosity at $t = 1$ yr after the end of the outburst, L_{q1} , as a function of outburst length, τ_{ob} , and recurrence time, τ_{rec} . This parameter gives a quick estimate of how quickly the neutron star crust cools immediately after the outburst. It is also a value which can be measured shortly after a transient neutron star outburst has ended. Each red plus marks the value of L_{q1} obtained for a run. The area enclosed by four values of L_{q1} is colored based on the value interpolated for the four points. In each plot is an extra disconnected point which

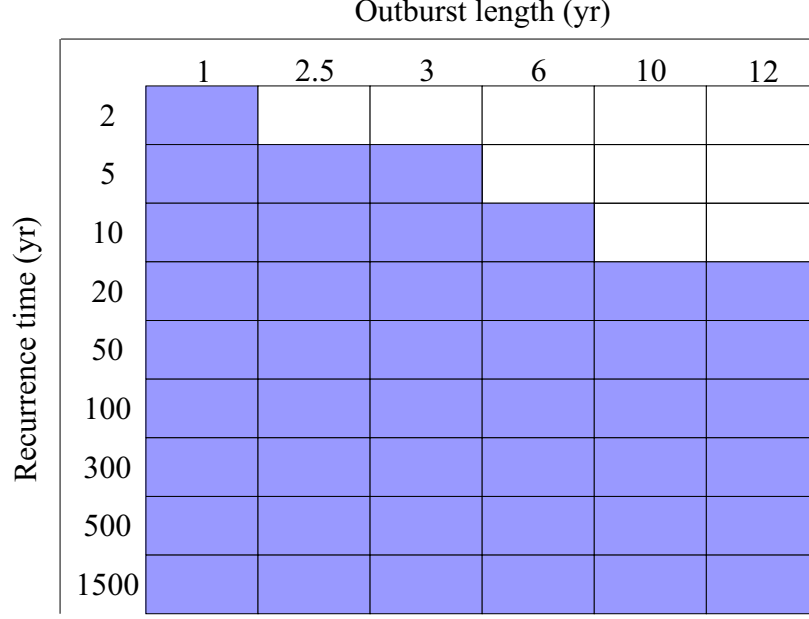


Figure 3.14: One twelfth of the cooling curve parameter space. An identical space exists for each mass accretion rate within each model. The empty boxes represent non-physical runs.

corresponds to $\tau_{ob} = 1$ yr, $\tau_{rec} = 2$ yr. It is disconnected from the grid due to the non-symmetric grid resolution. While L_{q1} for each mass accretion rate within a given model has been plotted on the same z -axis scale for comparison purposes, the color value scale shows finer detail.

The first general trend to note is that L_{q1} decreases as the recurrence time increases and as the outburst length decreases. In addition, it is obvious that L_{q1} increases with increasing mass accretion rate. This was previously illustrated for the sources KS 1731-260 (Figure 3.9) and MXB 1659-298 (Figure 3.13). The average mass accretion rate for a source is given by $\langle \dot{M} \rangle \approx \dot{M}_{ob} \tau_{ob} / \tau_{rec}$. This relationship determines the average amount of heat deposited in the crust over a series of outbursts. L_{q1} increases as this average mass accretion rate increases.

The overall range of the quiescent luminosity at $t = 1$ yr after the outburst is $10^{32} \leq L_{q1} \leq 2.8 \times 10^{34}$ erg s $^{-1}$. While it would be difficult to determine the conductivity of the crust and type of neutrino cooling from the core based solely on

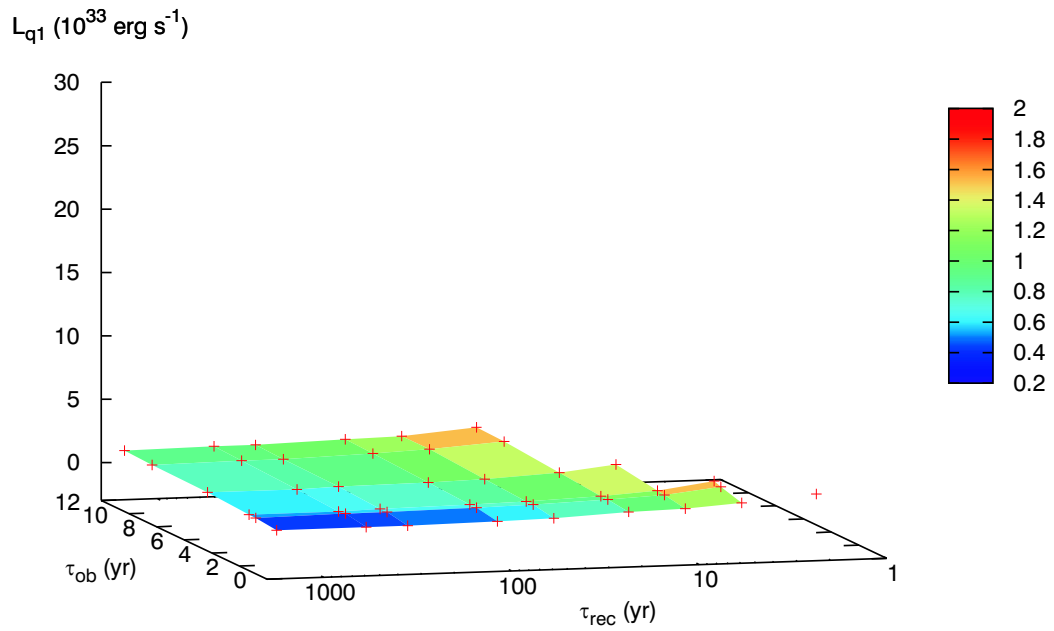


Figure 3.15: L_{q1} in the parameter space for low conductivity and standard cooling at a mass accretion rate of 10^{15} g s^{-1} .

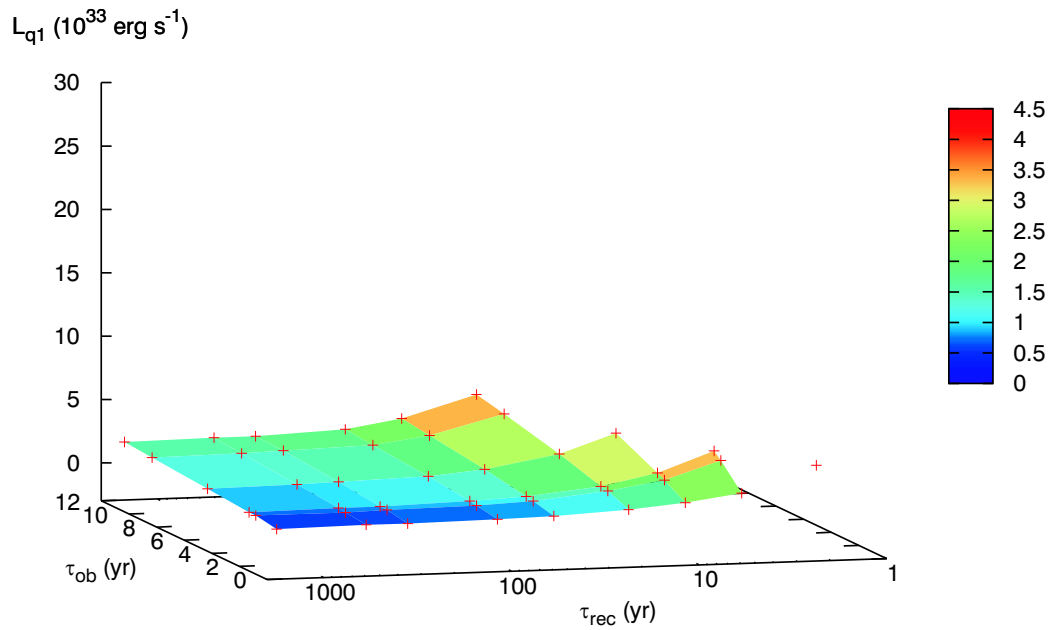


Figure 3.16: L_{q1} in the parameter space for low conductivity and standard cooling at a mass accretion rate of 10^{16} g s^{-1} .

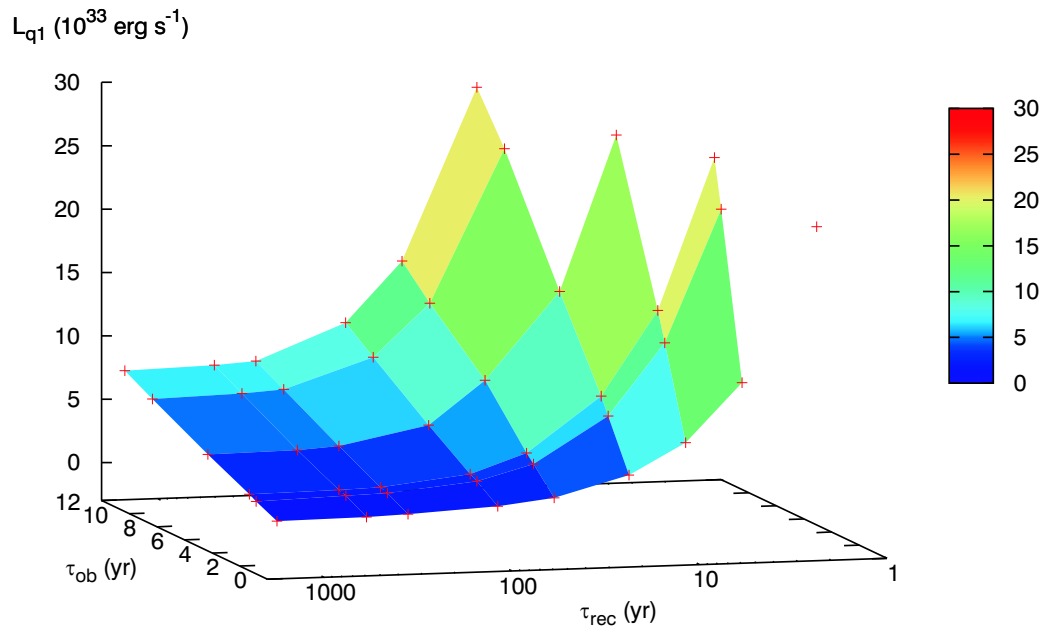


Figure 3.17: L_{q1} in the parameter space for low conductivity and standard cooling at a mass accretion rate of 10^{17} g s^{-1} .

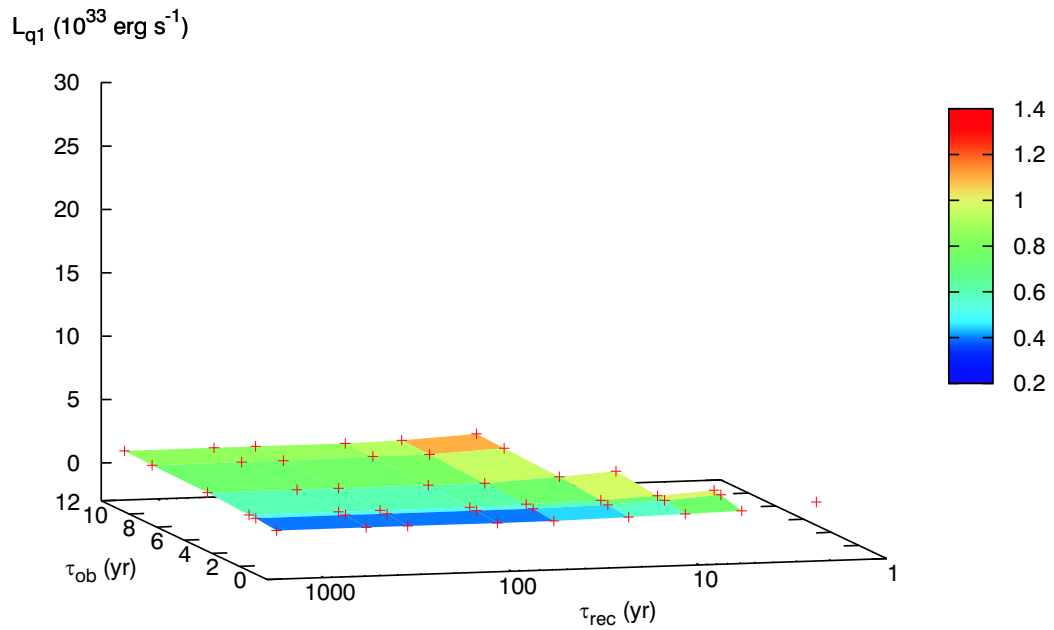


Figure 3.18: L_{q1} in the parameter space for low conductivity and enhanced cooling at a mass accretion rate of 10^{15} g s^{-1} .

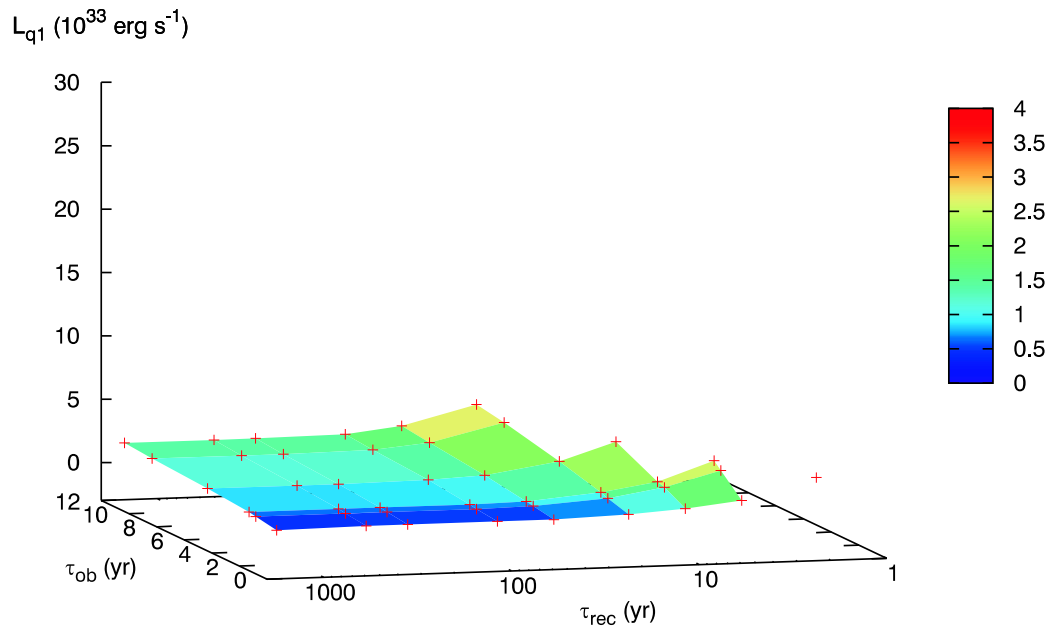


Figure 3.19: L_{q1} in the parameter space for low conductivity and enhanced cooling at a mass accretion rate of 10^{16} g s^{-1} .

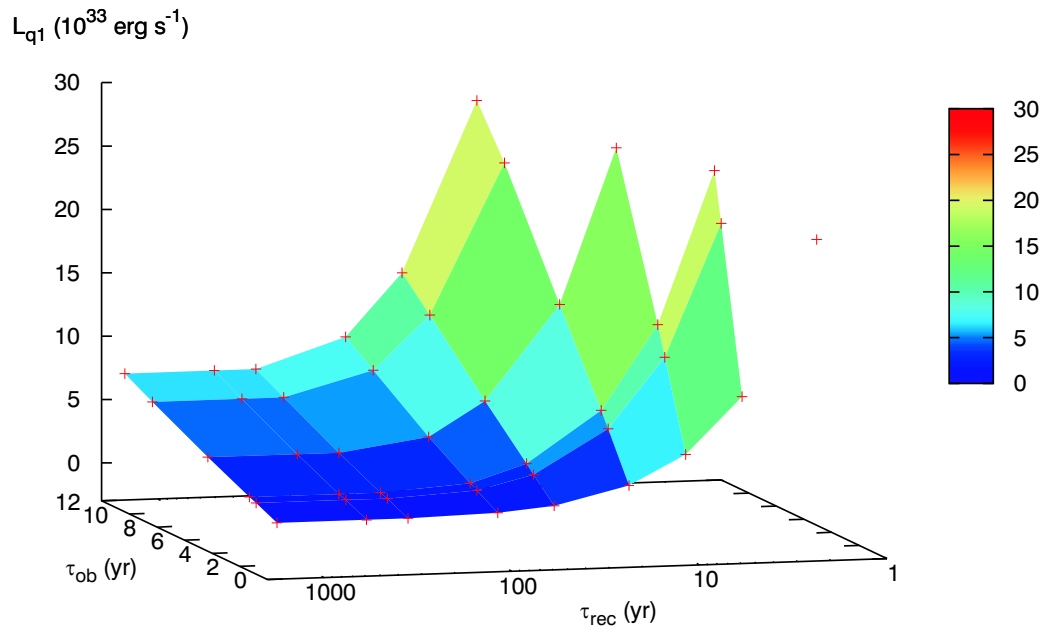


Figure 3.20: L_{q1} in the parameter space for low conductivity and enhanced cooling at a mass accretion rate of 10^{17} g s^{-1} .

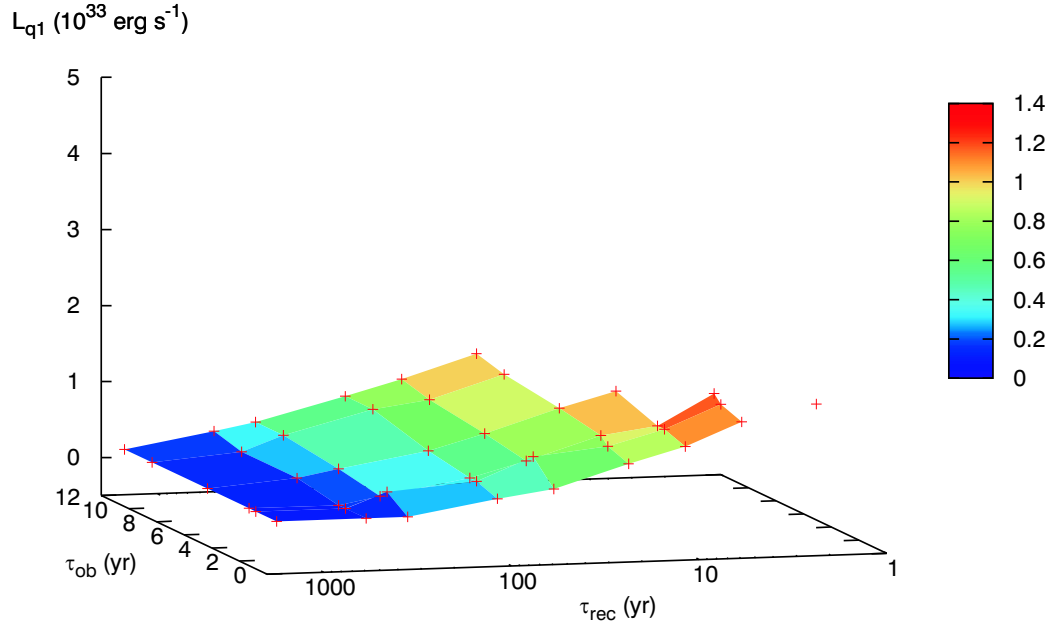


Figure 3.21: L_{q1} in the parameter space for high conductivity and standard cooling at a mass accretion rate of 10^{15} g s^{-1} .

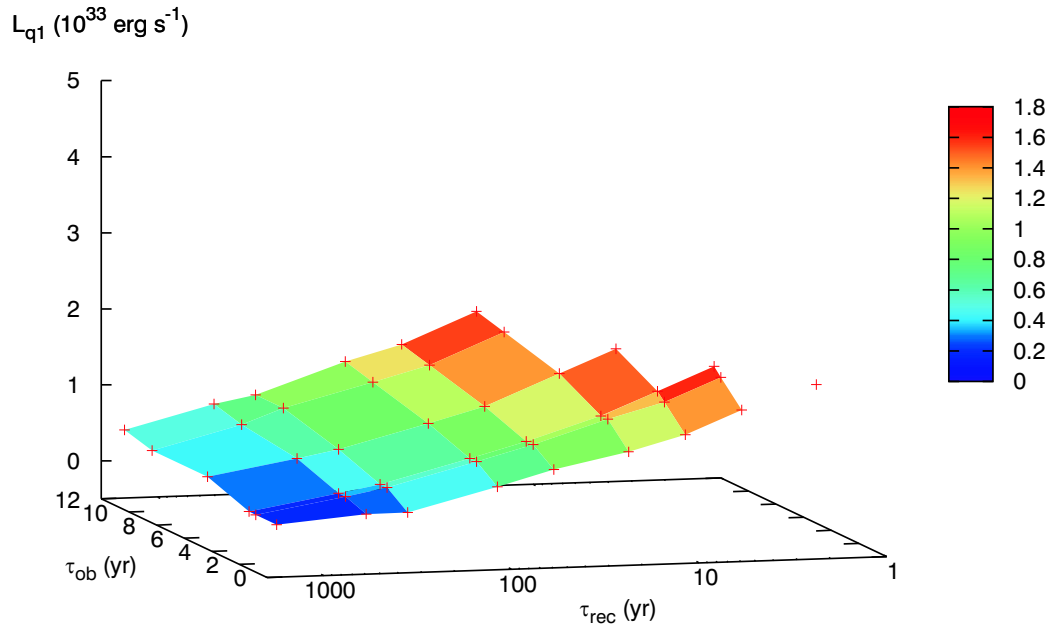


Figure 3.22: L_{q1} in the parameter space for high conductivity and standard cooling at a mass accretion rate of 10^{16} g s^{-1} .

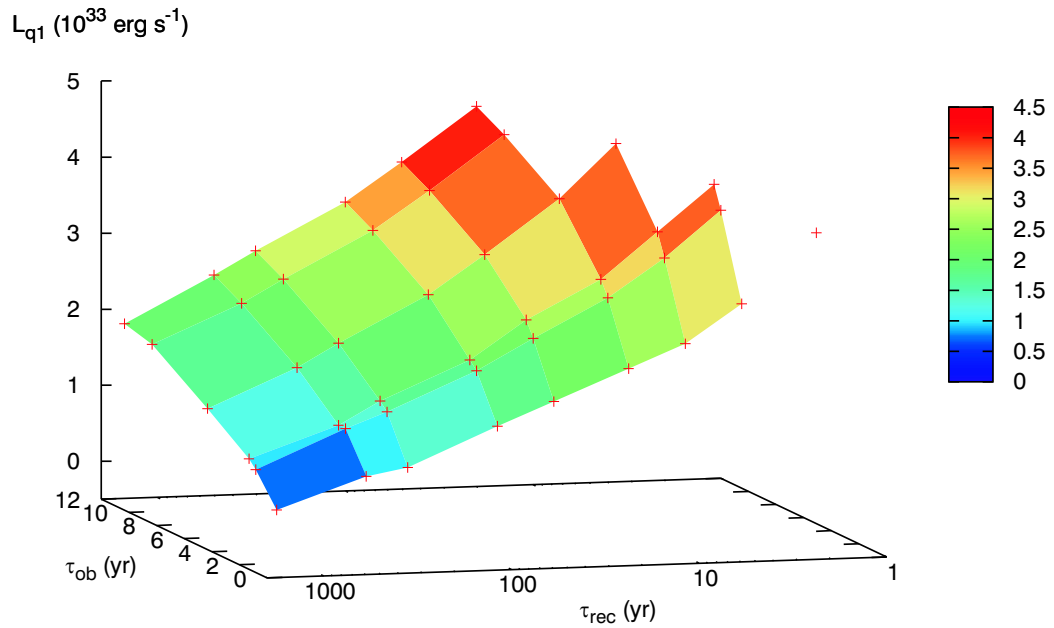


Figure 3.23: L_{q1} in the parameter space for high conductivity and standard cooling at a mass accretion rate of 10^{17} g s^{-1} .

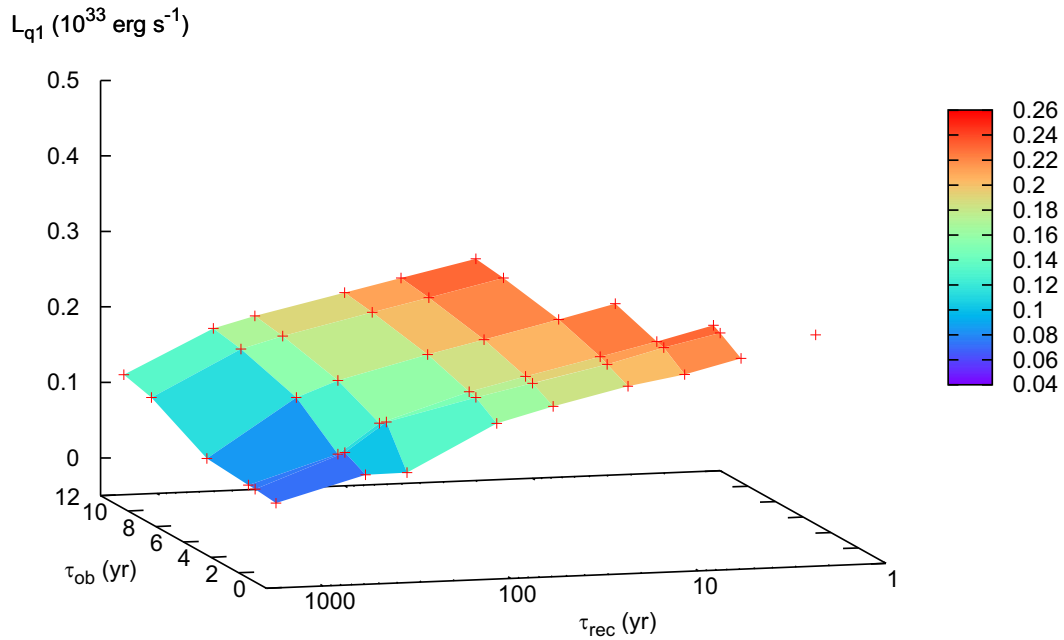


Figure 3.24: L_{q1} in the parameter space for high conductivity and enhanced cooling at a mass accretion rate of 10^{15} g s^{-1} .

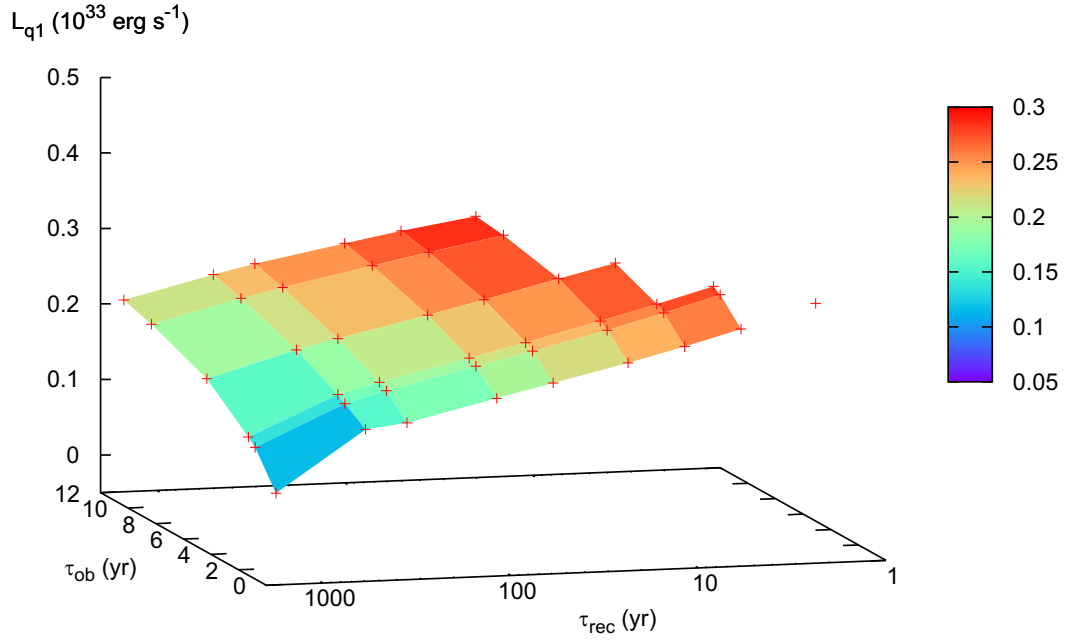


Figure 3.25: L_{q1} in the parameter space for high conductivity and enhanced cooling at a mass accretion rate of 10^{16} g s^{-1} .

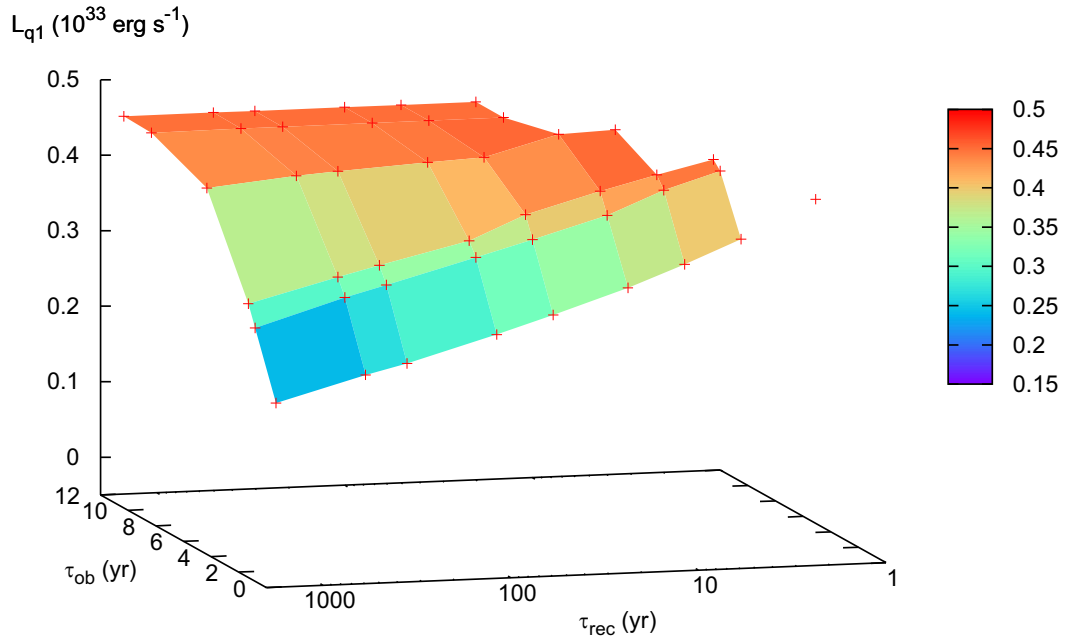


Figure 3.26: L_{q1} in the parameter space for high conductivity and enhanced cooling at a mass accretion rate of 10^{17} g s^{-1} .

an observed value of L_{q1} , some definite ranges of L_{q1} can be assigned, provided that the deep-crust heating formulation gives the correct amount of heat deposition. Over the entire parameter space, $L_{q1} > 5 \times 10^{33} \text{ erg s}^{-1}$ corresponds to neutron stars with low-conductivity crusts. Values of $L_{q1} < 3 \times 10^{32} \text{ erg s}^{-1}$ correspond to neutron stars with high-conductivity crusts. It is more difficult to differentiate between the types of neutrino cooling since a fairly large range, $3 \times 10^{32} < L_{q1} < 5 \times 10^{33} \text{ erg s}^{-1}$, overlaps both the low- and high-conductivity cases. This can be seen in a comparison between the standard and enhanced cooling for a low-conductivity crust. Because the conductivity is low, heat takes longer to move through the crust, and thus, more heat builds up in the crust during the outburst. The difference between standard and enhanced cooling is more clear in the high-conductivity case since heat can flow more freely through the crust. Thus, after the outburst the heat emission is less than in the low-conductivity case, so the smaller variations due to cooling from the core are more visible.

If the uncertainty in quiescent luminosity obtained from observation is assumed to be $5 \times 10^{32} \text{ erg s}^{-1}$, there is very little observable variation in L_{q1} beyond $\tau_{rec} = 300$ yr for a given outburst length for any model and accretion rate (see, in particular, Figure 3.17). This recurrence time is on the order of the time it takes for heat to flow from the inner crust to the top of the crust (Figure 3.1). Beyond this time, all of the heat that was deposited in the crust during the outburst has had time to flow to the surface.

For the high-conductivity case where the heat flows much more rapidly through the crust, it would be very difficult to distinguish between different outburst lengths and recurrence times since the heat left in the crust at the end of the outburst is so small in general (Figures 3.21 - 3.26). While there are possibly observable differences in outburst length for the low-conductivity cases with a given recurrence time, the largest difference in L_{q1} as a function of outburst length for the high-conductivity

cases is $2 \times 10^{33} \text{ erg s}^{-1}$ (Figure 3.23). This difference is not larger than $5 \times 10^{32} \text{ erg s}^{-1}$ for the high-conductivity/enhanced cooling cases (Figures 3.24 - 3.26), meaning that determining an outburst length and recurrence time from these calculations for a given observation is not possible.

Moreover, the claim of Rutledge et al. [124] that a recurrence timescale of 200 yr is the lower limit for KS 1731-260 can be regarded in light of Figure 3.26. This figure shows the high-conductivity/enhanced cooling case for a mass accretion rate of 10^{17} g s^{-1} , slightly below the inferred value for KS 1731-260. For an outburst length of 12 yr it is clear that there is very little change in L_{q1} for recurrence times even shorter than 200 yr, so there is no need to require a long recurrence time for this source.

3.4.2 Summary

In order to provide the astronomical community with a series of calculations to be compared with observations, the general trends found in this parameter study are as follows: (1) A low-conductivity crust can be assigned to neutron stars with observed values of L_{q1} greater than $5 \times 10^{33} \text{ erg s}^{-1}$. In contrast, neutron stars with observed values of L_{q1} less than $3 \times 10^{32} \text{ erg s}^{-1}$ can be assigned a high-conductivity crust. (2) For a given model and mass accretion rate, L_{q1} decreases for increasing recurrence time and decreasing outburst length. (3) Lower mass accretion rates result in less heat deposition during the outburst; hence, L_{q1} is lower for lower mass accretion rates.

3.5 Future work

Though the calculations presented here are the first comprehensive study of how the properties of neutron star transients affect cooling from an outburst state into quiescence, there are still many facets of the problem to be considered.

First, the heat deposition in the neutron star for these calculations was taken

from Haensel & Zdunik [66], who considered only one nuclear species. A more accurate model of heat deposition would result from the use of the complete range of ashes from the rp-process synthesized through electron capture and pycnonuclear calculations. Initial studies of these electron captures are presented in Chapter 4. Considering a range of nuclei may affect the energy production, resulting in a different thermal profile in the crust, and thus, a different quiescent luminosity curve. In addition, the cooling calculations should test the results of Jones [83], who predicts an energy release due to non-equilibrium reactions less than that given by Haensel & Zdunik [66].

In addition, a study should be made to test the effect of the mass accretion behavior at the beginning of, and especially at the end of an outburst. A preliminary test of this effect was made (Figure 3.6). The figure shows that a variable mass accretion rate affects a high-conductivity crust by reducing the quiescent luminosity significantly in the first year of quiescence. The mass accretion rate in this case was made to decrease linearly during the last four years of the outburst. While calculations of KS 1731-260 with a decreasing accretion rate were less consistent with the observations than the constant accretion rate, the observations of MXB 1659-298 could possibly be better fit with a variable accretion rate model. The duration of dropoff and non-linear dropoff behaviours need to be studied, as well as the effects of residual accretion.

Finally, the question of the origin of the superburst observed for KS 1731-260 needs to be investigated. As was shown here, the cooling calculations for a high-conductivity/enhanced cooling model agree with the observations to within the uncertainty. However, it was also shown that the recurrence time for unstable ^{12}C ignition is incompatible with the recurrence time calculated from the energetics of the burst. The nuclear physics of the outbursts and the isotopic composition of the superburst region should be studied in more detail to explain this discrepancy.

Chapter 4

Electron Captures in Neutron Star Crusts

4.1 Theory

To calculate the series of electron captures as the primary heating source in the crust of the neutron star, it is necessary to solve the thermal structure of the star in conjunction with a nuclear network. The thermal model used in this calculation is from Brown [23] and is nearly identical to that discussed in Section 3.1. The calculations of the nuclear network follow the method of Schatz et al. [128, 129].

4.1.1 Thermal structure

The thermal structure of the neutron star crust is calculated following Brown [23]. The crust is assumed to be thin compared to its radius, so the redshift, $z = (1 - 2GM/(Rc^2))^{-1/2} - 1$, is nearly constant over the crust. Because the crust is thin and the rate of mass accretion is small, the depths at which nuclear burning take place are assumed to be fixed. The nuclear burning is then treated as a stationary front through which material is being advected. The flow is very subsonic, and everything

is stationary, so the energy equation [88] is given by Equation (3.1), which can be written in the steady-state approximation as

$$\nabla \cdot (\rho H \mathbf{u} + \mathbf{F}) = 0. \quad (4.1)$$

Here, H is the enthalpy and \mathbf{u} is the velocity of the material being pushed through the flame front; \mathbf{F} is the energy flux. With $H = G + TS$, where G is the Gibbs energy, and the continuity equation, $\nabla \cdot (\rho \mathbf{u}) = 0$, Equation (4.1) can be written as

$$T \frac{dS}{dt} = -\frac{1}{\rho} \nabla \cdot \mathbf{F} - \frac{dG}{dt} - \frac{1}{\rho} \nabla \cdot \mathbf{F}_\nu, \quad (4.2)$$

where \mathbf{F}_ν is the flux from neutrinos produced in nuclear interactions. Here, d/dt denotes the Lagrangian derivative $\partial/\partial t + \mathbf{u} \cdot \nabla$.

Because the calculations are one-dimensional, time may be used as the independent Lagrangian coordinate. Thus, $\partial_z = -(\rho/\dot{m})\partial_t$. At a constant pressure, the specific heat, $c_P = T(ds/dT)_P$, and the left-hand side of Equation (4.2) can be expressed as

$$T \frac{ds}{dT} = c_P \frac{dT}{dt} + T \left(\frac{\partial s}{\partial P} \right)_T \left(\frac{dP}{dt} \right). \quad (4.3)$$

With the thermodynamic relation

$$\left(\frac{\partial s}{\partial P} \right)_T = - \left(\frac{\partial s}{\partial T} \right)_P \left(\frac{\partial T}{\partial P} \right)_s, \quad (4.4)$$

Equation 4.3 can be written as

$$T \frac{ds}{dT} = c_P \left(\frac{dT}{dt} - \frac{T}{P} \nabla_{ad} \frac{dP}{dt} \right), \quad (4.5)$$

where $\nabla_{ab} \equiv (\partial \ln T / \partial \ln P)_s$ is the adiabat. Using the fact that in hydrostatic balance

the pressure is $P(t) = mgt$, Equation (4.2) can then be written in its final form as

$$\frac{dF}{dt} = \dot{m} \left(c_p \frac{dT}{dt} - c_p \frac{T}{t} \nabla_{ab} - \varepsilon_N + \varepsilon_\nu \right). \quad (4.6)$$

The heat input is provided by nuclear reactions, ε_N , and ε_ν is the neutrino emissivity (Section 4.1.1). Equation (3.2) can be written as

$$\frac{dT}{dt} = \dot{m} \frac{F}{\rho K}. \quad (4.7)$$

Equations (4.6) and (4.7) describe the thermal structure of the crust.

Energy production

Because the difference in pressure over the reaction layer is small, the heat evolved may be calculated from the change in the Gibbs energy: $\delta Q = -\delta G$. From Equation (4.2), the net heating rate can be expressed as

$$\varepsilon = -\frac{dG}{dt} - \frac{1}{\rho} \nabla \cdot \mathbf{F}_\nu. \quad (4.8)$$

The first term in Equation (4.8) becomes

$$\frac{dG}{dt} = N_A \left(\sum_i \mu_i \frac{dY_i}{dt} + \mu_e \frac{dY_e}{dt} \right), \quad (4.9)$$

where μ_i is the chemical potential of species i , and μ_e is the electron chemical potential, both of which include the rest mass. The abundance of a given isotope is $Y_i = X_i/A_i$ and Y_e is the electron abundance.

The neutrino loss term in Equation (4.8) is related to the change in electron abundance via

$$\frac{1}{\rho} \nabla \cdot \mathbf{F}_\nu = N_A \sum_{i,j} E_\nu^{i,j} \frac{dY_e}{dt} \Big|_{i,j}. \quad (4.10)$$

The sum here is over all electron capture energy levels linking isotopes i and j ; $E_\nu^{i,j}$ is the neutrino energy averaged over these energy levels. Because no nuclear excited states are included in this calculation, there is only one energy level for each nucleus involved in a capture, and so this sum reduces to a sum over all isotopes.

Combining Equations (4.9) and (4.10), the reaction energy evolved in a given timestep (Equation [4.8]) then becomes

$$\varepsilon = -N_A \left[\sum_i \mu_i \frac{dY_i}{dt} + \frac{dY_e}{dt} \left(\mu_e + \sum_{i,j} E_\nu^{i,j} \right) \right]. \quad (4.11)$$

Deriving the energy in such a way, the Coulomb interactions should be incorporated into μ_i ; however, this is difficult to implement. First, the free energy has not been studied for a large mixture of ionic species. Numerical calculations of mixtures of two species show that a linear interpolation of the energies of pure phases, $\sum Y_i G_i$, gives reasonable results, though the calculation of the free energy is rather complex. It is also not understood whether mixtures of different charge ratios will form a lattice or an alloy. Because the Coulomb properties depend only on the electron abundance, the equation of state routine used here simplifies the calculation of Coulomb interactions by treating the plasma as if it were composed of a single ion of $\langle A \rangle$ and $\langle Z \rangle$. In this manner, the interactions between species may be separated from the chemical potentials, and the quantity

$$- \left(\frac{\partial G}{\partial \langle Z \rangle} \right)_{T,P} \frac{d\langle Z \rangle}{dt} \quad (4.12)$$

is added to Equation (4.11). This term the lowest order approximation to the linear interpolation rule for the energies of pure phases, and other terms dependent on higher orders of $\langle Z \rangle$ are included in the calculation for completion. The numerics for Equation (4.12) are given by the Coulomb term in the fits of the free energy calculated by Farouki & Hamaguchi [48] and are dependent on Γ (Equation [3.7]). Substituting

the number density of electrons, $n_e = n\langle Z \rangle$, in Equation (3.7) shows that the lattice energy, Equation (4.12), is a function of $\langle Z^{5/3} \rangle$.

Physical input

The formulation of the equation of state, conductivity, and crust neutrino emission used in these calculations is the same as that used for the cooling calculations (Section 3.1.2) with a few minor differences. First, no superfluidity is taken into account in these calculations since there are no free neutrons in the density regime of interest.

Again, the dominant neutrino process in the crust is neutrino bremsstrahlung (Equation [3.23]), so the other contributions are expected to be negligible. Pair, plasma, and photo-neutrino processes which were not included in the cooling calculation are included here for completeness following the work of Itoh et al. [80].

Finally, since the numerical integration starts from the top of the crust and runs inward, a guess must be made about the flux at the top of the crust. A good estimate of this value is something less than 10^{22} erg cm⁻² s⁻¹, or about 0.1 MeV \dot{m} u⁻¹ [23] for the calculations of Haensel & Zdunik [66]. A run is executed with this guess to check for stability of the temperature and the flux is adjusted if necessary.

Nuclear reactions

In steady-state, the continuity equation for a species i with a number density n_i is

$$\nabla \cdot (n_i \mathbf{u}) = \sum_i r, \quad (4.13)$$

where $\sum_i r$ is the sum of the creation and destruction processes for that species. With a mass fraction defined as $X_i = A_i m_p n_i / \rho$, Equation (4.13) may be written as [129]

$$\dot{m} \frac{\partial X_i}{\partial y} = \frac{A_i m_p \sum r}{\rho}. \quad (4.14)$$

It is this equation which is solved in conjunction with Equation (4.6) to determine the nuclear energy generation rate (Equation [4.11]) and the nuclear abundances, Y_i . Reaction rates (Section 4.1.2) are given by r , which is sum of particle creation and destruction rates. For three species, this is expressed as

$$\sum r = Y_{i-1}\lambda_{i-1\rightarrow i} + Y_i\lambda_{i\rightarrow i+1} \quad (4.15)$$

Electron capture reaction rates are contained in λ_i .

4.1.2 Electron captures

Electron capture rates have been measured on Earth, but cannot be used for stellar calculations primarily because experimental rates involve electrons bound in atoms and the stellar environment consists of individual nuclei surrounded by an electron gas. Therefore, theoretical calculations of electron capture rates are used which include corrections to take into account properties of the stellar environment, effects from excited states, and extrapolation to the proper energy regime. Experimental results such as nuclear level properties and (ft) strengths are still useful as input to the calculations. Electron capture reaction rates used in this formulation were developed by Fuller, Fowler, & Newman [53–56]. More recent work has been done by Pruet & Fuller [120], who extended these rate calculations to $65 \leq A \leq 80$. In a different microscopic calculation, Nabi [105] used the proton-neutron quasiparticle random-phase approximation (pn-QRPA) to calculate rates for $18 \leq A \leq 100$. Electron capture rates have also been calculated by Langanke & Martínez-Pinedo [90] for $45 \leq A \leq 65$ and Langanke et al. [89] for $65 \leq A \leq 112$.

As a matter element gets compressed in the crust due to accretion, the electron

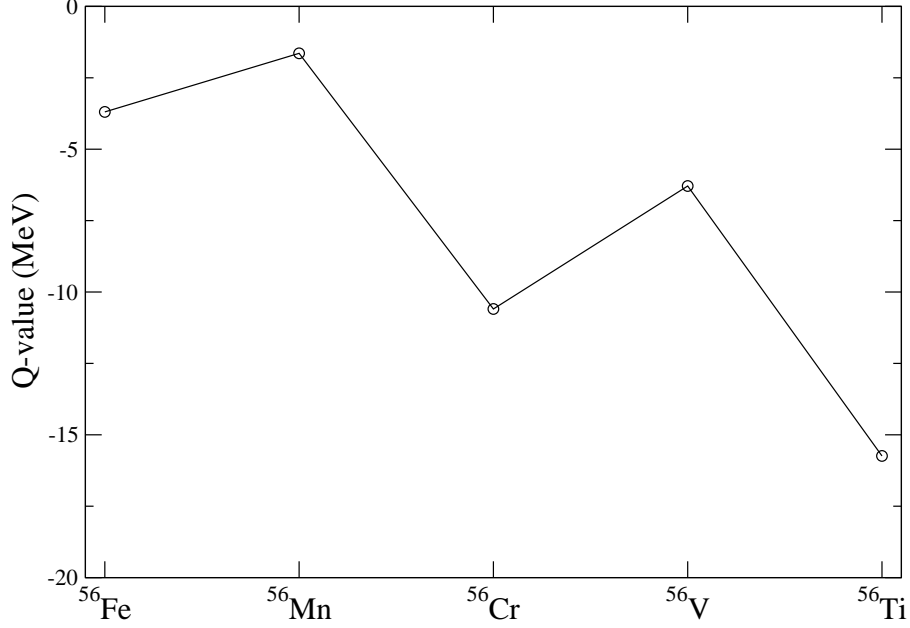
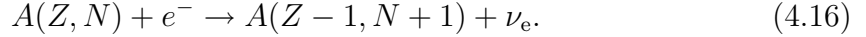


Figure 4.1: Atomic Q -values for nuclei included in the electron capture calculations.

Fermi energy rises, and electron captures will occur through the reaction [56]



In the $T = 0$ K approximation, the reaction onto an even-even nucleus will proceed as soon as the Fermi energy reaches the nuclear Q -value, q_n . A plot of the Q -values for nuclei included in this calculation is shown in Figure 4.1. Because of the odd-even effect, electron capture onto an even-even nucleus is followed immediately by electron capture onto an odd-even nucleus due to its low q_n . Thus, electron capture reactions proceed in pairs. A summary of the reactions taking place at each depth as calculated by Haensel & Zdunik [66] are listed in Table 3.2, which also includes the pycnonuclear reactions occurring deeper in the star. Only the first three entries of this table will be discussed here due to limitations in the available reaction rates.

The *nuclear* Q -value, q_n , is the mass-energy difference of the reaction in units of $m_e c^2$ [102]

$$q_n = \frac{1}{m_e c^2} (m_{nuc,p} - m_{nuc,d} + E_i - E_j), \quad (4.17)$$

where E_i and E_j are the energies of the excited parent and daughter states, respectively. The nuclear mass of the parent and daughter can be calculated from the tabulated mass excesses:

$$m_{nuc}(Z, N) = M(Z, N) + (Z + N)u - Zm_e + a_{el}Z^{2.39}. \quad (4.18)$$

Here, $M(Z, N)$ is the atomic mass excess, $u = 931.5014$ MeV, m_e is the electron mass, and $a_{el}Z^{2.39}$ represents the binding energy of Z electrons with $a_{el} = 1.433 \times 10^{-5}$ MeV.

Reaction rate calculations

At low temperatures and densities that correspond to Fermi energies near the reaction threshold, electron capture rates are dominated by captures from the parent ground state into the ground state of the daughter nucleus. With increasing density, transitions to excited states in the daughter nucleus also contribute to the rate. At higher temperatures, excited states in the parent nucleus also need to be taken into account. With many channels open, statistical approaches of calculation become possible. Fuller, Fowler & Newman [53–56] used the available experimental information for nuclei in the range $21 \leq A \leq 60$ along with shell-model calculations to estimate unmeasured Gamow-Teller matrix elements. Their results were made available in the form of a table [55] covering a temperature range of $0.01 \leq T_9 \leq 100$ and a density range of $10 \leq \rho/\mu$ (g cm^{-3}) $\leq 10^{11}$, and were used in the calculations presented here. A plot of these rates for the electron capture onto ^{56}Fe is shown in Figure 4.2. Here, ρ/μ is the mass density divided by the mean molecular weight per electron. Though Fuller, Fowler & Newman calculated rates for all lepton interactions, and all rates are included in the calculation, only those pertaining to electron captures will be discussed here.

The weak decay rate from a state i in the parent nucleus to a state j in the

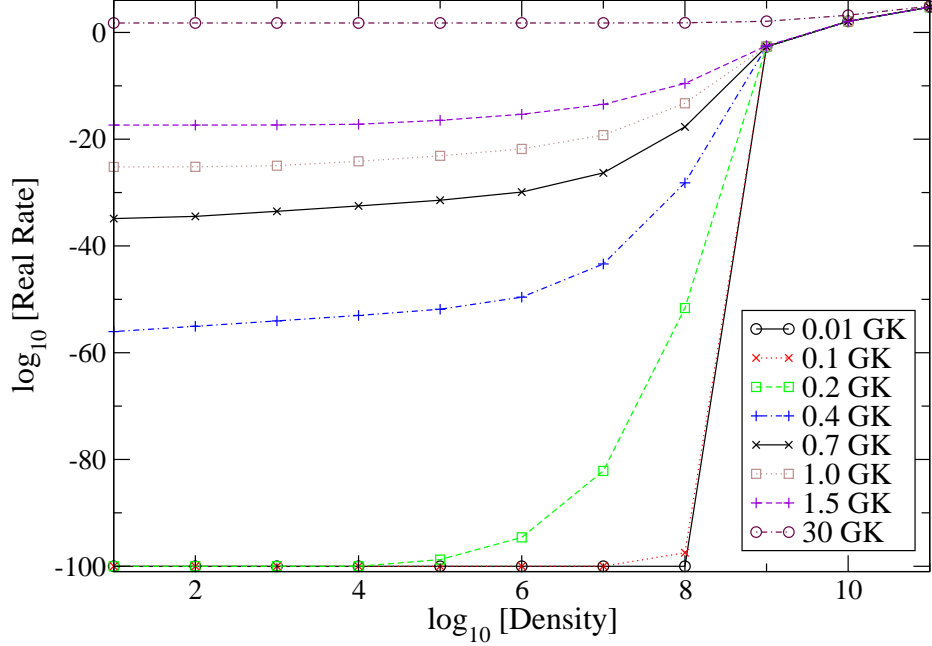


Figure 4.2: Reaction rates for electron capture on ^{56}Fe as calculated by Fuller, Fowler & Newman [55] for some temperatures of interest plotted as a function of $\log(\rho/\mu)$. Lines between points serve to guide the eye.

daughter is given by [53]

$$\lambda_{ij} = \ln 2 \frac{f_{ij}(T, \rho, \mu_e)}{(ft)_{ij}}, \quad (4.19)$$

where $(ft)_{ij}$ is the comparative half-life, and f_{ij} is the phase space integral described below. The comparative half-life is related to the allowed weak-interaction matrix elements by [19]

$$\log(ft)_{\text{GT}} = 3.596 - \log |M_{\text{GT}}|^2, \quad (4.20)$$

and

$$\log(ft)_{\text{F}} = 3.791 - \log |M_{\text{F}}|^2, \quad (4.21)$$

where $|M_{\text{GT}}|$ and $|M_{\text{F}}|$ are the Gamow-Teller and Fermi matrix elements, respectively.

The electron chemical potential is calculated from the density:

$$\begin{aligned}\mu_e &= \left[\left(1 + 1.02 \times 10^{-4} \left(\frac{\rho}{\mu} \right)^{2/3} \right)^{1/2} - 1 \right] \times m_e c^2 \\ &\approx 0.5 \times 10^{-2} \left(\frac{\rho}{\mu} \right)^{1/3} \text{ MeV.}\end{aligned}\tag{4.22}$$

The phase space integral, f_{ij} is given by [53]

$$f_{ij} = \int_{w_l}^{\infty} (q_n + w)^2 G(+Z, w) S(1 - S_\nu) w^2 dw,\tag{4.23}$$

where w is the total electron energy in units of $m_e c^2$, $w_l = |q_n|$, and

$$G(+Z, w) \equiv \frac{p}{w} F(+Z, w),\tag{4.24}$$

where $F(+Z, w)$ is the relativistic screening factor. Also, $p = (w^2 - 1)^{1/2}$ is the electron momentum in units of $m_e c$. S is the Fermi-Dirac distribution function for electrons, neglecting possible corrections from bound electrons and the ions:

$$S = \left(\exp \left(\frac{U - \mu_e}{kt} \right) + 1 \right)^{-1},\tag{4.25}$$

where $U = (w - 1)m_e c^2$ is the kinetic energy and μ_e is given by Equation (4.22). S_ν is the corresponding distribution for neutrinos. $S_\nu = 0$ here since inhibition of the final neutrino phase space is not important for these calculations.

The total weak transition rate is given by [53]

$$\lambda = \sum_i \sum_j P_i \lambda_{ij},\tag{4.26}$$

where, again, i is a parent state and j is a daughter state. P_i is the occupation index

$$P_i = \frac{(2J_i + 1) \exp(-E_i/kT)}{G}, \quad (4.27)$$

where J_i is the spin of level i and G is the nuclear partition function for the parent nucleus:

$$G = \sum_i (2J_i + 1) \exp(-E_i/kT). \quad (4.28)$$

Effective reaction rates

The electron capture rates of Fuller, Fowler & Newman [53] are available on a grid of temperature and density points. These rates are sensitive functions of temperature and density, and need to be interpolated. For capture interactions, not only is there a strong temperature dependence through the population of parent excited states, there are also considerable temperature and density dependences introduced through the electron distribution functions in the continuum phase space factors.

A plot of this temperature and density dependence is shown in Figure 4.2. As is clear, for temperatures of interest, $T \gtrsim 10^8$, there is a sharp transition between $10^8 < \rho/\mu$ (g cm^{-3}) $< 10^9$ at which the electron capture rate suddenly turns on. Due to the resolution of the grid, one is unable to determine the exact density and temperature where the rate becomes important. This problem can be alleviated by dividing out the continuum phase space capture integral to obtain an effective $\log(ft)$ value, $\log\langle ft \rangle_{eff}$. The effective rate varies over many fewer orders of magnitude than the real rate and can be more accurately interpolated.

Taking Equation (4.19) and rewriting it as [56]

$$\lambda = \ln 2 \frac{I_{eff}}{\langle ft \rangle_{eff}} \quad (4.29)$$

allows for the definition of the modified phase space factor

$$I_{eff} \equiv \frac{f_{eff}}{\langle G_{eff} \rangle}, \quad (4.30)$$

which is a complicated function of the constituent energies not reproduced here. In this equation, f_{eff} is the phase space factor as given in Equation (4.23) with the factor $G(+Z, w)$ removed from the integral and replaced by an average quantity $\langle G_{eff} \rangle$ in order to simplify the calculation. Also, $\langle ft \rangle_{eff}$ in Equation (4.29) is the effective value for $(ft)/\langle G_{eff} \rangle$. With these modifications, I_{eff} may be determined from Equations (4.23) and (4.25).

It is necessary to include q_n in Equation (4.23); however, and especially in these calculations where $T = 0$ K is not assumed, q_n should include energies of the nuclear excited states. What is currently used as the Q -value of the reaction is simply the difference in atomic mass excess of the parent and daughter nuclei, and this is reasonable in the assumption that the capture occurs between ground states. The excited states of both the parent and daughter nuclei should be taken into account, and this inclusion can introduce an error on the order of a few MeV in q_n for the onset of the electron capture. A few MeV is a sizeable fraction of q_n .

In the electron capture calculations presented here, the calculation of the effective rate has been implemented with a code provided by Langanke & Martínez-Pinedo [91], and the results for the ^{56}Fe electron capture can be seen in Figure 4.3.

This figure of effective rates versus density for each temperature yields some interesting insights. For temperatures higher than 10 GK, the effective rates vary smoothly with density as expected; the curve for $T = 30$ GK is shown as an example. However, for temperatures lower than 10 GK, an increased rate is seen at $\rho/\mu = 10^9$ g cm $^{-3}$. This is a result of the calculation for the very small rates found at low densities (see Figure 4.2). Furthermore, the effective rates calculated for the lowest temperatures

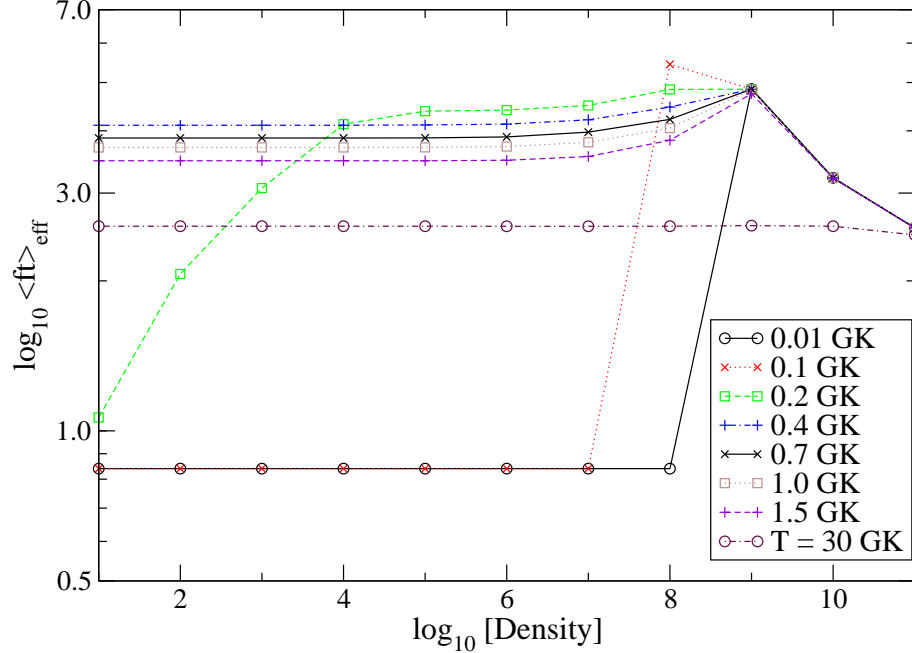


Figure 4.3: Effective reaction rates for electron capture on ^{56}Fe as calculated from the Langanke/Martínez-Pinedo code [91]. Rates for some temperatures of interest are plotted as a function of $\log(\rho/\mu)$.

are even more problematic. This is due to the numerical cutoff of the real rate when it is very small: the reaction rate is set to -99.999. This in turn leads to unrealistic calculations of the effective rate, and thus, inaccurate effective rate interpolations when trying to compute reaction chains. Following Fuller, Fowler & Newman, these very low reaction rates have been extrapolated from adjacent table entries [56].

4.1.3 Numerical method

The code is comprised of two main parts: the electron capture program, and the thermal routines. The electron capture program was modified from the steady state rp-process calculation of Schatz et al. [129] to calculate electron captures in the outer crust and to update the existing thermal routines with those from Brown [23] (Section 4.1.1).

Initial input to the code is neutron star mass ($1.4 M_{\odot}$) and radius (10 km), initial temperature, mass accretion rate, and initial flux at the top of the crust. The neutron

star is assumed to be accreting steadily. The initial abundance is taken to be pure ^{56}Fe as the ashes from the rp-process. This composition was chosen to make comparisons with the calculations of Haensel & Zdunik [66], though this is not realistic for most hydrogen-burning scenarios. With these input values, an initial density is calculated at a time, $t = 10^7$ s, which corresponds to a column depth of about 9×10^{11} g cm $^{-2}$. The network includes also neutrons and other elements in this $A = 56$ chain, though their initial abundances are set to zero. The elements currently included are: ^{56}Mn , ^{56}Cr , ^{56}V , ^{56}Ti , and ^{56}Sc . This list of nuclei is limited by the reaction rates included in the tables of Fuller, Fowler & Newman [56].

The calculation follows a fluid element down through the crust as it evolves in time under the steady accretion of material. For each timestep, the code calculates the temperature, density, energy, flux, neutrino energy loss, and isotopic abundances as well as the electron abundance. A schematic diagram of the calculational algorithm is shown in Figure 4.4. Throughout a calculational run, the mass fraction X_i is checked at each timestep to ensure that the mass is conserved to a certain fraction: 10^{-7} . If this is not satisfied, the timestep is reduced and the abundance calculation is made again.

The most important part of the algorithm is the calculation of the timestep. The method used here ensures that the timestep will be sufficiently small so that the start of each reaction layer is resolved. A trial timestep, h_{trial} , is taken based on the current reaction rate and abundance change from the previous timestep and is checked to ensure that it has not increased by more than twice the previous step. This is then compared to a test timestep, which is calculated for each isotope from

$$h_{test} = \frac{Y_i}{r_i}, \quad (4.31)$$

where the abundance, Y_i , and the reaction rate, r_i , have been evaluated from the

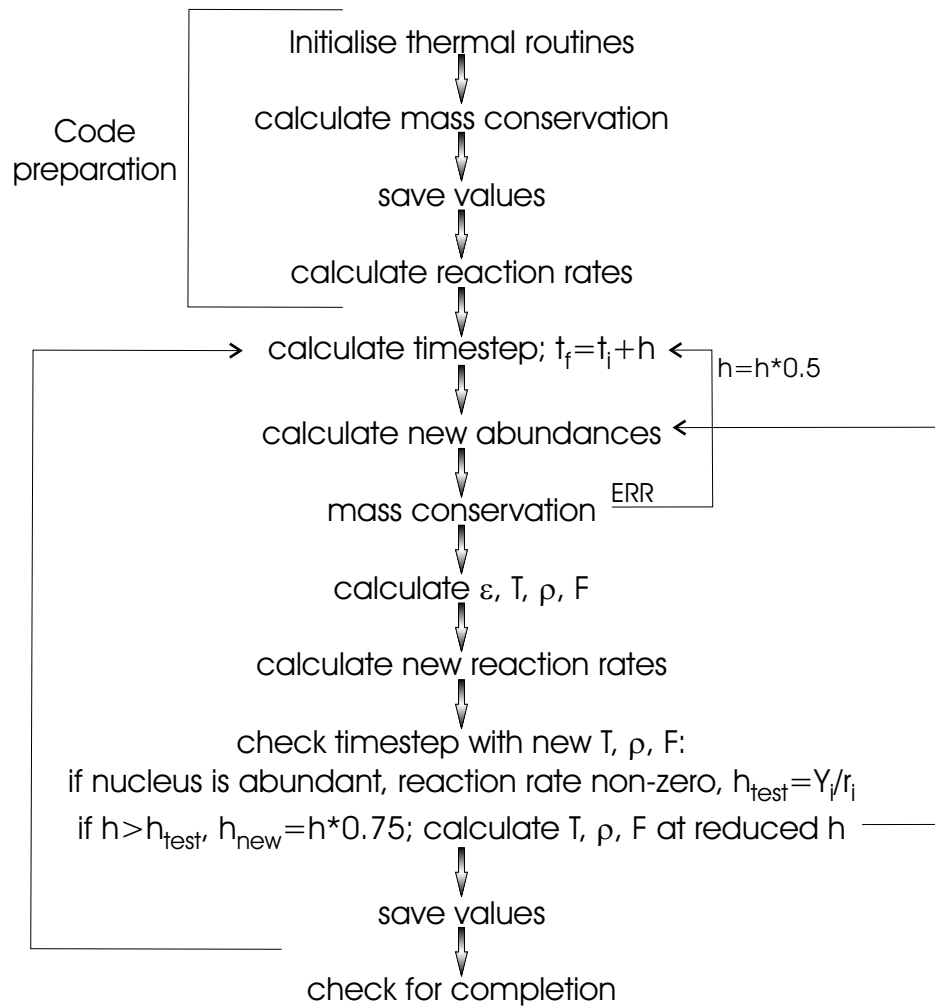


Figure 4.4: Flow chart illustrating the algorithm used in the calculation of electron captures.

temperature and density at h_{trial} . If either $Y_i < 10^{-7}$ or $r_i = 0$, the isotope is ignored. If the test timestep is less than the trial timestep, the timestep is reduced by 30% and all of the variables are recalculated. If this timestep calculation succeeds, the temperature, density, and flux are saved as old values and the process is repeated. The condition for the end of the run is set by a maximum temperature or density: $T_{max} = 10^{10}$ K and $\rho_{max} = 10^{12}$ g cm⁻³.

The thermal routines consisting of Equations (4.6) and (4.7) are integrated using a non-stiff Adams predictor-corrector method included in ODEPACK. Because a trial flux is used, the temperatures calculated could possibly become unreasonably low or even become negative. Thus, a term

$$\frac{1}{2} \left[1 + \tanh \left(\frac{T - T_{min}}{\delta} \right) \right] \quad (4.32)$$

is multiplied to the right hand side of the flux equation (Equation [4.7]). Here, T_{min} and δ are set to $T_{min} = 10^7$ K and $\delta = T_{min}/10$. This term ensures that dT/dt will smoothly decrease to zero for $T < T_{min}$.

The nuclear abundance evolution is calculated from Equation (4.14) through an implicit differencing method [6]. Explicit differencing schemes

$$\frac{1}{\delta t} [Y_i(t + \delta t) - Y_i(t)] = r_i(t) \quad (4.33)$$

are impractical for network calculations since the timesteps required to ensure convergence are unreasonably small. Implicit differencing schemes,

$$\frac{1}{\delta t} [Y_i(t + \delta t) - Y_i(t)] = r_i(t + \delta t), \quad (4.34)$$

allow for larger or adjustable timesteps. This method involves n coupled equations with n unknowns, and can then be solved by linearization. Because the reactions turn

on quickly and abundances may change rapidly in a given timestep, the timestep must be chosen carefully to ensure that abundance changes are small and that mass and energy are conserved.

4.2 Results

4.2.1 The $A = 56$ chain

Implementing the Fuller, Fowler & Newman reaction rates with the calculation of the effective phase space, an initial temperature of 3×10^8 K, and a mass accretion rate of $1 \dot{m}_{\text{Edd}}$ yields the electron capture chain starting at ^{56}Fe , which is plotted in Figure 4.5. The vertical lines show the location of the electron capture layers as calculated by Haensel & Zdunik [66]. The capture layers calculated here agree with naïve predictions given the Q -values from Figure 4.1. The disagreement between these calculations and those of Haensel & Zdunik [66] may occur for a couple of reasons. First, the mass model they use for unknown masses may be different. In addition, they include the energy of the first excited state in ^{56}Mn , changing the Q -value for the electron capture onto ^{56}Fe slightly. Finally, the lattice energy is included explicitly in their calculations, while it is left out of the effective phase space calculation made here. Including the lattice energy would have the effect that an extra amount of energy would be released in the capture reaction. This means that the electron would require less energy, thus capturing sooner.

One important thing to note in Figure 4.5 is that the odd-even nuclei are significantly less abundant than the even-even nuclei. This is simply due to the odd-even effect of the nuclear binding energy and the low Q -value for the electron capture. Although ^{56}Sc has a high abundance, this is misleading: the rates provided by Fuller, Fowler & Newman do not include rates for nuclei past ^{56}Sc , so this is where the reaction chain ends. In this calculation ^{56}Sc cannot burn into anything, so its abundance

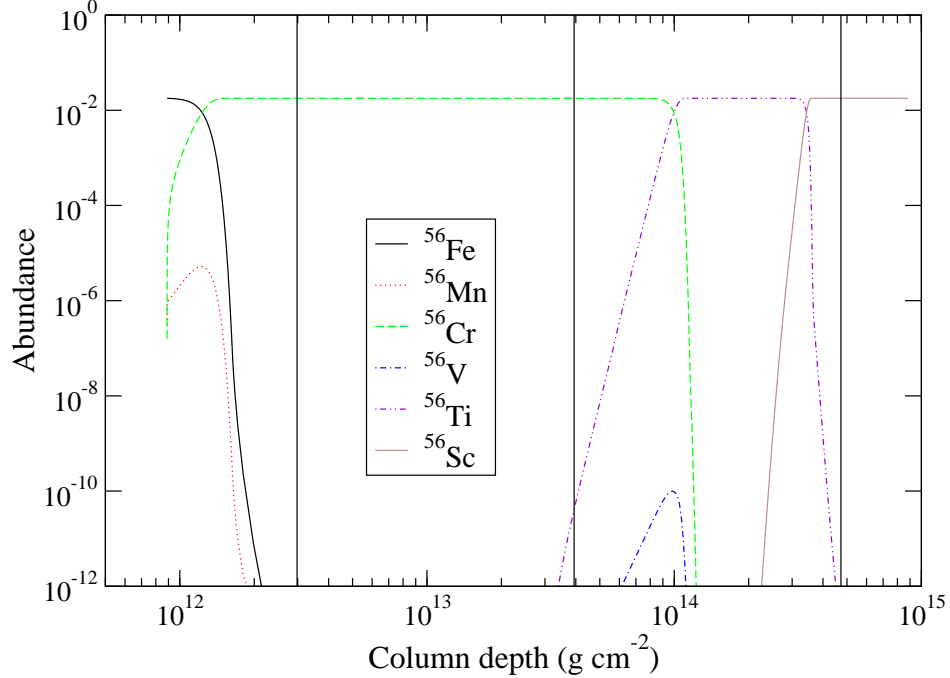


Figure 4.5: Abundance plot for the $A = 56$ electron capture chain. Time increases to the right, so the initial composition is pure ^{56}Fe and the final composition is ^{56}Sc . The vertical lines show the location of the capture layers as calculated by Haensel & Zdunik [66].

remains high.

One major difference from the work of Haensel & Zdunik [66] is that for non-zero temperature, the capture layers have a definite thickness. In their $T = 0$ K approach, the Fermi distribution is very sharp and so the captures happen at a well-defined depth. Because the temperature here is $10^8 - 10^9$ K, the Fermi distribution has a tail through which electron captures may occur, widening the layer, and also shifting the location of the capture. If the thickness of the layers and the composition therein happens to vary over the crust of the neutron star, this could lead to mass-dipole anisotropies and thus, gravitational wave emission [17, 137, 150] for a spinning neutron star.

This calculation differs from the work of Haensel & Zdunik [66] in another way as well. They determined the reaction layer depth solely by examining which nuclear species would minimize the Gibbs energy of the Wigner-Seitz cell at a given pressure.

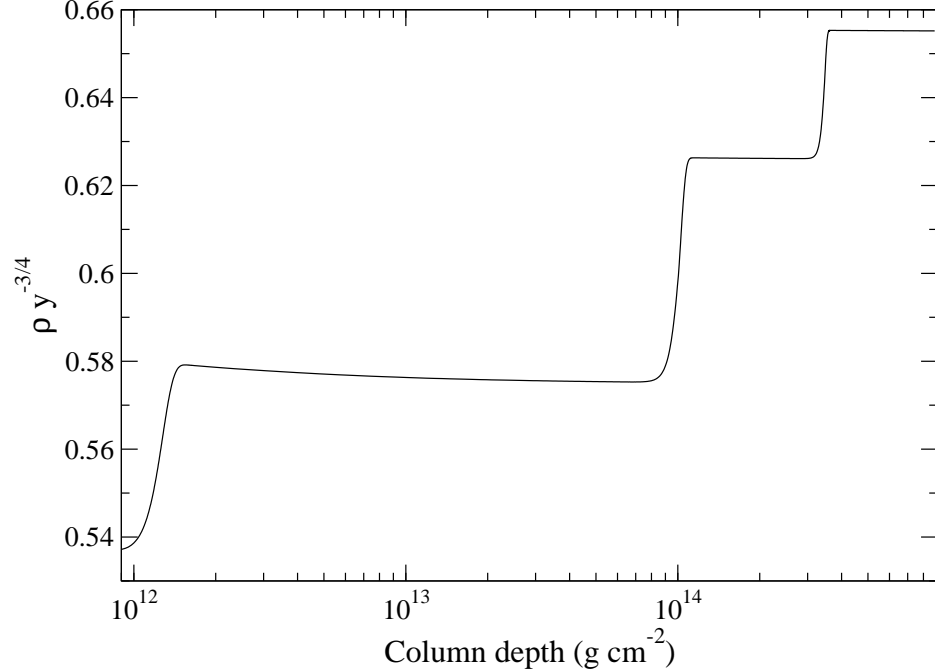


Figure 4.6: Plot of density for the $A = 56$ electron capture chain allowing for a variable temperature. The density jumps at each capture layer are evident.

The calculations presented here implement calculated reaction rates as a function of density and temperature. Although there are problems caused by appropriate interpolation of the rates, this method is likely to give a better estimate of the capture depth since the thermal structure of the star is also taken into account.

The density of matter in the crust changes rapidly at each reaction layer. To first order, the density scales as $y^{3/4}$, where y is the column depth. Plotting $\rho y^{-3/4}$ removes this dependence and shows the density jumps due to the electron captures more clearly. Figure 4.6 shows the density as a function of column depth, and these jumps are evident. The jumps are due to the fact that reactions take place at a constant pressure determined mainly by the electron density, $n_e = Zn$. As the pressure increases, the electron Fermi energy rises until it reaches a point at which the reaction can occur. The capture takes place, and the reduction of Z at each capture layer forces the mass density to increase in order to keep the pressure constant.

Figure 4.7 shows the energy produced at each reaction layer. In the $T = 0$ K

approximation, matter is compressed and the electron Fermi energy rises until it reaches the Q -value of the reaction (Figure 4.1). For the electron capture on ^{56}Fe , as for the capture on any even-even nucleus, the net energy produced in the reaction should be zero since the reaction occurs at the threshold. For the reactions on odd-even nuclei, the Fermi energy is already greater than the Q -value, so there will be energy produced. These calculations are not done in the $T = 0$ K approximation, and so captures are able to take place when the Fermi energy is slightly below the Q -value, thus releasing energy. This energy release can be seen for the capture on ^{56}Sc , since this energy peak is only for the electron capture onto an even-even nucleus. In addition, the captures do not happen instantaneously, so the density changes slightly in the time during which the reactions occur, thus increasing the Fermi energy and releasing more energy than would be expected. Figure 4.7 illustrates that more energy is released for each subsequent reaction layer since $q_n - \mu_F$ becomes larger for each reaction. Comparing this figure with Figure 4.6, it is clear that these energy production regions occur where the density jumps are, and there is no energy production between the layers.

4.2.2 Capture dependences

A study was made of the dependence of the electron captures on temperature. Since these calculations do not make a $T = 0$ K approximation as was assumed by Haensel & Zdunik [66], it is important to understand the differences between the two methods. Only the electron capture on ^{56}Fe was considered in order to keep the study simple. To survey this, the temperature was kept constant during the calculation of an electron capture event, and was chosen to be either 0.0101, 0.101, or 1.01 GK. The extra percent was added to be able to clarify which temperature grid point was chosen for the calculation.

Figures 4.8 and 4.9 illustrate the dependence on temperature for an accretion rate

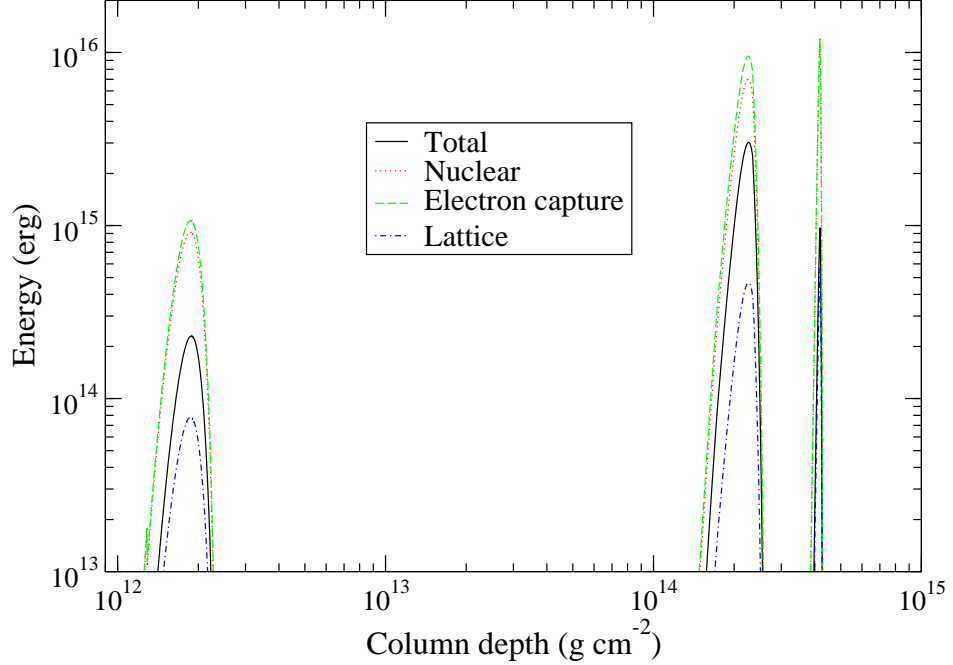


Figure 4.7: Plot of the energy production for the $A = 56$ chain. Note that it is the absolute value of the nuclear energy and lattice energy that is plotted here.

of $1 \dot{m}_{\text{Edd}}$. Note that the change in density becomes smoother as the temperature increases. This steepness represents the thickness of the capture layer. Again, this thickness is due to the ratio of the Fermi energy to the thermal temperature.

As can also be seen in Figures 4.8 and 4.9, the position and thickness of the capture layer is also dependent on the reaction rate. These figures show the density change for temperatures of 0.0101 GK and 0.101 GK for three different reaction rates: the original rate, the rate times ten, and the rate times one hundred. Not only is the density jump steeper for a faster reaction rate, it is clear that the layers are spread out for higher temperatures.

The position of the capture layer for $T = 0.0101$ GK shown in Figure 4.8 is due primarily to the interpolation of the effective rates. Fuller, Fowler & Newman [56] did not calculate the effective rates for those temperatures and densities where the numerical cutoff of the real rate is -99.999 . They suggest that a reasonable extrapolation should be used for these rates. Indeed, when the effective reaction rate

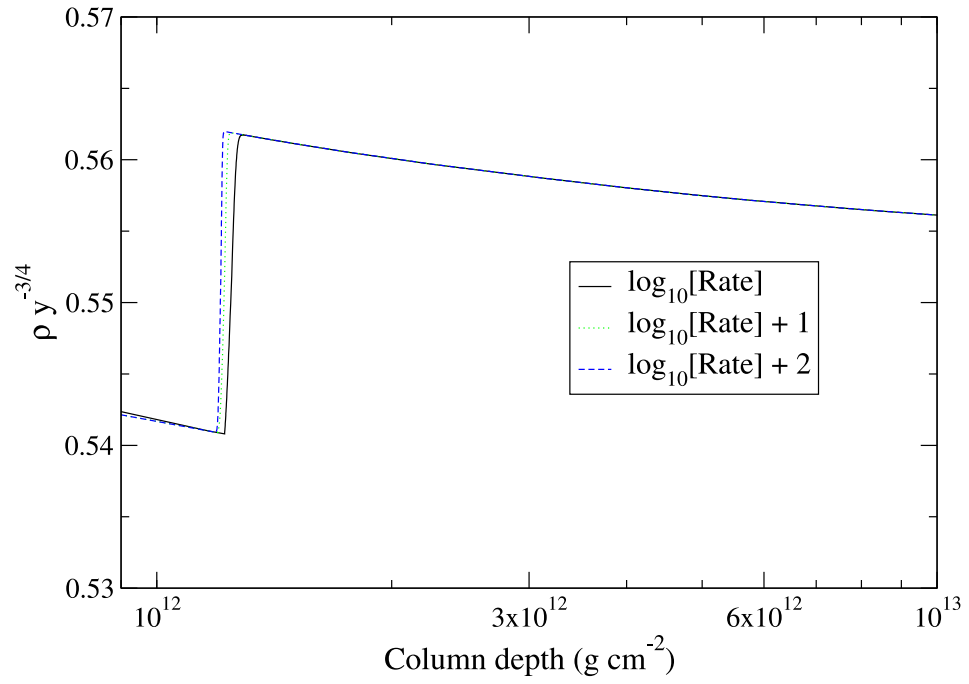


Figure 4.8: Plot of the reaction rate dependence for the electron capture on ^{56}Fe for an accretion rate of $1 \dot{m}_{\text{Edd}}$ and a temperature of 0.0101 GK.

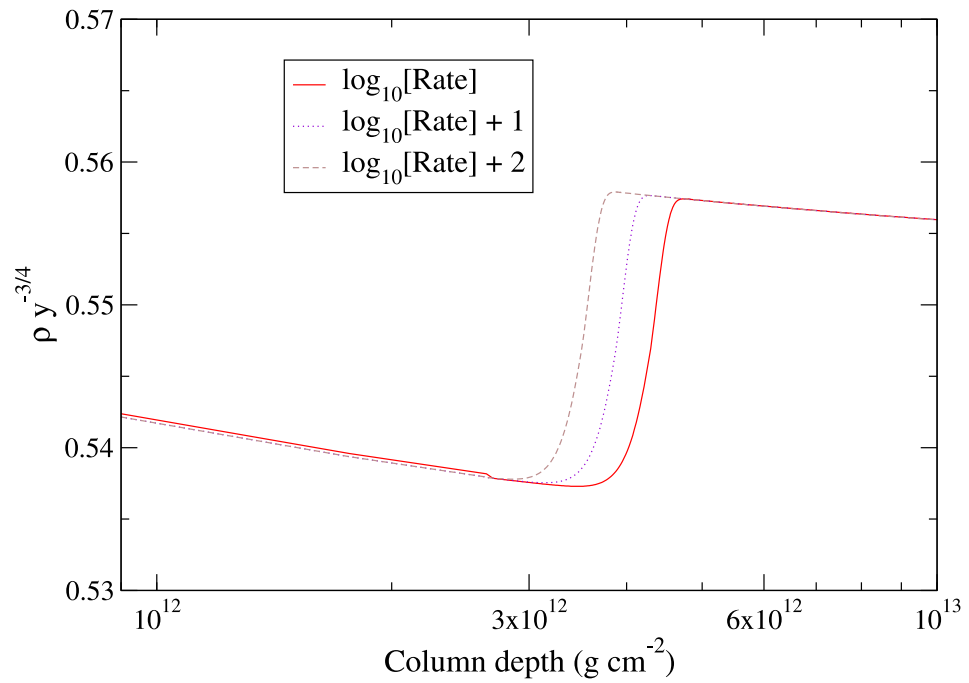


Figure 4.9: Plot of the reaction dependence for the electron capture on ^{56}Fe for an accretion rate of $1 \dot{m}_{\text{Edd}}$ and a temperature of 0.101 GK.

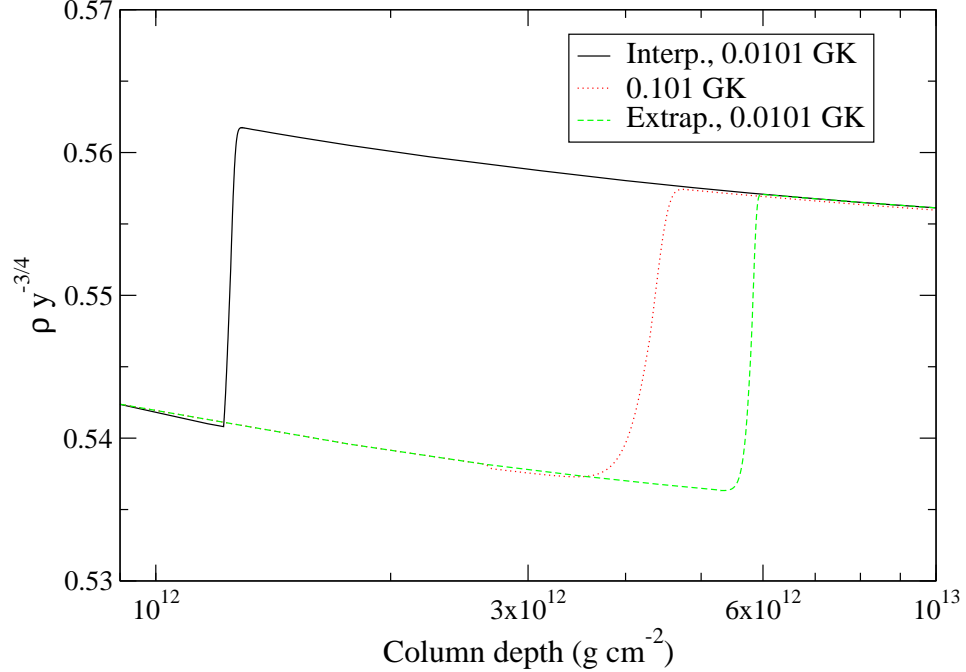


Figure 4.10: Plot of depth of the electron capture ^{56}Fe for an accretion rate of $1 \dot{m}_{\text{Edd}}$ illustrating the dependence on the effective rate calculation. The original curve is shown using an interpolation of the effective rate. The dashed line shows the calculation using an extrapolation of the effective rate. The curve for $T = 0.101$ GK is shown for reference.

at a temperature of 0.0101 GK is extrapolated from a density of 10^9 to 10^8 g cm^{-3} , the layer falls at a depth greater than that for 0.101 GK, as would be expected. Figure 4.10 illustrates the effect of a proper effective rate calculation. The original calculation is shown along with the density curve for a temperature of 0.101 GK. When the effective rate is extrapolated, the reaction layer occurs at the depth expected.

The calculations presented here demonstrate the dependence of the electron capture layer on the temperature and reaction rate. The reaction rate affects primarily the capture layer thickness: for faster rates the reaction layer becomes thinner. The temperature, in contrast has many effects. Higher temperatures mean the electron Fermi energy will be higher at a given depth, thus allowing the captures to occur less deep in the crust. In addition, the temperature smooths out the Fermi distribution, allowing captures into the tail of the energy distribution which widens the capture

layer.

Temperatures in the crust of a neutron star may be between $10^7 - 10^9$ K, depending on the composition and the mass accretion rate. For electron capture on ^{56}Fe , according to these calculations, this temperature difference means layers can occur at depths between $10^{12} - 6 \times 10^{12}$ g cm $^{-2}$. While this difference is not insubstantial, it is doubtful that it would be observable. In the lightcurves of cooling neutron star transients it has been shown that heat from the individual capture layers is smeared together before reaching the neutron star surface. Because of this, it is not possible to tell at which depth a given electron capture occurs. However, the difference in depth could affect gravitational wave emission, which, with sensitive enough measurements, would yield information about the crust temperature of the neutron star if the composition structure were known.

4.3 Summary and future prospects

This work has calculated electron captures for the non-zero temperature neutron star crust by implementing the reaction rates calculated by Fuller, Fowler & Newman [53]. The electron capture chain proceeding from ^{56}Fe was calculated as an example. It was also shown that electron capture reactions calculated in conjunction with a thermal model are quite different than reactions calculated in the $T = 0$ K approximation. The non-zero temperature means that the reaction layers have a finite thickness and occur at a depth inversely proportional to the temperature. The reaction layers are also dependent on the reaction rate, which serves to thicken the reaction layer, and the calculation of the effective phase space.

Much work needs to be done to make the electron capture calculations useful for neutron star crust studies such as that explained in Chapter 3. First, the reaction rate table needs to be expanded to include more nuclei, since the current table contains

electron capture rates only for stable nuclei of $21 \leq A \leq 60$. Calculations of the rp-process indicate that the ashes that would form the initial composition for the electron capture calculations are composed of a range of nuclei up to $A = 106$, extending far beyond the current available rates. In addition, the table should also be expanded to higher densities. Second, a calculation must be implemented so that the energy of the mother and daughter excited states are included in the nuclear Q -values used in the effective rate calculations. Third, the calculation of the effective phase space should be modified to take into account the cutoff values of the reaction rate when the rate is very slow. Finally, calculations of the neutron emission and pycnonuclear reaction rates need to be implemented, along with an extension of these rates to higher densities.

The first three modifications will be taken into account in a new calculation being made by Sanjib Gupta. This is an analytical calculation of the effective phase space and as such will be applicable for any temperature and density. Besides removing the need for an expansion of the rate table, it will also eliminate the problems related to the interpolation between points, which will automatically take into account the phase space. Furthermore, $\log(ft)$ values of daughter excited states have been computed by Peter Möller for use in these calculations. They will also be implemented in the work of Sanjib Gupta.

The calculation of the pycnonuclear reaction rates are being led by Michael Wiescher. These fusion reactions occur deep in the crust (see Table 3.2) at extreme densities and the calculations need to include nuclear masses far from stability. Currently the equation of state of Mackie & Baym [96] is used for densities at the inner crust. Because the type of matter present at this depth is uncertain, it would be desirable to find an accurate equation of state at these densities. In particular, it should take into account the neutron gas surrounding the nuclei.

Finally, to be of use for astrophysical calculations, a full series of electron cap-

ture calculations should be run with a realistic initial abundance distribution. These abundances can be produced from steady-state calculations by Schatz et al. [129] or from multi-zone models [165] of X-ray bursts.

Chapter 5

Time-of-flight Detectors

Because many of the nuclei in the deep crust of the neutron star are very neutron rich, few experimental measurements of these nuclei have been made. Thus, astrophysical calculations must rely on theoretical models for nuclear data input. However, several properties of these nuclei can be measured with radioactive beams, such as the neutron separation energy, half-life, and mass. Most important for electron capture rate calculations are the masses of these nuclei. To this end, a parallel-plate avalanche counter (PPAC) has been developed for use in mass measurement experiments in conjunction with the S800 magnetic spectrograph at MSU. A similar technique has been employed successfully at GANIL with the SPEG spectrometer for nuclei on both sides of the valley of β -stability [32, 60, 61, 112, 125]. This experiment will mark the first measurement of ^{70}Fe .

5.1 Time-of-flight measurements

A straightforward way to measure masses of isotopes is to use a spectrograph (Figure 5.2) in conjunction with two timing detectors. The equation of motion of a particle

in a magnetic field is given by

$$m \frac{d\mathbf{v}}{dt} = q\mathbf{v} \times \mathbf{B}, \quad (5.1)$$

where m and \mathbf{v} are the mass and velocity of the particle; q is the particle's charge and \mathbf{B} is the magnetic field strength. Including the relativistic factor $\beta = v/c$ and rearranging, this formula may be written as

$$B\rho = \frac{m_0 c^2}{Ze} \frac{\beta}{\sqrt{1 - \beta^2}}, \quad (5.2)$$

where the properties of the spectrograph are on the left and the properties of the particle are on the right. Here, ρ is the radius of the particle's path in the magnetic field, Ze is the charge of the particle, and the quantity $B\rho$ is known as the *magnetic rigidity*.

To measure the mass of a particle, one must know $B\rho$, Ze , and v . A position measurement in the dispersive focal plane of the spectrograph determines $B\rho$, and Ze is determined by an energy loss measurement. To measure the velocity, $v = L/T_f$, two detectors are placed in the beamline, a given distance, L , apart, and the time it takes for the particle to traverse this distance, T_f , is measured. Equation (5.2) can then be expressed as

$$\frac{m_0 c^2}{\sqrt{1 - \beta^2}} = \frac{ZeB\rho}{L} T_f, \quad (5.3)$$

where $\beta = v/c$, containing another factor of T_f .

5.2 Measuring the mass of ^{70}Fe

An experiment has been proposed and approved at the NSCL to measure the masses of short-lived neutron-rich isotopes near the $N = 50$ shell closure through such a time-of-flight method. The experiment will utilize the A1900 – S800 beam line system (Figure

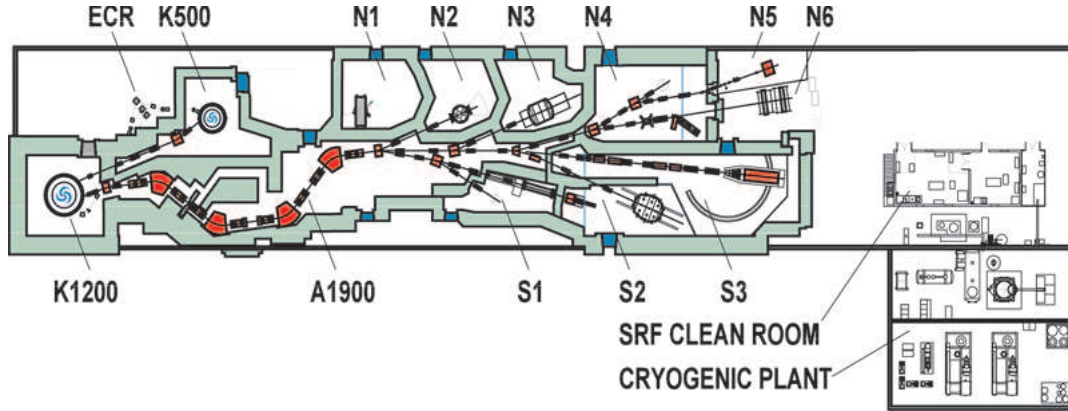


Figure 5.1: A map of the coupled cyclotron facility at the NSCL. The K500 and K1200 cyclotrons and the A1900 are illustrated. The S800 spectrograph is located in the S3 vault.

5.1) along with a rigidity measurement in the S800. In a single production setting, the masses of a number of neutron-rich Fe, Ni, and Co isotopes will be measured.

A 100 MeV/u⁸⁶Kr primary beam produced in the coupled cyclotrons (Figure 5.1) will be incident on a 376 mg cm⁻² Be target, and the A1900 fragment separator will be set to select either ⁶⁶Fe or ⁷⁰Fe fragments. Produced along with the ⁶⁶Fe fragments in a cocktail beam will be a number of previously measured isotopes to be measured again for calibration purposes. Table 5.1 lists nuclei that can be measured in either setting. According to LISE [13] calculations, the ⁷⁰Fe fragment with an energy of 71 MeV/u out of the A1900 will have a 680 ns time of flight.

One timing PPAC will be placed in the intermediate image chamber of the A1900 (Figure 5.1) to mark the start time. The other will mark a stop time 78 meters down the beamline in the focal plane of the S800 (Figure 5.2). The S800 is a high-resolution, high-acceptance spectrograph designed especially for radioactive beam experiments [14]. To determine $B\rho$ in Equation (5.3), position and angle information in the S800 focal plane [171] is given by a pair of cathode readout drift counters (CRDCs) separated by one meter. These detectors are filled with a mixture of 80% CF₄ and 20% C₄H₁₀ at a pressure of 50 Torr, and have an active area of 56 cm by 26 cm in the dispersive and non-dispersive direction, respectively. An ionization chamber

Table 5.1: Production rates calculated with LISE for nuclei of interest for the ^{66}Fe and ^{70}Fe settings as well as lighter calibration nuclei. 20 additional unknown masses are not listed. 50% losses due to transmission through the S800 are taken into account. Boldface nuclei indicate r-process waiting points. Experimental mass excesses are taken from Audi et al. [7].

Isotope	Rate (s^{-1}) (^{66}Fe)	TOF (ns) (^{66}Fe)	Rate (s^{-1}) (^{70}Fe)	TOF (ns) (^{70}Fe)	Mass Excess (keV)
^{47}Ar	0.013	694.050			-29780.739 \pm 40.898
^{48}K	0.108	674.721			-32124.479 \pm 24.117
^{49}K	0.195	686.692			-30320.147 \pm 70.124
^{50}Ca	1.75	668.691			-39571.456 \pm 9.297
^{51}Ca	1.9	680.068			-35886.511 \pm 90.963
^{56}V	70.	653.955			-52914.442 \pm 272.520
^{57}V	110.	663.787			-52914.442 \pm 272.520
^{58}V	35.	673.668	0.01	642.495	-52914.442 \pm 272.520
^{59}V	4.85	683.560	0.275	651.761	-52914.442 \pm 272.520
^{60}V	0.355	693.501	0.39	661.077	-52914.442 \pm 272.520
^{60}Mn	1.8	646.101			-52914.442 \pm 272.520
^{61}Mn	60.	655.117			-51735.169 \pm 260.818
^{62}Mn	130.	664.178			-48465.626 \pm 260.818
^{63}Mn	47.	673.247			-46751.677 \pm 279.448
^{64}Mn	8.	683.356	0.095	650.634	-43100.221 \pm 326.023
^{65}Mn	0.75	691.473	0.37	659.176	-40892.588 \pm 558.896
^{65}Fe	100.	668.693			-51288.052 \pm 279.448
^{66}Fe	29.5	677.416			-50319.298 \pm 326.023
^{67}Fe	3.8	686.185	0.09	654.222	-46574.693 \pm 465.747
^{68}Fe	0.235	694.961	0.3	662.445	
^{69}Fe	0.0115	703.778	0.12	670.709	
^{70}Fe			0.0225	679.016	
^{67}Co	135.	664.486			-55321.420 \pm 279.448
^{68}Co	70.	672.899			-51828.318 \pm 326.023
^{69}Co	15.5	681.307			-51045.864 \pm 372.598
^{70}Co	1.75	689.764	0.08	657.575	
^{71}Co	0.09	698.217	0.3	665.496	
^{72}Co			0.095	673.457	
^{73}Co			0.019	681.494	
^{70}Ni	120.	668.656			-59485.198 \pm 326.023
^{71}Ni	55.	676.779			-55889.632 \pm 372.598
^{72}Ni	11.	684.897			-54678.690 \pm 465.747
^{73}Ni	1.	693.061	0.115	660.665	
^{74}Ni	0.055	701.217	0.31	668.309	
^{75}Ni			0.095	675.994	
^{76}Ni			0.018	683.673	

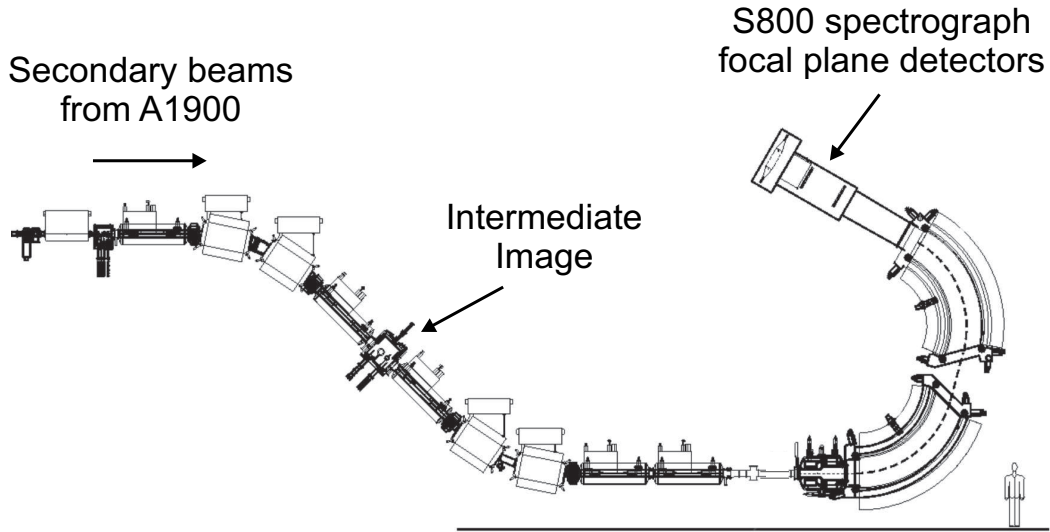


Figure 5.2: Diagram of the S800 spectrograph at MSU.

is located beyond the CRDCs and measures the energy loss of the ions. It is filled with P10 gas, a mixture of 90% argon and 10% methane, at a pressure of 300 Torr. Finally, a series of three plastic scintillators 5, 10, and 20 cm thick measure the energy loss and total energy of the ions. The amount of light sent by the scintillators to a pair of attached photo-multiplier tubes (PMTs) is a function of the atomic number, mass number, and energy of the ions. This provides Ze in Equation (5.3).

To minimize systematic errors, a careful calibration will be made using nuclei with well-known masses. To test the method, a ^{66}Fe setting will provide good statistics for a large number of isotopes with measured masses ranging from Ca to Ni. The ^{70}Fe setting will then be used to measure new masses in the Fe – Ni region. This setting provides a mix of unknown nuclei along with a number of calibration nuclei. The overlap of nuclei allows for consistency checks between the two settings.

5.3 Timing detectors

In order to measure the time of flight to high precision, two PPACs [71, 95, 136, 140] were built (Figure 5.3). PPACs are composed of thin foils separated by 1 or 2 mm



Figure 5.3: Photograph of one timing PPAC. The left panel shows the detector as it is used in the experiment, showing a pressure window. The right panel shows the inside of the detector with the stack of G10 boards.

of an organic gas. As electron-ion pairs are created in the gas chamber, the electrons drift toward an anode and produce secondary ion pairs, all of which are then detected. PPACs are commonly used at the NSCL and other accelerator facilities for position and timing measurements since there is little material within the detector, reducing the energy loss of the particles. The detectors discussed here are designed to make timing measurements only. Each detector consists of a stack of eight 2 mm thick chambers formed by two aluminized mylar sheets stretched on G10 boards and filled with isobutane gas. The motivation for the stack of eight chambers is to make eight time measurements of each particle at both the start and stop locations. In this way, the statistics are greatly increased with the same beam and experimental setup. The stack of chambers is housed in a steel box with pressure windows aligned with the mylar foils. The effective area of each detector is 100 cm^2 . As can be seen in Figure 5.4, the five holes in the G10 board above the foils allow for the flow of isobutane between the foils.

Construction of the detectors is done by cementing a sheet of mylar to the G10 board such that the sheet touches the silver contact on the board. Another board is

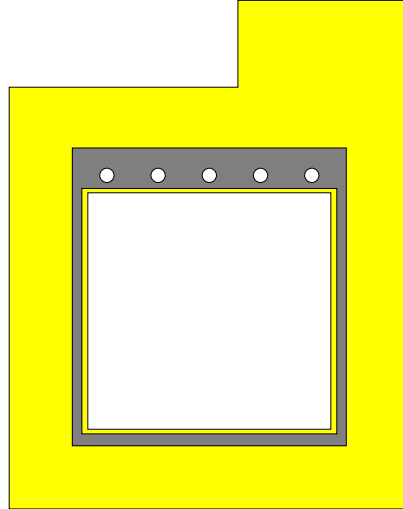


Figure 5.4: Diagram showing a G10 board used in the timing detector. The dark gray area represents the silver contact.

then placed against the first board so that its silver contact also touches the mylar and the five gas holes line up. This forms one cathode, and the seven other cathodes and eight anodes are formed in the same manner. Cathodes and anodes are then alternated, with the gas holes at one end for the cathodes and at the other end for the anodes. Gas is free to flow throughout the interior of the box.

The electronics on each board consist of a $50\ \Omega$ resistor and a $0.010\ \mu\text{F}$ capacitor serving as a high-pass filter. With this combination, one obtains 500 ns differentiation. The signal rise time is much shorter than this, but a relatively long differentiation time is chosen to improve the spark resistance. A high voltage cable connects the cathodes in series and the anodes are grounded to the steel container (Figure 5.3). There are two large feed-throughs for the gas: one input and one outflow. The BNC connector is for the high voltage cable, and the eight LEMO connectors are for each of the eight channels in the detector.

Isobutane was chosen to be used in the detectors for a number of reasons. Primarily, it is an organic gas which is readily available with a high purity. Trimethylpentane would work as well, but it is difficult to get enough high-purity gas for use in these detectors. Finally, CF_4 could be used, but this is not ideal for several reasons. It

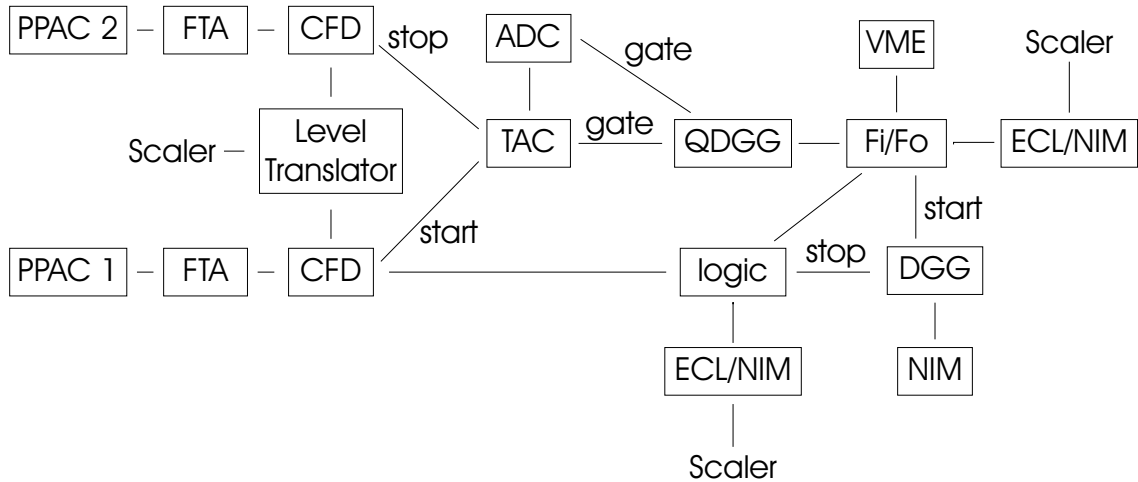


Figure 5.5: Diagram showing the electronic circuitry for PPAC timing measurements. The TAC start signals go through a 150 ns delay and the TAC stop signals go through a 200 ns delay.

has a higher stopping power than isobutane at the same pressure so it has a higher ionization potential. Thus, there is not a large gain in signal height for the amount of energy that is lost by the particle through detection. Finally, CF_4 etches away the aluminum on the anodes and cathodes more quickly than isobutane.

5.3.1 Electronics

The basic electronics setup for tests of the detectors is shown in Figure 5.5. A signal from each segment of each PPAC is sent to an Ortec 820 fast timing amplifier (FTA) and then to a Tennelec 455 constant fraction discriminator (CFD) with a 10 ns delay. The signal from channel one of PPAC 1 acts as the master gate, going through a gate and delay generator and then into an Ortec AD413A analog to digital converter (ADC). Signals from PPAC 1 are the start signals and signals from PPAC 2 are the stops. One start and one stop signal are delayed by different amounts and then fed into a time-to-amplitude converter (TAC), whose output is connected to the ADC.

The TACs were set to the best available time range at 200 ns for all electronics and detector tests. The desired time range would be 250 ns to include all nuclei in

the multi-species, or *cocktail*, beam, though a range of 200 ns only eliminates three or four of the lightest nuclei from the spectrum. The ADC has a resolution given by Δ_{tof}/N , where N is the number of channels and Δ_{tof} is the spread in times of flight for different nuclei. The Ortec AD413A has 8064 channels, resulting in a resolution of 24 ps per channel. With this time range, the expected resolution of 150 ps per timing peak means the full-width at half-maximum (FWHM) would span 6 channels, which is a reasonable width for fitting with Gaussian curves.

As a check of the electronics setup, a pulser signal was split and sent through the electronics using various TAC ranges. A clean spectrum resulted, showing peaks with a FWHM of 1 – 2 channels. This test demonstrates that the resolution of the electronics is better than 24 ps.

5.3.2 Detector tests

A number of tests were made with the detectors in order to determine the best settings for pressure and bias voltage for use in the experiment. In addition, the electronics were tested further to optimize the CFD delay cable length and constant fraction.

Preliminary tests were made with a ^{228}Th α -source in the intermediate image chamber of the S800 (Figure 5.2). An existing gas-handling system provided isobutane to the detectors. A very stable setting was found at a pressure of 6.0 Torr and 585 V, yielding a signal rise time of 4 ns. With the source in place, α -particles penetrated only the first three or four chambers of the detector, leading to a weaker signal in each succeeding chamber. Using neighboring chambers in one detector, signals were sent through the electronics to obtain a timing spectrum. The average FWHM of a spectral peak was 100 channels, corresponding to a timing resolution of 2.5 ns. Tests made with ^{86}Kr and ^{36}Ar beams improved the resolution slightly to 1.25 ns.

Further tests were made in an isolated vacuum chamber to reduce outside effects that may result from electronic or vibrational noise. The mylar foils of one detector

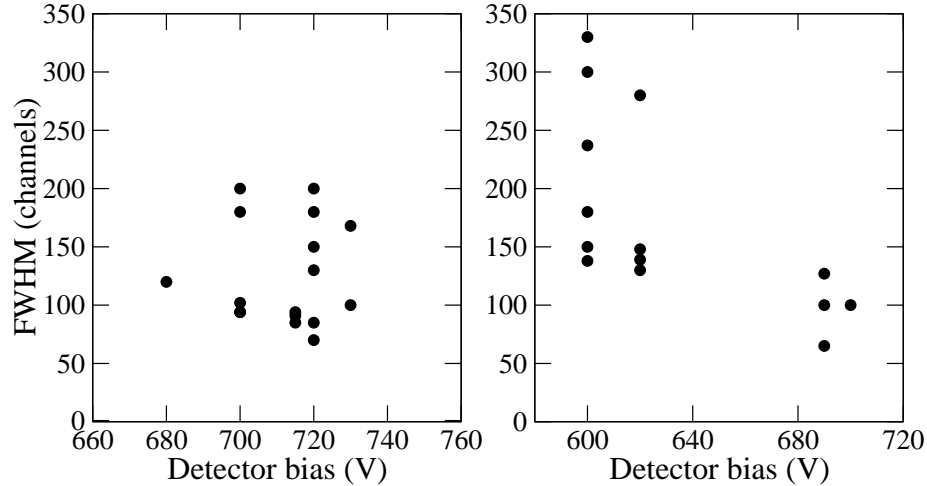


Figure 5.6: Plot of the FWHM (24 ps/channel) as a function of bias voltage with the collimator in place (left panel) and with no collimator (right panel). The left panel shows measurements at 9.0 Torr with varying CFD delay cable lengths. The right panel shows measurements at 7.0 Torr for the low biases and 9.0 Torr at the high biases with various CFD delay cable lengths.

were replaced with 9 μm aluminum foils, as the aluminum was expected to be more resistant to sparks than the mylar. In addition, as the particles deposit more energy in aluminum than in mylar, it was suspected that this would increase the pulse height, whereby increasing the timing resolution. However, the α -particles were not energetic enough to penetrate a chamber. In subsequent beam tests no signals were detected in this PPAC since the breakdown threshold was very low.

Figure 5.6 shows the FWHM as a function of bias voltage in the presence of a collimator and with no collimator in place. Pressure, CFD delay cable length, and the CFD threshold were varied for these measurements. In general, the FWHM improves with increasing delay cable length and increasing CFD threshold. With a collimator in place it is clear that a better spectrum resolution is obtained since the collimator reduces the angular spread of particles passing through the detector. However, a higher bias is necessary to detect enough particles in a reasonable length of time. From this data, the setup without the collimator yielding the best spectrum resolution was obtained with a pressure of 9.0 Torr and a bias of 690 V.

With this pressure and bias, the CFD was set with a threshold of 1000 mV, which is rather high, limiting the number of detections. The delay cable length used was 10 ns. The CFD settings determine how the signal will be interpreted by the electronics system. It is necessary to have a delay cable longer than the rise time, and delay cables much longer than this serve to damp out differences in rise times from various signals. The constant fraction in the CFD is also a variable, and though a fraction of 40% with a delay cable comparable to the rise time would seem best, the signals are unstable enough that better results are obtained with a fraction of 20% and a longer delay cable. The resulting timing spectrum is shown in Figure 5.7. The primary peak can be fit well with a Gaussian curve, illustrating that the detector behaves as expected.

One final beam test was made in the 92-inch chamber in the N3 vault (Figure 5.1) with a 140 MeV/u ^{48}Ca beam using these optimal settings; however, no improvements could be made on the resolution. Since the gas-handling system was different for each testing location, there was little consistency between pressure measurements in each setup. This, in turn, affected the optimal voltage; using a voltage that is too high induces sparking between foils. The breakdown of PPACs due to various reasons has been discussed by Fonte et al. [50]. Despite this, the major cause of the poor resolution is thought to be from cross-talk between chambers, leading to variations in the signal rise time. As can be seen in Figure 5.7, the variations in rise time not only broaden the timing peak, but also create a secondary, smaller peak. Further improvements are needed to get a desired time resolution of less than 500 ps.

5.3.3 Sources of error

To measure the time of flight with high accuracy, two items must be taken into account: the resolution of an individual detector, and the number of measurements that will be made in each detector.

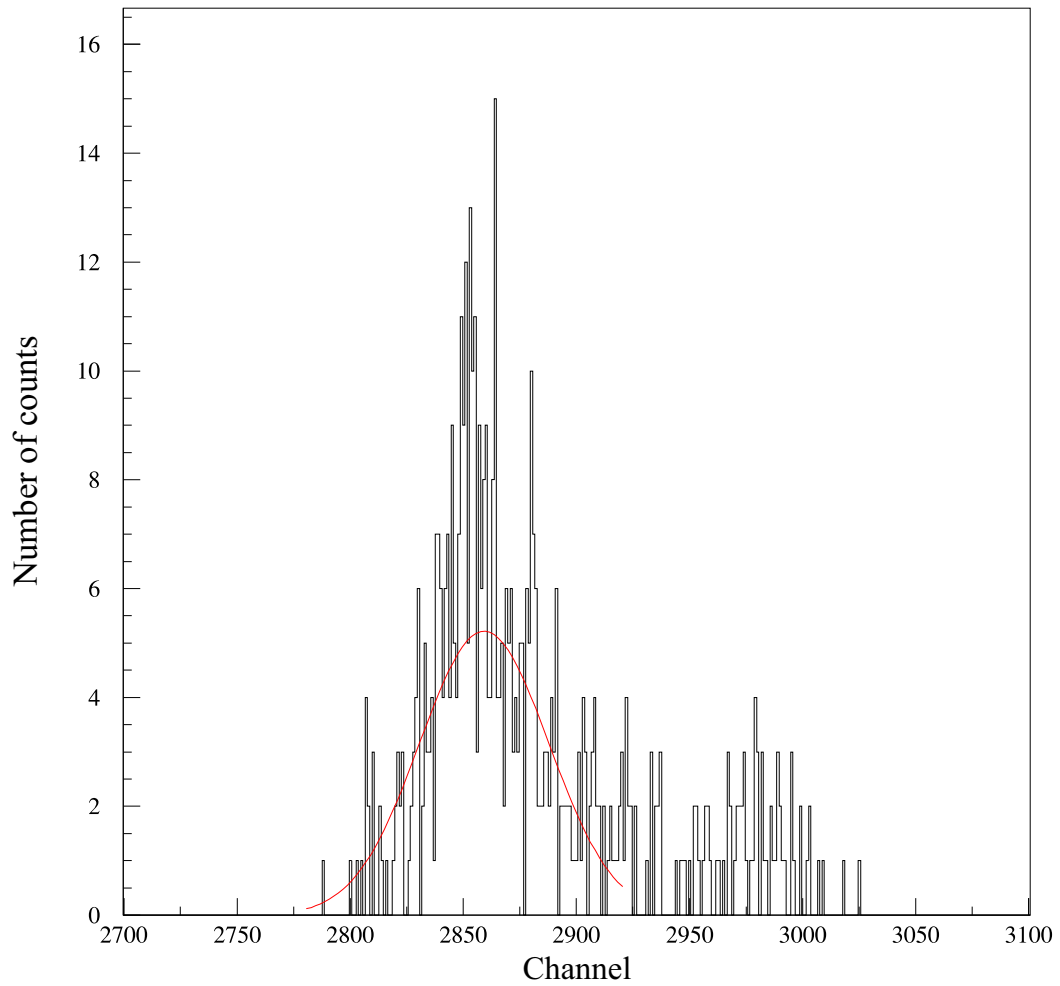


Figure 5.7: Timing spectrum obtained from the optimum setup during detector testing. The spectrum has been fit with a Gaussian between channels 2780 and 2920, which does not include the data to the right of the primary peak. The FWHM = 67.

The electronic timing resolution of one PPAC chamber in the timing detector can be estimated using

$$\text{resolution} \simeq \frac{\text{noise level}}{\text{pulse height}} \times \text{rise time.} \quad (5.4)$$

The noise from a single PPAC channel is typically ~ 10 mV and the rise time is approximately 4 ns. At a pressure of 6.0 Torr and a voltage of 585 V the pulse height is ~ 300 mV, yielding a timing resolution of 130 ps for one PPAC. However, various sources of uncertainty serve to worsen the resolution. Sources of uncertainty include the TAC/ADC combination, non-planar geometries in the detector, the location of ionization in each chamber, and variations of the signal for each detection.

Based on previous studies of PPACs, the goal was to build a timing PPAC that would have a resolution of 300 ps, yielding a measurement in the stack of 8 PPACs with a resolution of 106 ps. Given that there are two PPACs per timing measurement, the total timing resolution would be 150 ps. Error in the spectrum due to the electronics must be accounted for also. This uncertainty, due mostly to the TACs, is 55 ps, which therefore does not significantly contribute to the error for one timing measurement. Comparing this to the timing error from the PPACs alone, it is clear that the PPAC timing uncertainty is the limiting factor. The resolution for a timing measurement of a 700 ns average time of flight would therefore be 2.1×10^{-4} .

The accuracy constraints in the measurement of the mass are the magnetic rigidity and the time of flight. These uncertainties are combined quadratically to give the error in mass:

$$\left(\frac{\delta m}{m}\right)^2 = \left(\frac{\delta T_f}{T_f}\right)^2 + \left(\frac{\delta B\rho}{B\rho}\right)^2. \quad (5.5)$$

The resolution of $B\rho$ for the S800 is 2×10^{-4} , so the total mass resolution would be 2.4×10^{-4} . To be useful in astrophysical calculations, masses are needed with an uncertainty of about kT , or 100 – 200 keV for astrophysical temperatures. Measuring the mass to within 200 keV for an $A = 70$ nucleus necessitates an accuracy of 3×10^{-6} ,

which, for $T_f = 700$ ns, corresponds to a timing measurement with 2 ps error. To obtain this mass accuracy with a mass resolution of 2.4×10^{-4} , about 6200 events need to be measured. For the primary nucleus of interest, ^{70}Fe , LISE calculations predict 7800 counts in the 96 hours of allotted beam time.

5.4 Outlook

Although it is unclear why the detectors did not perform as well as expected, the design and use of such detectors seems promising. Because very little energy is lost through detection in these PPACs, the particles retain much of their energy upon detection in the S800, making for clean measurements. Additional work needs to be done to improve the resolution of the PPACs before useful mass measurements of 200 keV accuracy may be made.

One option would be to reduce the effective area of the detector. This would serve to reduce the capacitance of the detector and give a larger signal height. However, the PPAC effective area is the same as for standard position PPACs and the resolution is more likely due to variations in the rise time due to cross-talk between the various segments. Another possibility is to increase the distance between the foils in the detector. This would increase the mean free path of the particles, therefore increasing the electron statistics in the detector, though more energy would be lost.

An additional proposal to make these mass measurements is to use one PPAC timing detector in conjunction with a fast scintillator [107], or to use two scintillators without timing PPACs. These scintillators are constructed of C_9H_{10} at a density of 1.032 mg cm^{-3} with a thickness of 0.2 mm, and it has been shown that timing resolutions on the order of 20 ps can be achieved for heavy ion beams. Because the plastic can be kept thin, little energy is lost in detection. However, with such a setup, the eight-fold measurement advantage is lost.

Chapter 6

Conclusion

The work presented here links the four areas of nuclear astrophysics: observational astronomy, theoretical astrophysics, theoretical nuclear physics, and experimental nuclear physics. The integration of work in these fields leads to the understanding of physics in dense stellar conditions such as neutron stars.

First, this work combined theoretical astrophysics and observational astronomy by presenting a theoretical calculation made to follow the thermal evolution of a transient neutron star over a series of outbursts and quiescent periods. The results of this calculation were compared with two transient neutron stars: KS 1731-260 and MXB 1659-298. Agreement between calculations and observations is good for the case of KS 1731-260, indicating a high-conductivity crust and enhanced core neutrino cooling. Comparison of observations and calculations indicate the same for MXB 1659-298, though more work is necessary before the thermal evolution of MXB 1659-298 can be understood, as the calculations under-predict the observed quiescent luminosity. While constraints may still be made on the interior physics of these neutron stars, such as the conductivity of the crust and the material at the center of the star, more observations are necessary to better map out the actual cooling curves for better comparison with the calculations. Moreover, the outburst recurrence time of KS 1731-

260 cannot be constrained due to the high-conductivity crust and its low luminosity in quiescence. The calculation of KS 1731-260 also allowed for a determination of the depth of ^{12}C ignition in the neutron star crust, giving a recurrence time of 95 yr for the model which best agrees with observations. This recurrence time is much longer than the outburst length of the source, and is also much longer than the recurrence time inferred from the energetics. Many more studies are necessary to reconcile this discrepancy.

To aid in interpreting past and future observations of quiescent neutron stars which have undergone long outbursts, the cooling code was used to make a parameter study of neutron stars cooling into quiescence. This survey shows how the cooling curves change with respect to outburst length, recurrence time, and mass accretion rate. It was found that the outburst length and accretion rate determine how much heat is deposited in the crust over an outburst, and the recurrence time affects the amount of heat lost during quiescence. The thermal conductivity and neutrino emission from the star were also varied. It was shown that stars with a high-conductivity crust are much less luminous at $t = 1$ yr after the outburst than stars with low-conductivity crusts. It was also shown that stars with enhanced neutrino emission in the core cooled down to a lower quiescent luminosity than stars with standard neutrino cooling, though a distinction between cooling models is only manifested in the high-conductivity case. In particular, sources with quiescent luminosities less than 3×10^{32} erg s $^{-1}$ at one year after the outburst indicate high-conductivity crusts, and sources with quiescent luminosities greater than 5×10^{33} erg s $^{-1}$ at one year after the outburst indicate low-conductivity crusts. Finally, the outburst recurrence time for the high-conductivity/enhanced cooling case is unconstrained for an outburst length of 12 yr, such as in the case of KS 1731-260.

Second, the primary factors in determining how much heat is deposited in the star are the position and energetics of the electron capture and pycnonuclear reactions

in the crust. Building on previous calculations of electron capture reaction rates, a calculation was made which aimed to compute the depth and energy output of electron captures for astrophysical temperatures, as well as provide the thickness of the burning layers. The depth and thickness of these layers were found to be dependent on the temperature at the location of the capture layer, the reaction rate, and the reaction Q -value, which should include the energies of excited states in the parent and daughter nuclei. Because the dependence of the reaction rates on temperature and density is so steep, an accurate interpolation of the reaction rate grid is necessary, and the removal of the effective phase space from the reaction rate is an important factor in properly determining the rate. It was discovered, however, that the effective phase space calculation was not suitable for the calculations done here, so additional work is needed before these nuclear reaction rates may be used in astrophysical calculations.

Finally, the major uncertainty in such reaction rate calculations is the nuclear physics. Experiments to measure the level structure of nuclei as well as their masses provide empirical input for the calculations. With this in mind, a pair of stacked parallel-plate avalanche counters for use in mass measurement experiments were designed, built, and tested. However, it was found that the resolution of these detectors in their current design is not suitable for use in mass measurements requiring a high time precision.

Appendix A

Outer boundary condition derivation

The steady burning of hydrogen sets a temperature of $T_0 = 2.5 \times 10^8$ K at a column depth of $y_0 = 10^8$ g·cm⁻² [43]. In plane-parallel coordinates, the flux is given by Equation 3.2. The conductivity (Equation 3.15) can be approximated by

$$K \sim C_1 \frac{T n_e p^2}{m_e n}, \quad (\text{A.1})$$

where n is the number density of nuclei and C_1 contains the remaining constant factors. The number density of electrons goes as the mass density, which is proportional to $P^{3/4}$. With this substitution, the conductivity can be expressed as

$$K \sim C_2 \rho^{1/3} T, \quad (\text{A.2})$$

with C_2 different from C_1 .

The flux may then be written as

$$F = C_2 \rho^{4/3} T \frac{dT}{dy}. \quad (\text{A.3})$$

Because the column depth $y \sim P \sim \rho^{4/3}$, the flux equation may then be expressed as

$$F = C_2 y T \frac{dT}{dy}. \quad (\text{A.4})$$

Substituting $u = T/T_0$ and $x = y/y_0$ yields

$$F = (K\rho)_{y_0, T_0} u x \frac{T_0}{y_0} \frac{du}{dx}, \quad (\text{A.5})$$

where $(K\rho)_{y_0, T_0}$ is the product of the conductivity and density at the base of the hydrogen burning zone. Substituting

$$C = \left(\frac{F y}{K \rho T} \right)_{y_0, T_0} \quad (\text{A.6})$$

gives the solvable equation

$$C = u x \frac{du}{dx}, \quad (\text{A.7})$$

whose solution is

$$T = T_0 \left[2C \ln \left(\frac{y}{y_0} \right) + 1 \right]^{1/2}. \quad (\text{A.8})$$

Calculating C at y_0 and solving for the flux yields Equation 3.33.

A series of calculations was made in order to determine C . The temperature was set at a column depth of 10^8 g cm^{-2} , and the flux was varied to calculate temperatures at the outer boundary of the crust, $2 \times 10^{12} \text{ g cm}^{-2}$. A fit of this data gives $C = 0.62$.

Appendix B

Heat capacity and neutrino luminosity of the core

In order to calculate the total heat capacity of the core, it was necessary to calculate the thermal structure of the core including a model of superfluidity. An equation of state by Tolman [147] was used to approximate the density in the core as a function of radius

$$\rho = \rho_c \left[1 - \left(\frac{r}{R} \right)^2 \right], \quad (\text{B.1})$$

where ρ_c is the central density calculated from

$$\rho_c = \frac{15M}{8\pi R^3}. \quad (\text{B.2})$$

This equation of state, although analytical, reproduces the general trend of neutron star core equations of state that have been fit from nucleon-nucleon scattering data.

The total heat capacity is given by $C = \int c_P dV$, where

$$dV = 4\pi r^2 \left(1 - \frac{2Gm}{rc^2} \right)^{-1/2} dr \quad (\text{B.3})$$

accounts for relativistic effects and $m = m(r)$ is the gravitational mass within a sphere

of radius r . In this equation, the specific heat, c_P , has been calculated following the work of Yakovlev et al. [169], allowing for ${}^3\text{P}_2$ neutron superfluidity and ${}^1\text{S}_0$ proton superfluidity. The critical temperatures for these states were determined in the same manner as the critical temperatures in the crust following Brown [23]. See Table 3.1 for the relevant parameters. Due to the strong relativistic effects in the core, the formula for the nucleon specific heat (Equation 3.9) utilises the redshifted temperature, $T(r) = T_{cc}e^{-\phi/c^2}$.

The total neutrino luminosity in the core as input for Equation 3.35 is expressed as

$$L_\nu = \int Qe^{2\phi}dV, \quad (\text{B.4})$$

where Q is the neutrino emissivity (Equations 3.26 and 3.27 or Equation 3.30) and dV is given by Equation B.3. The neutrino emissivity is composed of the relevant components: either all modified Urca, or a combination of the direct and modified Urca processes including reduction factors allowing for nucleon superfluidity. The formulation used here is described in [169]. Neutrino emission due to Cooper pairing has not been considered here since it is most effective near the critical temperature, $T_c \sim 10^9$ K. Temperatures in the core for these calculations are significantly below the critical temperature, so the effects of this process are much less important than the Urca processes.

With the neutron star characteristics used in this calculation, only the most central part of the core was subject to the direct Urca process. This region was determined by where the total neutrino emissivity of the core increases rapidly as a function of density. For a $1.4 M_\odot$, 10 km star the direct Urca region consisted of matter at densities greater than 1.5×10^{15} g cm $^{-3}$. When including the direct Urca process, the core is still subject to the modified Urca process for $\rho_{cc} < \rho < 4.4 \times 10^{14}$ g cm $^{-3}$. Cooling in the intervening region, $4.4 \times 10^{14} < \rho < 1.5 \times 10^{15}$ g cm $^{-3}$, is treated as a linear interpolation of the two Urca processes.

The reduction factor for the neutron branch of the modified Urca process in Equation 3.26 is

$$R^{Mn} = \frac{a^{7.5} + b^{5.5}}{2} \exp \left[3.4370 - \sqrt{(3.4370)^2 + v_p^2} \right], \quad (\text{B.5})$$

where

$$a = 0.1477 + \sqrt{(0.8523)^2 + (0.1175v_p)^2} \quad (\text{B.6})$$

and

$$b = 0.1477 + \sqrt{(0.8523)^2 + (0.1297v_p)^2}. \quad (\text{B.7})$$

Protons in the core couple in a $^1\text{S}_0$ state, so the factor v_p is given by Equation 3.13.

For the proton branch (Equation 3.27), the reduction factor is given by

$$R^{Mp} = \frac{a^7 + b^5}{2} \exp \left[2.398 - \sqrt{(2.398)^2 + v_n^2} \right], \quad (\text{B.8})$$

where

$$a = 0.1612 + \sqrt{(0.8388)^2 + (0.1117v_n)^2} \quad (\text{B.9})$$

and

$$b = 0.1612 + \sqrt{(0.8388)^2 + (0.1274v_n)^2}. \quad (\text{B.10})$$

The factor v_n is given by Equation 3.14 since neutrons are expected to pair in the $^3\text{P}_2$ configuration in the core. Of course $R^{Mn} = R^{Mp} = 1$ if the local temperature is greater than the critical temperature (Equation 3.10).

In the direct Urca process, only the protons are expected to be superfluid throughout the core, so the reduction factor in Equation 3.30 is expressed as

$$R^D = \left[0.2312 + \sqrt{(0.7688)^2 + (0.1438v_p)^2} \right]^{5.5} \exp \left[3.427 - \sqrt{(3.427)^2 + v_p^2} \right], \quad (\text{B.11})$$

where, again, v_p is given by Equation 3.13.

Bibliography

- [1] V. Abartsumyan and G. Saakyan. *Sov. Astron.*, **4**:187, 1960.
- [2] A. Akmal, V. Pandharipande, and D. Ravenhall. *Phys. Rev. C*, **58**:1804, 1998.
- [3] C. Alcock, E. Farhi, and A. Olinto. *ApJ*, **310**:261, 1986.
- [4] L. Amundsen and E. Østgaard. *Nucl. Phys. A*, **437**:487, 1985.
- [5] L. Amundsen and E. Østgaard. *Nucl. Phys. A*, **442**:163, 1985.
- [6] D. Arnett. *Supernovae and Nucleosynthesis*. Princeton, Princeton, 1996.
- [7] G. Audi et al. *Nucl. Phys. A*, **624**:1, 1997.
- [8] W. Baade and F. Zwicky. *Phys. Rev.*, **45**:138, 1934.
- [9] G. Bader and P. Deuffhard. *Num. Math.*, **41**:373, 1983.
- [10] J. Bahcall and R. Wolf. *Phys. Rev. Lett.*, **14**:343, 1965.
- [11] J. Bahcall and R. Wolf. *Phys. Rev. B*, **140**:1452, 1965.
- [12] D. Baiko et al. *Phys. Rev. Lett.*, **81**:5556, 1998.
- [13] D. Bazin et al. *Nucl. Instr. and Meth. A*, **482**:307, 2002.
- [14] D. Bazin et al. *Nucl. Instr. and Meth. B*, **204**:629, 2003.
- [15] R. Belian, J. Conner, and W. Evans. *ApJ*, **206**:L135, 1976.
- [16] H. Bethe and M. Johnson. *Nucl. Phys. A*, **230**:1, 1974.
- [17] L. Bildsten. *ApJ*, **501**:L89, 1998.
- [18] G. Bisnovatyi-Kogan and V. Chechetkin. *Sov. Phys. Usp.*, **22**:89, 1979.
- [19] B. Brown, W. Chung, and B. Wildenthal. *Phys. Rev. Lett.*, **40**:1631, 1978.
- [20] E. Brown. *ApJ*, **614**:L57, 2004.
- [21] E. Brown and L. Bildsten. *ApJ*, **496**:915, 1998.

- [22] E. Brown, L. Bildsten, and R. Rutledge. *ApJ*, **504**:L95, 1998.
- [23] E. F. Brown. *ApJ*, **531**:988, 2000.
- [24] L. Burderi et al. *ApJ*, **574**:930, 2002.
- [25] A. Burrows. *Phys. Rev. Lett.*, **44**:1640, 1980.
- [26] A. Cameron. *ApJ*, **130**:884, 1959.
- [27] S. Campana et al. *A&A*, **324**:941, 1997.
- [28] S. Campana et al. *A&A Rev.*, **8**:279, 1998.
- [29] R. Canal, J. Isern, and J. Labay. *Ann. Rev. Astron. Astrophys.*, **28**:183, 1990.
- [30] G. Caughlan and W. Fowler. *At. Data Nucl. Data Tables*, **40**:283, 1988.
- [31] G. Chabrier and A. Potekhin. *Phys. Rev. E*, **58**:4941, 1998.
- [32] M. Chartier et al. *Nucl. Phys. A*, **637**:3, 1998.
- [33] W. Chen, C. Schrader, and M. Livio. *ApJ*, **491**:312, 1997.
- [34] K. Cheng, Y. Li, and W. Suen. *ApJ*, **499**:L45, 1998.
- [35] H. Chiu and E. Salpeter. *Phys. Rev. Lett.*, **12**:413, 1964.
- [36] N. Chong and K. Cheng. *ApJ*, **425**:210, 1994.
- [37] M. Colpi et al. *ApJ*, **548**:L178, 2001.
- [38] L. Cominsky and K. Wood. *ApJ*, **337**:485, 1984.
- [39] L. Cominsky and K. Wood. *ApJ*, **283**:765, 1989.
- [40] R. Cooper and R. Narayan. [astro-ph/0410462](https://arxiv.org/abs/astro-ph/0410462), , 2004.
- [41] R. Cornelisse et al. *A&A*, **357**:L21, 2000.
- [42] R. Cornelisse et al. *A&A*, **382**:174, 2002.
- [43] A. Cumming and L. Bildsten. *ApJ*, **544**:453, 2000.
- [44] A. Cumming and L. Bildsten. *ApJ*, **559**:L127, 2001.
- [45] R. Doxsey et al. *ApJ*, **228**:L67, 1979.
- [46] D. Eichler and A. Cheng. *ApJ*, **336**:360, 1989.
- [47] A. Fabian, J. Pringle, and M. Rees. **172**:15, 1975.
- [48] R. Farouki and S. Hamaguchi. *Phys. Rev. E*, **47**:4330, 1993.

- [49] A. Finzi. *ApJ*, **139**:1398, 1964.
- [50] P. Fonte, V. Peskov, and F. Sauli. *Nucl. Instr. and Meth. A*, **305**:91, 1991.
- [51] B. Friman and O. Maxwell. *ApJ*, **232**:541, 1979.
- [52] M. Fujimoto et al. *ApJ*, **278**:813, 1984.
- [53] G. Fuller, W. Fowler, and M. Newman. *ApJ*, **42**:447, 1980.
- [54] G. Fuller, W. Fowler, and M. Newman. *ApJ*, **252**:715, 1982.
- [55] G. Fuller, W. Fowler, and M. Newman. *ApJS*, **48**:279, 1982.
- [56] G. Fuller, W. Fowler, and M. Newman. *ApJ*, **293**:1, 1985.
- [57] D. Galloway et al. *ApJ*, **590**:999, 2003.
- [58] M. Garcia and P. Callanan. *AJ*, **118**:1390, 1999.
- [59] R. Giacconi et al. *Phys. Rev. Lett.*, **9**:439, 1962.
- [60] A. Gillibert et al. *Phys. Lett. B*, **176**:317, 1986.
- [61] A. Gillibert et al. *Phys. Lett. B*, **192**:39, 1987.
- [62] G. Glen and P. Sutherland. *ApJ*, **239**:671, 1980.
- [63] J. Grindlay et al. *ApJ*, **205**:L127, 1976.
- [64] E. Gudmundsson, C. Pethick, and R. Epstein. *ApJ*, **272**:286, 1983.
- [65] P. Haensel, A. Kaminker, and D. Yakovlev. *A&A*, **314**:328, 1996.
- [66] P. Haensel and J. Zdunik. *A&A*, **227**:431, 1990.
- [67] P. Haensel and J. Zdunik. *A&A*, **404**:L33, 2003.
- [68] T. Hamada and E. Salpeter. *ApJ*, **134**:683, 1961.
- [69] B. Harrison, M. Wakano, and J. Wheeler. In *La Structure et l'évolution de l'univers*, Brussels, Belgium, 1958. Onzième Conseil de Physique Solvay.
- [70] M. Hashimoto, H. Seki, and M. Yamada. *Prog. Theor. Phys.*, **71**:320, 1984.
- [71] G. Hempel, F. Hopkins, and G. Schatz. *Nucl. Instr. and Meth.*, **131**:445, 1975.
- [72] L. Henyey and J. L'Ecuyer. *ApJ*, **156**:549, 1969.
- [73] A. Hewish et al. *Nature*, **217**:709, 1968.
- [74] R. Hulse and J. Taylor. *ApJ*, **195**:L51, 1975.

- [75] I. Iben. *ApJS*, **76**:55, 1991.
- [76] J. in 't Zand, R. Cornelisse, and A. Cumming. *A&A*, **426**:257, 2004.
- [77] H. Inoue et al. *ApJ*, **250**:L71, 1981.
- [78] J. in't Zand et al. *IAU Circ*, **7138**:1, 1999.
- [79] J. in't Zand et al. *A&A*, **411**:L487, 2003.
- [80] N. Itoh et al. *ApJS*, **102**:411, 1996.
- [81] N. Itoh and Y. Kohyama. *ApJ*, **404**:268, 1993.
- [82] N. Iwamoto. *Phys. Rev. Lett.*, **44**:1637, 1980.
- [83] P. Jones. *astro-ph/0502182*, 2005.
- [84] D. Kaplan and A. Nelson. *Phys. Lett. B*, **175**:57, 1986. Errata: **179**, 409.
- [85] E. Kuulkers. *A&A*, **383**:L5, 2002.
- [86] E. Kuulkers et al. *A&A*, **382**:503, 2002.
- [87] E. Kuulkers et al. *astro-ph/0402076*, 2004.
- [88] L. Landau and E. Lifshitz. *Fluid Mechanics*. Pergamon Press, New York, 1987.
- [89] K. Langanke et al. *Phys. Rev. Lett.*, **90**:241102, 2003.
- [90] K. Langanke and G. Martínez-Pinedo. *Nucl. Phys. A*, **673**:481, 2000.
- [91] K. Langanke and G. Martínez-Pinedo. *Private communication*, 2001.
- [92] J. Lattimer et al. *Phys. Rev. Lett.*, **66**:2701, 1991.
- [93] K. Levenfish and D. Yakovlev. *Astron. Rep.*, **38**:247, 1994.
- [94] W. Lewin, J. Hoffman, and J. Doty. *IAU Circ.*, **2994**:2, 1976.
- [95] U. Lynen et al. *Nucl. Instr. and Meth.*, **162**:657, 1979.
- [96] F. Mackie and G. Baym. *Nucl. Phys. A*, **283**:332, 1977.
- [97] N. Madsen and R. Sincovec. In *Computational Methods in Nonlinear Mechanics*, Austin, TX, 1974. Texas Inst. for Computational Mechanics.
- [98] K. Makishima et al. *ApJ*, **247**:L23, 1981.
- [99] L. Maraschi and A. Cavaliere. *Highlights Astron.*, **4**:127, 1977.
- [100] O. Maxwell. *ApJ*, **231**:201, 1979.

- [101] R. Mignani et al. *A&A*, **389**:L11, 2002.
- [102] P. Möller, J. Nix, and K.-L. Kratz. *At. Data Nucl. Data Tables*, **66**:131, 1997.
- [103] M. Muno et al. *ApJ*, **542**:1016, 2000.
- [104] M. Muno et al. *ApJ*, **553**:L157, 2001.
- [105] J.-U. Nabi. *Eur. Phys. J. A*, **5**:337, 1999.
- [106] A. Nelson and D. Kaplan. *Phys. Lett. B*, **192**:193, 1987.
- [107] S. Nishimura et al. *Nucl. Instr. and Meth. A*, **510**:377, 2003.
- [108] S. Ogata, S. Ichimaru, and H. van Horn. *ApJ*, **417**:265, 1993.
- [109] T. Oosterbroek et al. *A&A*, **372**:922, 2001.
- [110] J. Oppenheimer and G. Volkoff. *Phys. Rev.*, **55**:374, 1939.
- [111] J. Orosz, C. Bailyn, and K. Whitman. *ATel*, #75, 2001.
- [112] N. Orr et al. *Phys. Lett. B*, **258**:29, 1991.
- [113] A. Parmar et al. *ApJ*, **308**:199, 1986.
- [114] C. Pethick, D. Ravenhall, and C. Lorenz. *Nucl. Phys. A*, **584**:675, 1995.
- [115] C. Pethick and V. Thorsson. *Phys. Rev. Lett.*, **72**:1964, 1994.
- [116] W. Pietsch et al. *A&A*, **157**:23, 1986.
- [117] W. Pietsch, H. Steinle, and M. Gottwald. **3887**:3, 1983.
- [118] A. Potekhin, G. Chabrier, and D. Yakovlev. *A&A*, **323**:415, 1997.
- [119] A. Potekhin et al. *A&A*, **346**:345, 1999.
- [120] J. Pruet and G. Fuller. *ApJS*, **149**:189, 2003.
- [121] D. Ravenhall, C. Pethick, and J. Wilson. *Phys. Rev. Lett.*, **50**:2066, 1983.
- [122] R. Rutledge et al. *ApJ*, **514**:945, 1999.
- [123] R. Rutledge et al. *ApJ*, **551**:921, 2001.
- [124] R. Rutledge et al. *ApJ*, **580**:413, 2002.
- [125] F. Sarazin et al. *Phys. Rev. Lett.*, **84**:5062, 2000.
- [126] K. Sato. *Prog. Theor. Phys.*, **62**:957, 1979.
- [127] H. Schatz, L. Bildsten, and A. Cumming. *ApJ*, **583**:L87, 2003.

- [128] H. Schatz et al. *Phys. Rev.*, **294**:167, 1998.
- [129] H. Schatz et al. *ApJ*, **524**:1014, 1999.
- [130] H. Schatz et al. *Phys. Rev. Lett.*, **86**:3471, 2001.
- [131] H. Schatz et al. *Nucl. Phys. A*, **718**:247, 2003.
- [132] P. Schinder et al. *ApJ*, **313**:531, 1987.
- [133] E. Schreier et al. *ApJ*, **172**:L79, 1972. Errata: **173**, L51.
- [134] S. Shapiro and S. Teukolsky. *Black Holes, White Dwarfs, and Neutron Stars: The Physics of Compact Objects*. John Wiley & Sons, New York, 1983.
- [135] R. Sincovec and N. Madsen. *ACM Transactions on Mathematical Software (TOMS)*, **1**:232, 1975.
- [136] H. Stelzer. *Nucl. Instr. and Meth.*, **133**:409, 1976.
- [137] T. Strohmayer. *Classical and Quantum Gravity*, **19**:1321, 2002.
- [138] T. Strohmayer and E. Brown. *ApJ*, **566**:1045, 2002.
- [139] T. Strohmayer and C. Markwardt. *ApJ*, **577**:337, 2002.
- [140] D. Swan, J. Yurkon, and D. Morrissey. *Nucl. Instr. and Meth. A*, **348**:314, 1994.
- [141] R. Syunyaev et al. *Sov. Astron. Lett.*, **16**:1, 1990.
- [142] T. Takatsuka and R. Tamagaki. *Prog. Theor. Phys. Supp.*, **112**:27, 1993.
- [143] H. Tananbaum et al. *ApJ*, **174**:L143, 1972.
- [144] K. Thorne. *ApJ*, **212**:825, 1977.
- [145] F. Timmes. *ApJ*, **390**:L107, 1992.
- [146] F. Timmes and F. Swesty. *ApJS*, **126**:501, 2000.
- [147] R. Tolman. *Phys. Rev.*, **55**:364, 1939.
- [148] S. Tsuruta. *Phys. Rev.*, **292**:1, 1998.
- [149] V. Urpin and D. Yakovlev. *Sov. Astron.*, **24**:126, 1980.
- [150] G. Ushomirsky, C. Cutler, and L. Bildsten. *MNRAS*, **319**:902, 2000.
- [151] G. Ushomirsky and R. Rutledge. *MNRAS*, **325**:1157, 2001.
- [152] J. van Paradijs et al. *A&A*, **182**:47, 1987.
- [153] K. van Riper. *ApJS*, **75**:449, 1991.

- [154] Y. Vartanyan and N. Ovakimova. *Soob. Byur. Obs.*, **49**:87, 1976.
- [155] R. Wallace and S. Woosley. *ApJS*, **45**:389, 1981.
- [156] R. Wijnands. *ApJ*, **554**:L59, 2001.
- [157] R. Wijnands. In *The High Energy Universe at Sharp Focus: Chandra Science*, San Francisco, 2002. Astronomy Society of the Pacific.
- [158] R. Wijnands et al. *ApJ*, **573**:L45, 2001.
- [159] R. Wijnands et al. *ApJ*, **560**:L159, 2001.
- [160] R. Wijnands et al. *ATel*, #72, 2001.
- [161] R. Wijnands et al. *ApJ*, **566**:1060, 2002.
- [162] R. Wijnands et al. *ApJ*, **594**:952, 2003.
- [163] R. Wijnands et al. *ApJ*, **606**:L61, 2004.
- [164] E. Witten. *Phys. Rev. D*, **30**:272, 1984.
- [165] S. Woosley et al. *ApJS*, **151**:75, 2004.
- [166] S. Woosley and R. Taam. *Nature*, **263**:101, 1976.
- [167] D. Yakovlev. *Sov. Astron.*, **31**:347, 1987.
- [168] D. Yakovlev and A. Kaminker. *Ast.L.*, **22**:491, 1996.
- [169] D. Yakovlev, K. Levenfish, and Y. Shibano. *Physics-Uspekhi*, **42**:737, 1999.
- [170] D. Yakovlev and V. Urpin. *Sov. Astron.*, **24**:3, 1980.
- [171] J. Yurkon et al. *Nucl. Instr. and Meth. A*, **422**:291, 1999.
- [172] L. Zampieri et al. *ApJ*, **439**:849, 1995.
- [173] J. Ziman. *Principles of the Theory of Solids*. Cambridge University Press, Cambridge, 1972.